Plasma Discharges in Gas Bubbles in Liquid Water: Breakdown Mechanisms and Resultant Chemistry

by

Sarah M. N. Gucker

A dissertation submitted in partial fulfillment
of the requirements for the degree of
Doctor of Philosophy
(Nuclear Engineering and Radiological Sciences)
in The University of Michigan
2015

Doctoral Committee:

Professor John E. Foster, Chair
Assistant Research Scientist Natalia Babaeva
Professor Ronald M. Gilgenbach
Professor Mark Kushner

Ad Majorem Dei Gloriam.

To Joseph and Deborah,
my wonderful parents.

To Damien and Micah,
my sweet boys.

To Dennis,
my loving husband and best friend.

To God,
my Creator, Savior, and Counselor.
I can do all things in Him who strengthens me.

Acknowledgements

Throughout the course of my graduate school career I have been inordinately blessed: academically, professionally, financially, personally. I am grateful for this opportunity to acknowledge these individuals and resources that have supported me on this journey.

Firstly, this work, the discoveries and dead ends it encompassed, would simply not be what it is now, what you, the reader, hold in its final form, if it were not for my mentor, John E. Foster. My academic, professional, and personal growth over the last five years are due to the deep knowledge, guiding leadership, and supportive energy he has shared during my time at the University of Michigan. Additionally, I would like to thank my committee: Ron Gilgenbach, Mark Kushner, and Natalia Babaeva. They have each given me the great honor of sharing their time, efforts, and expertise to assist me in my graduate career and through the final steps of my doctoral program. I am sincerely grateful, and thank them sincerely.

I am enormously thankful for my friends and colleagues during this graduate school experience and time. I am grateful not only for the knowledge and experience these individuals passed on to me (both personally and academically/professionally), but I am convinced that successfully traversing the sometimes barren landscape of graduate school is made possible through the psychological and emotional benefit of friends and compatriots. I specifically want to mention previous lab mates: Aimee Hubble, Benjamin Yee, Bradley Sommers, Kapil Sawlani, Eric Gilman, and Alexander Englesbe. In addition, the women of the NERS department, especially Cassie Brown and fellow mama Crystal Thrall, as well as Sonal Joshi, Anne Campbell, Eva Sunny and all the other women who created a welcoming atmosphere in a very male-dominated field and environment. Thank you! I would also like to thank Amanda Lietz of Prof. Kushner's group who took time to equip me to use *GlobalKIN* to numerically verify results.

I would like to thank my dear friends from my undergraduate institution, the University of Northern Colorado, who encouraged me to continue on, especially Jenna Simonton, Erin (Simonton) Day, Amy (Devlin) Fraser, Katherine Placzek, Kayleigh Glaspie, Rachelle (Ivy)

Baron, Katheryn Hamm, and Mackenzie Wiggs. A deep, deep thank you to my professors from the University of Northern Colorado Physics Department, especially Dr. Cynthia Galovich, Dr. Robert Walch, and Dr. Matthew Semak, who gave me the tools and the crucial physics foundation that equipped me to even begin to consider a PhD. You were all specifically sources of encouragement, blessing and grace in my life during undergrad and even if you were not aware of it, thank you for your part in getting me here.

I would like to acknowledge the resources and incredible opportunities afforded to me to get to this point, as well as the individuals associated with them. These include the Colorado Space Grant Consortium, the National Science Foundation Research Experience for Undergraduates (NSF REU) program at the University of Wyoming, the NASA Ames Academy for Space Exploration, and NASA Goddard Flight Center. Additionally, I am eternally grateful for the National Science Foundation's Graduate Research Fellowship Program (NSF GRFP) for the financial support during my PhD studies. Other funding sources and privileges I was blessed to have include NSF CBET grants and a graduate fellowship through the Michigan Institute for Plasma Science and Engineering (MIPSE).

Of course, my deepest thank you's are to my dear family, immediate and extended, birth and in-law. To my siblings: Dave Nowak, John Nowak, Vincent Nowak, Gemma Nowak, Clare Nowak, Frank Nowak, Helen Nowak, Becky Nowak, Ellie (Bova) Nowak and Steve Nowak; to my siblings in-law: Justin Gucker, Rebecca Gucker, Alisha (Gucker) Lester and Todd Lester; to my parents-in-law: Ruth Gucker and Jeff Gucker; to my dear parents, Debbie Nowak and Joseph Nowak, who were a constant source of encouragement from the very beginning of my school experience; to my dear sons, Micah Gucker and Damien Gucker, who inspired me to work efficiently and rigorously, and who are my inspiration to create a better future through scientific progress; and finally, to my best friend and husband, Dennis Gucker, who provided constant emotional, intellectual and spiritual support throughout my entire graduate school career.

In closing, please forgive me if I have forgotten anyone significant in this section. I would like to give my sincerest gratitude to those who paved the way for women in science and female researchers. To those who were not able to complete their academic training (at any level) due to incomplete resources or support, this work is dedicated in some part to you. Finally, I would like to acknowledge the enormous blessing from God this entire experience has been, from funding and general support to my classes and conferences.

Thank you.

For I know the plans I have for you, declares the Lord, plans to prosper you and not to harm you, plans to give you hope and a future. (Jer 29:11)

Table of Contents

List of Figures

List of Tables

Abstract

Plasma Discharges in Gas Bubbles in Liquid Water: Breakdown Mechanisms and Resultant Chemistry

by

Sarah M. N. Gucker

Chair: Prof. John E. Foster

The use of atmospheric pressure plasmas in gases and liquids for purification of liquids has been investigated by numerous researchers, and is highly attractive due to their strong potential as a disinfectant and sterilizer. However, the fundamental understanding of plasma production in liquid water is still limited. Despite the decades of study dedicated to electrical discharges in liquids, many physical aspects of liquids, such as the high inhomogeneity of liquids, complicate analyses. For example, the complex nonlinearities of the fluid have intricate effects on the electric field of the propagating streamer. Additionally, the liquid material itself can vaporize, leading to discontinuous liquid-vapor boundaries. Both can and do often lead to notable hydrodynamic effects. The chemistry of these high voltage discharges on liquid media can have circular effects, with the produced species having influence on future discharges. Two notable examples include an increase in liquid conductivity via charged species production, which affects the discharge. A second, more complicated scenario seen in some liquids (such as water) is the doubling or tripling of molecular density for a few molecule layers around a high voltage electrode. These complexities require technological advancements in optical diagnostics that have only recently come into being.

This dissertation investigates several aspects of electrical discharges in gas bubbles in liquids. Two primary experimental configurations are investigated: the first allows for single bubble analysis through the use of an acoustic trap. Electrodes may be brought in around the

bubble to allow for plasma formation without physically touching the bubble. The second experiment investigates the resulting liquid phase chemistry that is driven by the discharge. This is done through a dielectric barrier discharge with a central high voltage surrounded by a quartz discharge tube with a coil ground electrode on the outside. The plasma is created either through flowing gas around the high voltage electrode in the discharge tube or self-generated by the plasma as in the steam discharge. This second method allows for large scale processing of contaminated water and for bulk chemical and optical analysis.

Breakdown mechanisms of attached and unattached gas bubbles in liquid water were investigated using the first device. The breakdown scaling relation between breakdown voltage, pressure and dimensions of the discharge was studied. A Paschen-like voltage dependence for air bubbles in liquid water was discovered. The results of high-speed photography suggest the physical charging of the bubble due to a high voltage pulse; this charging can be significant enough to produce rapid kinetic motion of the bubble about the electrode region as the applied electric field changes over a voltage pulse. Physical deformation of the bubble is observed. This charging can also prevent breakdown from occurring, necessitating higher applied voltages to overcome the phenomenon.

This dissertation also examines the resulting chemistry from plasma interacting with the bubble-liquid system. Through the use of optical emission spectroscopy, plasma parameters such as electron density, gas temperature, and molecular species production and intensity are found to have a time-dependence over the ac voltage cycle. This dependence is also source gas type dependent. These dependencies afford effective control over plasma-driven decomposition. The effect of plasma-produced radicals on various wastewater simulants is studied. Various organic dyes, halogenated compounds, and algae water are decomposed and assessed. Toxicology studies with melanoma cells exposed to plasma-treated dye solutions are completed, demonstrating the non-cytotoxic quality of the decomposition process.

Thirdly, this dissertation examines the steam plasma system, developed through this research to circumvent the acidification associated with gas-feed discharges. This steam plasma creates its own gas pocket via field emission. This steam plasma is shown to have strong decontamination properties, with residual effects lasting beyond two weeks that continue to decompose contaminants.

Finally, a “two-dimensional bubble” was developed and demonstrated as a novel diagnostic device to study the gas-water interface, the reaction zone. This device is shown to provide convenient access to the reaction zone and decomposition of various wastewater simulants is investigated.

Chapter 1:

Introduction

This dissertation is the study of atmospheric plasma interactions with liquids and gases, examining the fundamental physics and chemistry of such discharges. While the application of such discharges can be applied to a multitude of systems, this study focuses on the use of atmospheric plasma discharges for water purification and contaminant mitigation.

This chapter presents the motivation and historical backdrop for the interest in producing electrical discharges in liquid water. With the increases in the use of chemical compounds to support increasing production and land use worldwide, a pending crisis regarding water quality may be looming. Current water treatment technology is not designed to handle such contaminants. It is now well recognized that new technological advances are required [**1**]. Plasma-based water purification has the potential to address many of the issues facing the world in the 21st century. In the subsections that follow, a review of water treatment technologies is given followed by a historical overview of the development of plasma-driven water purification. The chief goal and focus of the dissertation is then identified. Finally, the proposed approach of this dissertation research is outlined.

1.1 Water

Water is key to life – human, animal, the environment itself. While approximately 3% of global water is freshwater, of this volume, only approximately one third of this freshwater is easily accessible (the two thirds majority is locked up in polar and glacial regions). This reality should immediately direct humanity's actions to preserve these finite reserves. However, increased industrial and agricultural activities have introduced large quantities of harmful compounds into the environment, which accumulate in the water system. These toxins include textile dyes, pesticides, herbicides, pharmaceuticals, and volatile organic compounds (VOCs). Conventional wastewater treatment is ineffective at completely removing these chemicals [**2**,**3**], which are detected in virtually all water (ground, surface, and ocean waters, sediments, soils).

1.1.1 Magnitude of the problem

Globally, textile runoff is the largest producer of contaminated water [**4**]. Every year, approximately 1 Mkg of dyestuffs are ejected into the environment [**5**], many of which are endocrine disrupting chemicals [**6**]. Some may also decompose to carcinogenic compounds [**7**]. One common herbicide, atrazine, has been found to be present in the environment in excess of 1.0 ppb. Heavily studied in frog populations, mutations such as excess or missing limbs, hermaphroditism and loss of reproductive organs has been noted in several frog species at atrazine concentrations of 0.1 ppb [**8**]. Some of the most threatening substances are the endocrine disrupting compounds (EDCs), which are quite harmful to animal and human endocrine systems [**9**,**10**]. In the United States, VOCs have been detected at elevated concentrations throughout the nation's aquifers; almost 20% of ground-water wells were found to contain VOCs [**11**].

Pharmaceutical accumulation in the environment has already started to have substantial ecological effects; two well-known examples are the endangerment of three separate Asian vulture species[1] (due to diclofenac, a veterinary NSAID[2]) and the decline of non-intersex[3] fish (due to estrogen, etc.) [**12**]. These and other ubiquitously present pharmaceuticals may have irreversible effects for any level of the biological system (i.e., cells to ecosystems) [**13**].

Perhaps most alarming is the rise of antibiotic resistance pathogens. While antibiotic resistant bacteria such as MRSA (*Methicillin-resistant Staphylococcus aureus*) and CREs (*Carbapenem resistant enterobacteriaceae*, almost entirely immune to all available antibiotics) have made international headlines, antibiotic resistance is also cropping up in less-exotic pathogens, such as salmonella [**14**]. A 2013 report published by the Center for Disease Control on antibiotic resistance calls the rapid rise in antibiotic and antimicrobial resistance "one of our most serious health threats" with "potentially catastrophic consequences of inaction" [**15**].

---

[1] Endangered vulture species: Oriental white-backed vulture; long-billed vulture; slender-billed vulture.

[2] i.e., nonsteroidal anti-inflammatory drug, e.g., aspirin, ibuprofen.

[3] i.e., fish species that have distinct male and female members. Feminization of male fish has been widely studied. These species have been consistently shown to decline in population due to their inability to breed effectively, while intersex fish populations – those not effected by estrogen – increase.

1.1.1.1 Global effects

Safe access to clean water has been declared a basic human right by the United Nations [**16**] and identified as a Grand Challenge by the National Academy of Engineering [**17**]; however, one out of five children in the world does not have access to clean water, and around 1.8 million die every year due to water-related illnesses [**18**]. Lack of water availability has socio-economic impacts as well. For example, people living in water insecure areas (usually children and women in the developing world) typically must walk on average three miles a day to obtain water necessary for the day, which result in little to no time is left for education [**16**]. Access to clean water is crucial to breaking the cycle of poverty.

1.1.2 Current water contaminant mitigation methods

1.1.2.1 Conventional methods

The natural response to the accumulation of contaminants in source water is to first appreciate the capabilities of conventional water treatment approaches and understand the deficiencies to construct a better method. The contaminant removal capacity of conventional methods is linked with the chemistry of the individual contaminant, as well as the naturally occurring chemistry of the water, which is typically dependent on local geology (e.g., limestone and high levels of $CaCO_3$, or hard water [**19**]). Because of this, water treatment facilities vary from location to location, incorporating treatment processes as necessary. A multitude of treatment processes used in the United States exists, but in general conventional treatment is considered to refer to coagulation[4], flocculation[5], sedimentation, and filtration[6] [**20**]. Conventional sewage treatment has been observed to remove typically around 90% of common pain relievers such as ibuprofen and naproxen, but essentially none of more significant medications, such as more powerful pain relievers, hormone supplements, and mental health prescription drugs [**21**].

A recent US Geological Survey study found the Chattahoochee River, which supplies drinking water to 3 million people in Atlanta, Georgia, had the same concentrations of containments (hydrocarbons, herbicides, etc.) before and after treatment [**22**] (see Figure 1.1).

[4] Contaminants are electrically neutralized, typically by adding alum or like compound, which allows precipitates termed "floc" to form.

[5] I.e., mixing.

[6] Current standard filtration includes slow sand filters and active carbon.

Beyond addressing externally derived contaminants, conventional treatment methods have been linked to a variety of health concerns, either through residual agents or the formation of

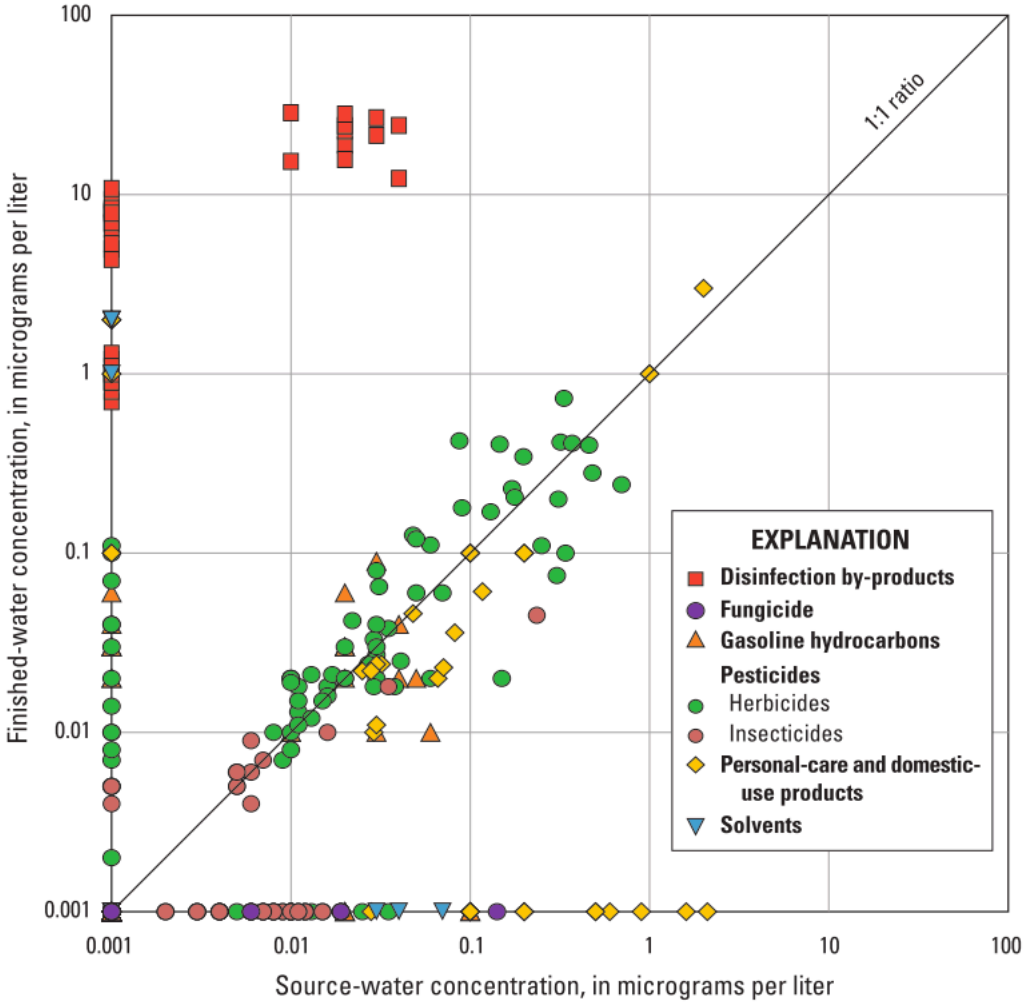

Figure 1.1: Drinking water contaminants in the Chattahoochee River feeding into Atlanta, Georgia. A 1:1 ratio (the center line) is for contaminants that pass through the disinfection/purification process completely unaffected. From [22].

disinfection by-products. Fluoridation, for example, has been linked with bone cancer, and disinfection by-products (DBPs, e.g., chloroform, originating from chlorination) are connected with leukemia, bladder and colon cancer [**23**]. Atlanta tap water from the Chattahoochee River was found to have up to tens of micrograms per liter of DBPs [**22**]. With recent publications reporting gains as "high" as 31% total removal (n.b., 0% removal of carbamazepine, a common anti-seizure medication) [**24**], relying on conventional removal of exotic compounds is not promising. New technologies must be developed to combat the increasing quantity of hazardous material.

1.1.2.2 Advanced techniques

Many advanced methods of water purification exist, all with their individual benefits and drawbacks. A few are outlined below.

1.1.2.2.1 Advanced Filters

Filtering-based processes are purification processes that utilize a filter, and are typically divided into two main categories: granular media filters and membrane filters. Granular filters are gravity-driven filters that strain out particulates through media such as sand and gravel, or more modern media such as activated carbon and polypropylene pellets. Granular filters of sand and gravel date back as far as 2000 BC in India [**20**].

A more recent technological advancement, membrane technology first entered municipal use in the 1950s. Membranes used by municipal water treatment facilities in the United States include microfiltration (MF), ultrafiltration (UF), nanofiltration (NF) and reverse osmosis (RO) (see Figure 1.2). (NF may be thought of as a special case of "standard" RO, with a specific cutoff of 1 nm.) In all types, these advanced filters are processes that force water through a membrane via pressure gradient, though filtering may be prompted by several other forces, including via electrical potential for electrodialysis and via temperature gradient with thermoosmosis [**20**].

RO produces high purity water (capable of removing more than 99% of targeted impurities), and of the major water treatment techniques current in use, has the distinct advantage of excellent desalination ability. However, the disadvantages of RO are due to the fact that a physical process performs the water treatment. RO is a slow process (1-50 L m^{-2} h^{-1}, compared to 30-170 L m^{-2} h^{-1} for MF and UF), and requires frequent replacement depending on the application (typical recovery values of the RO membrane range from 50% - 90%) [**20**]. The membrane is delicate (> 1 mm in thickness), and can be easily damaged (e.g., high flow rates, biofouling). Finally, some herbicides, pesticides, and VOCs are not affected by RO [**25**]. In addition, the rejection water/effluent must be properly disposed.

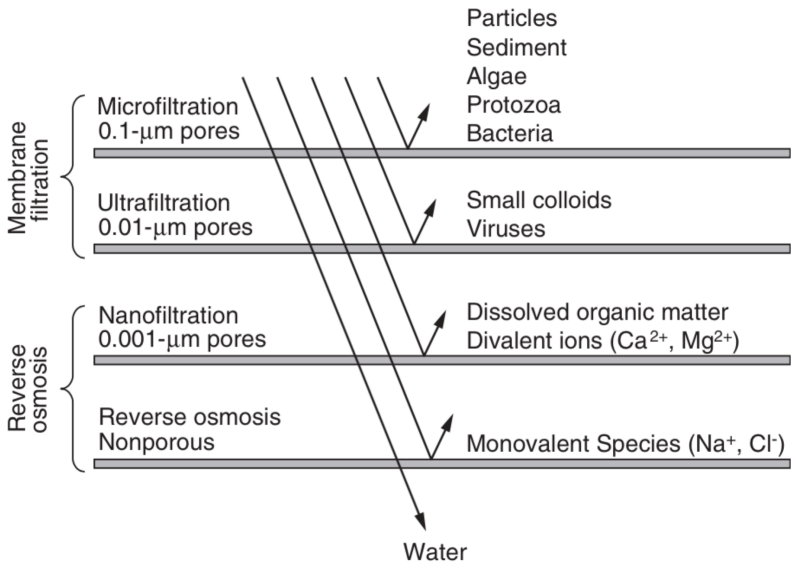

Figure 1.2: Filtration ability by type. From [26].

1.1.2.2.2 Ion Exchange

Ion exchange methods utilize the charge chemistry of various dissolved ionic contaminants to remove them (e.g., nitrate removal (NO_3^-)). Water is passed through a column filled with a cation-/anion-based resin which selectively removes anions/cations from the liquid (e.g., sulfonate (SO_3^-) column removes cations such as $Ca^{2+}, Ba^{2+}, Pb^{2+}$). This method is not a standard municipal treatment but is used in household systems or in applications where ultra high purity water is necessary, such as pharmaceutical and semiconductor industries. While effective at removing the targeted ions, ion exchange as a purification method is far too expensive for the large-volume water processing of a municipal source, as the columns must be replaced frequently [**20**].

1.1.2.2.3 Advanced Oxidation Processes (AOPs)

Considered by many to be the solution to 21st century water problems, advanced oxidation processes (AOPs) have been targeted as a viable method for neutralizing and destroying drinking water containments [**13**,**27**,**28**]. AOPs are processes that create and use primarily the hydroxyl radical (OH) to quickly oxidize containments. Other advanced oxidants that are also capable of decomposing or initiating the decomposition process include ozone (O_3), hydrogen peroxide (H_2O_2), atomic oxygen ($O(^1D)$, for example), ultraviolet photons, etc. This combination of highly oxidative species rapidly mineralizes containments, reducing particles to carbon dioxide, water and harmless inorganics. This aggressive oxidation also destroys viral, microbial, and

Table 1.1: Summary of common advanced oxidation types.

Type	Example	Pros	Cons	Reaction Rate *k*	Ref.
Photocatalysis	TiO_2/UV	Cheap Operate in ambient conditions Can use $h\nu_{solar}$	Sensitive to contaminant load, catalyst load, pH, temp., UV radiation time Slower than other AOPs	1×10^{-7}- 10^{-4} mol/(L min) (see note 7)	[**29**,**30**]
	O_3/TiO_2 $H_2O_2/O_3/TiO_2$	Might be faster than TiO_2 alone	No commercial applications		[**26**]
Fenton's reactions	Fe^{2+}/ H_2O_2 H_2O_2/ Fe^{2+}/UV	Good choice for acidic solutions (pH < 4) Photo-Fenton: fast for wide range of contaminants Can use $h\nu_{solar}$	Oxidation of organics inhibited by PO_4^{3-}, SO_4^{2-}, F^-, Br^-, Cl^- Cost Fe^{2+} ions added to solution	1×10^{-7}- 10^{-2} sec^{-1}	[**30**]
O_3 and H_2O_2 systems	H_2O_2/UV	Good for organics	H_2O_2 inefficient UV absorber Contaminant load, typically acidic pH (< 5) → limits H_2O_2	1×10^{-4}- 10^{-3} sec^{-1} (see note 8)	[**30**,**31**]
	O_3/UV	Good for organics Fast *k* for wide range of contaminants	Cost Low quantum efficiencies	1×10^{-5}- 10^{-2} sec^{-1} (see note [8])	[**30**,**31**]
	Ozonation	Excellent choice for most organics	One of the most expensive AOPs Incomplete mineralization can lead to production of hazardous compounds, e.g., bromate	1×10^{-5}- 10^{-2} sec^{-1}	[**30**,**26**]

[7] Reaction rates depend on pollutant (here, 2-/3-/4-CP; 2,3-/2,4-/2,6-/3,4-/3,5-DCP; 2,3,5-/2,4,6-TCP, PCP); pollutant concentration (0.1 – 1.0 mM); various TiO_2 dopants used.

[8] Pseudo-first order kinetic constants are given due to the dependency on contaminant concentration, reactant concentration, solution pH, catalysts concentration, UV radiation intensities, et cetera.

bacterial particles by attacking the cell membrane, destroying DNA. Conventional water treatment AOPs are commonly created via ozonation, UV-Ozone and Fenton reactions [**13**]. A summary of the major AOPs in commercial use or close to commercial use are presented in Table 1.1.

1.1.2.2.3.1 TiO_2/UV

UV photon irradiation of the TiO_2 semiconductor surface creates conduction band electrons (e_{cb}) and valence band holes (h^+) (1.1). The electrons produce superoxide (O_2^-) from the dissolved oxygen in the water (1.2) while hydroxyl radicals are produced from the reaction between holes and water molecules (1.3). In a TiO_2/UV system, contaminants are decomposed through oxidative reactions with valence band holes, superoxide and hydroxyl radicals, and reduction reactions with conduction band electrons. Electron and hole recombination is a fast (~30 ns) process, which limits the usefulness of the method. Nitrogen or metal ion (such as Fe^{3+}, Zn^{2+}, V^{5+}, etc.) doping of the semiconductor can alleviate this issue [**32**], and extensive literature exists on the effect of various metal dopants in TiO_2 and their increased decomposition rates on various contaminants [**33**].

$$TiO_2 + h\nu \rightarrow e_{cb} + h^+ \quad \textbf{(1.1)}$$

$$e_{cb} + O_2 \rightarrow O_2^- \quad \textbf{(1.2)}$$

$$h^+ + H_2O \rightarrow H^+ + OH \quad \textbf{(1.3)}$$

One of the positive aspects of TiO_2 as a photocatalysis for water purification is the ability to use solar photons, however there is only a small overlap between the absorption of TiO_2 and the output of solar radiation (on the surface of the Earth) [**34**].

1.1.2.2.3.2 Fenton Reactions

One of the simplest methods of producing hydroxyl radicals and hydroxide anions is through the use of Fenton reactions [**31**] (see (1.4)).

$$Fe^{2+} + H_2O_2 \rightarrow Fe^{3+} + OH^- + OH \quad \textbf{(1.4)}$$

From an industrial application standpoint, Fenton processes are highly reactive and easy to implement if the conditions of the wastewater are favorable. The largest requirement here is the

pH: pH values of 4 and higher have significantly decreased reaction rates and result in Fe^{3+} complexing with OH.

1.1.2.2.3.2.1 Photo-Fenton Reactions

With the application of photons ($\lambda \approx$ 250-400 nm) [**35**], the general reaction rate with organics is not only increased, but the Fe^{3+} complexes discussed just above undergo photolysis and release OH back into solution:

$$Fe(OH)^{2+} \xrightarrow{h\nu} Fe^{2+} + OH \quad \textbf{(1.5)}$$

1.1.2.2.3.3 Ozone and Hydrogen Peroxide Systems

The most commonly used AOP methods are O_3, H_2O_2/UV, O_3/UV, or combinations (such as H_2O_2/O_3) [**31**]. These systems utilize much of the same or similar chemistries, and are reviewed below together.

1.1.2.2.3.3.1 Ozone

Ozone rapidly reacts with organics, and as it was one of the first AOP investigated (see subsection Ozone on page 24), much literature and commercial application of ozonation exists. Complex chemistries are possible with ozonation: various products and by-products of the reaction between ozone and ethylene (C_2H_4) are given schematically in Figure 1.3.

Ozonation processes have several disadvantages, the chief two being cost and unwanted by-products. Ozone generation requires not only a generator (typically an oxygen DBD or glow discharge – running on liquid oxygen has safety constraints and expense), but also a cooling system and typically a need for post-treatment of residual ozone. In addition, the strong corrosive power of ozone places constraints on the types of materials that can actually be exposed to the water in the treatment process [**36**].

Ozonation generates unwanted by-products depending on the contaminant chemistry. In the case of solutions with bromide present, bromate (BrO_3^-) is readily formed upon reacting with ozone. Bromate is believed to be a human carcinogen with a maximum contaminant level (MCL, set by the U.S. EPA in the United States) of 10 μg/L [**26**]. Various pathways for bromate formation via ozonation are given in Figure 1.4.

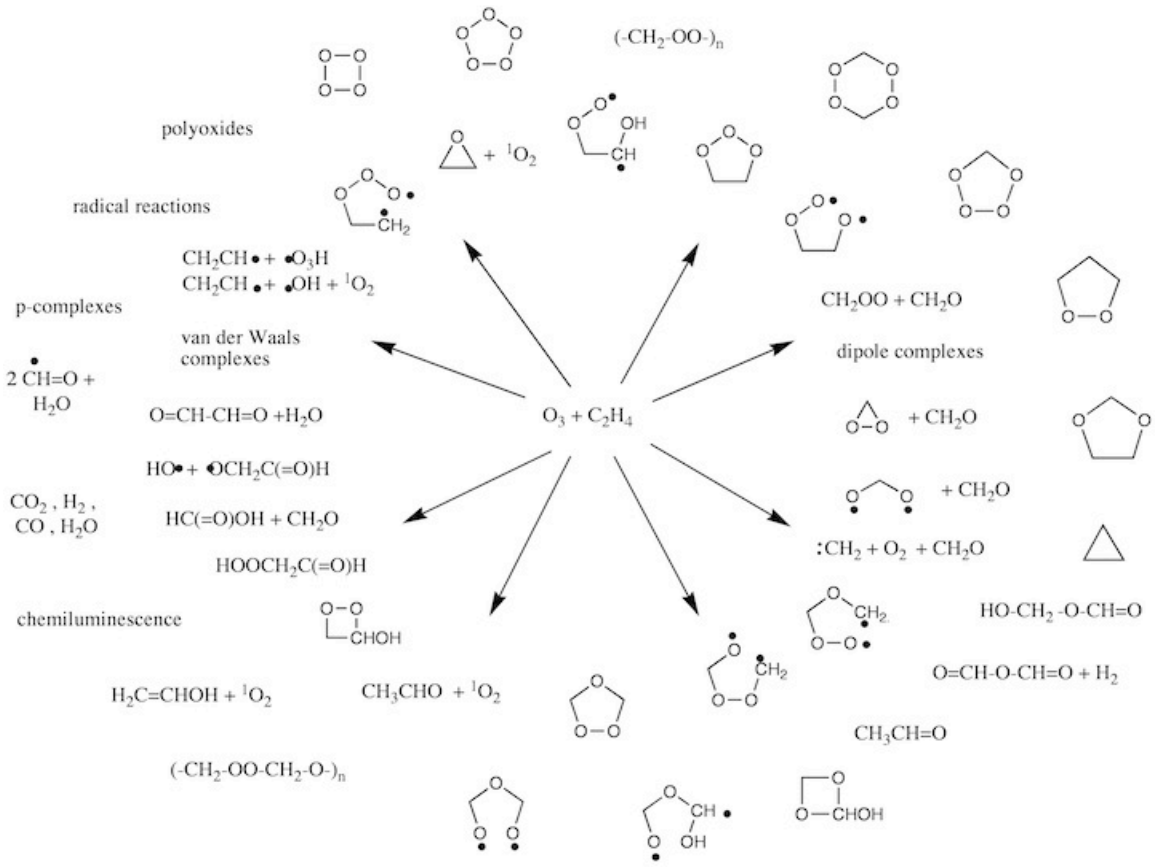

Figure 1.3: Possible products and by-products of ozone reacting with ethylene. From [37].

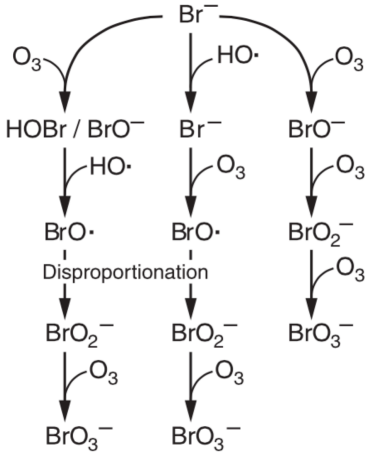

Figure 1.4: Various ozonation of bromide pathways that generate bromate. From [26].

1.1.2.2.3.3.2 Hydrogen Peroxide and UV (H_2O_2/UV)

Hydrogen peroxide will undergo photolysis when subjected to photons of $\lambda < 280$ nm [**38**]. This process has an overall quantum yield of one as hydrogen peroxide reacts with hydroxyls (see (1.6) through (1.8)).

$$H_2O_2 \xrightarrow{h\nu} 2OH$$

(1.6)

$$2(H_2O_2 + OH) \rightarrow H_2O + HO_2$$

(1.7)

$$2HO_2 \rightarrow H_2O_2 + O_2$$

(1.8)

However, hydrogen peroxide has a small absorption cross section (18.6 M^{-1} cm^{-1} at 254 nm) [**31**], which results in low conversion of H_2O_2 to OH by UV. In addition, the rate of photolysis is also limited by the pH of the solution: acidic pH has a limiting effect on the generation of OH, making this method only truly useful for alkaline solutions [**39**]. This is not an insignificant fact, as common pollutants are acidic, with a range of 3.0 to 5.0 [**40**]. Increasing the pH could add significant cost depending on the pollutant chemistry [**31**].

1.1.2.2.3.3.3 Ozone and UV (O_3/UV)

In addition to functioning as a typical ozone system, the O_3/UV system also produces both atomic oxygen and hydroxyl radicals, which can increase efficiency (depending on contaminant chemistry). The oxidation processes in these systems is debated [**31**,**41**], but the general reactant production is as follows:

$$O_3 \xrightarrow{h\nu} O^1(D) + O_2$$

(1.9)

$$O^1(D) + H_2O \rightarrow H_2O_2$$

(1.10)

$$H_2O_2 \xrightarrow{h\nu} 2OH$$

(1.11)

The absorption cross section of ozone is much higher than that of hydrogen peroxide (3600 M^{-1} cm^{-1} versus 18.6 M^{-1} cm^{-1} at 254 nm [**31**]), which is attractive. One of the negative aspects of O_3/UV systems is the reaction of ozone with contaminants can quickly become mass transfer limited due to the rate of ozone dissolution, which implies an increase in operating costs [**42**].

1.1.2.2.3.3.4 H_2O_2/O_3, H_2O_2/O_3/UV

These systems are essentially combinations of the previously described methods. Adding H_2O_2 to an ozone system increases the decomposition efficacy of the system. The presence of

ozone decreases the contaminant load for the peroxide reactions, which typically have far faster reaction rates with organics then ozone. In practice, it is far simpler to add an H_2O_2 system to an existing O_3 system, as ozone generation relies on complex equipment (e.g., oxygen DBD) whereas hydrogen peroxide can be injected into solution as a liquid. When used in conjunction with UV, the hydrogen peroxide promotes ozone mass transfer throughout the liquid [**26**]. However, these systems are still inefficient for acidic solutions, and may need post-processing to remove residual ozone.

1.1.2.2.3.4 Summary

While AOP methods are effective, implementation costs are higher than conventional methods (refer to Table 1.2 for simplified cost comparisons). Additionally implementation is associated with increased system complexity; as a result, these methods are not in widespread use [**43**,**44**].

Table 1.2: Typical cost comparison between conventional and AOP water treatments.

	Treatment Rate (gal/min)	**Operating Cost ($/1,000 gal)**	**Note**	**Ref.**
Conventional Water Treatment	173.6	1.7 (2.29[9])	2001 (2015) dollars	[**45**]
	347.2	1.25 (1.69[9])		
	520.8	1.05 (1.42[9])		
	694.4	1.00 (1.35[9])		
AOP: $UV/O_3/H_2O_2$	732	0.86 – 4.47 (1.16 – 6.03[10])	2001 (2015) dollars	[**46**]
AOP: UV/O_3	20	19.49 (36.29[9])	1990 (2015) dollars	
	100	7.28 (13.56[9])		
	250	4.74 (8.83[9])		

1.2 Plasma-based Water Purification

1.2.1 Promising potential

Nonconventional AOPs, and most especially plasma-based AOPs, are a growing field with great promise. Unlike conventional AOPs used in water treatment (e.g., ozonation), which

[9] 1990 dollars to 2015 dollars conversion calculated using annual inflation of 2.52% from this period.

[10] 2001 dollars to 2015 dollars conversion calculated using annual inflation of 2.16% from this period

typically produce only a select few species (e.g., in conventional ozonation, only O_3 is produced), plasma AOPs have the ability to generate multiple reactive oxygen species at once. Refer to Table 1.3 for the oxidation potentials of common, highly reactive oxidants. Atmospheric air-water plasmas produce many of these prominent species, which are all more reactive than fluorine and chlorine (commonly-utilized oxidants in water treatment). Excitingly, combinations of these species have shown to have synergistic effects, displaying greater disinfection and decomposition efficiencies working in concert than in separate applications of each species [**47**,**48**].

Over the past decade, the research area of plasma based water purification has grown [**49**,**50**,**51**,**52**]. These plasmas have been shown to destroy organic contaminants, such as textile dyes [**53**,**54**,**55**,**56**] and antibiotics in aqueous solutions [**57**,**58**], as well as inactivating biological microorganisms [**59**,**60**].

Table 1.3: Oxidation potential of common oxidants [61**].**

Species	**Oxidation Potential (V)**
F_2	2.87
OH	2.80
O	2.42
O_3	2.07
H_2O_2	1.78
HO_2	1.70
Cl_2	1.36

1.2.2 Challenges

While the study of plasma discharges in gases is fairly established, breakdown in liquids is very much an underdeveloped field [**62**]. The interaction of plasma with liquid water and the transport of reactivity into the bulk solution is not well understood [**63**]. Numerous aspects of breakdown in liquid water are poorly understood, including breakdown initiation; streamer propagation; the effects of high electric fields on liquids; and efficiency (e.g., conversion, electrical, etc. efficiencies) [**64**].

1.3 Past Research and Approaches

A review of the main electrical discharges in water is given, followed by a historical overview of the evolution of the use of electrical discharges in water for water purification.

1.3.1 Overview of Discharge Types

Plasma discharges interact with water through three basic methods, and examples of each are illustrated in Figure 1.5: direct discharges, in which the plasma is ignited within the liquid volume itself; indirect discharges, where the discharge is initiated and primarily resides in a gas neighboring the treatment liquid, limiting plasma treatment to the surface of the liquid; and bubble or hybrid discharges, whereupon breakdown occurs within gas bubbles contained in the liquid water.

1.3.1.1 Direct Discharges

Direct discharges include corona glow, streamers, arcs, and sparks. Here, radicals are produced directly in the liquid, resulting in optimal flux [**65**,**66**]. Fridman et al. [**67**] have shown that direct plasmas provide quicker and more efficient deactivation of bacteria than indirect plasmas. However, the limitation of direct discharges is due to the high breakdown field associated with water (on the order of 1 MV/cm), associated with the large collision frequency of water [**68**]. Many authors believe microbubbles and voids are a requirement for plasma production in liquids (e.g. [**69**]), however Starikovskiy et al. [**70**] have provided evidence suggesting the ignition of plasma discharges directly in water without bubbles if sub-nanosecond high voltage pulses are applied. Direct discharges in water were some of the first approaches investigated for the purpose of sterilizing water. A summary of the main direct discharges and their relevancy for water purification and sterilization is given in Table 1.4. A summary of the main electrical characteristics of each discharge is given in Table 1.5.

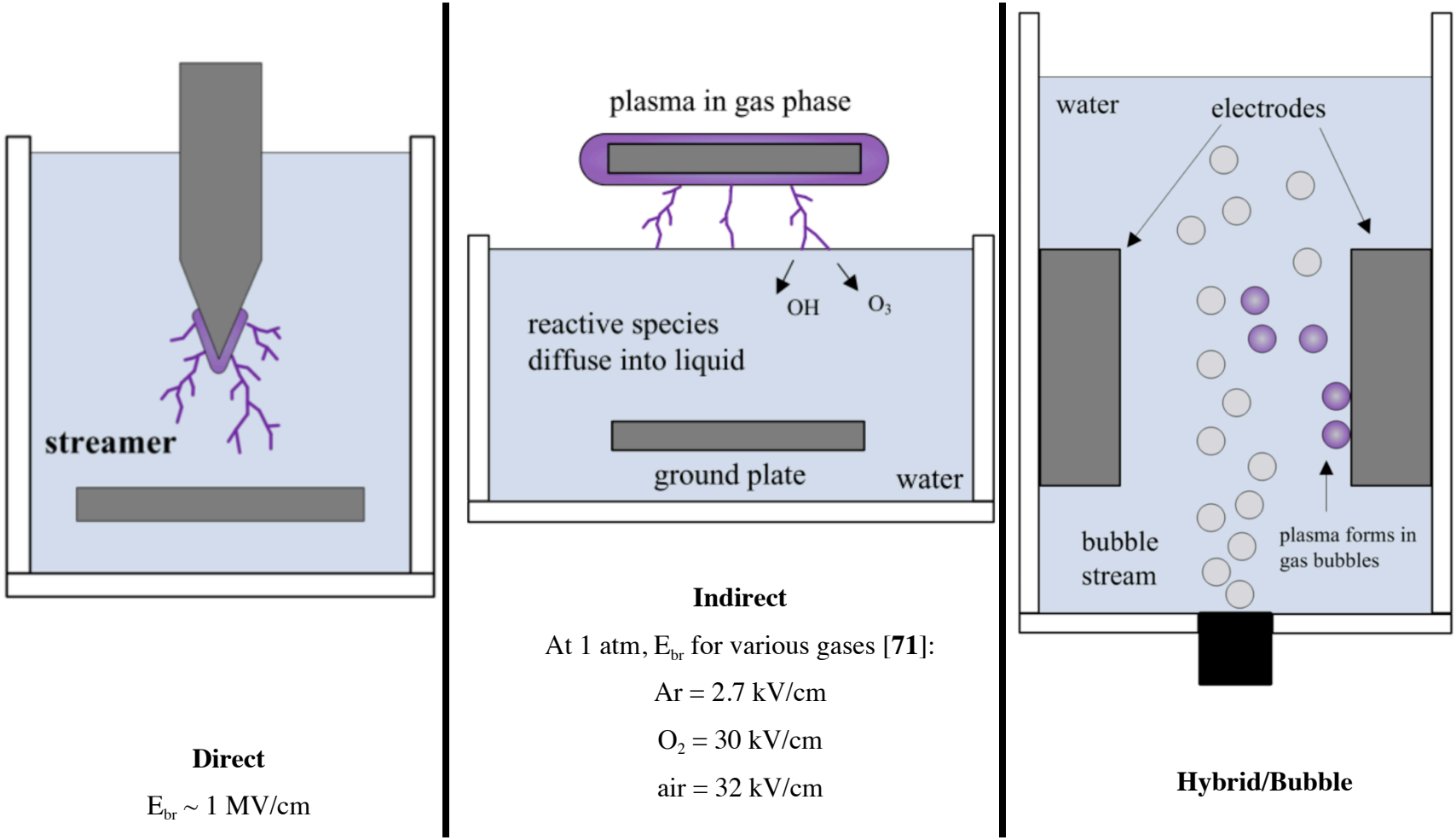

Direct

E_{br} ~ 1 MV/cm

Indirect

At 1 atm, E_{br} for various gases [**71**]:

Ar = 2.7 kV/cm

O_2 = 30 kV/cm

air = 32 kV/cm

Hybrid/Bubble

Figure 1.5: Various methods of producing plasma for water treatment. Adapted from [72] and [73].

Table 1.4: Summary of direct discharges in water and their water purification and sterilization efficacy. Adapted from [74].

	Pulsed corona	**Pulsed arc**	**Spark**
Energy per liter for 1-log reduction in *E. coli*, J/L	3×10^4 to 1.5×10^5	860	77
Power requirement for water processing at 1,000 gpm (gallons per minute), kW	1.9×10^3 to 9.5×10^3	54.3	4.9
Power available in small power system (10×10×10 cm), kW	0.3	30	10

Table 1.5: Discharge characteristics of the primary direct discharges. Adapted from [74].

	Corona and Streamer in Water	**Arc and Spark in Water**
Current Transfer	Mainly by ions	Electrons
Typical Peak Current	<100 A	> 1000 A
Temperature	Non-thermal plasma	Quasi-thermal Arc $> 1\times10^4$ K Spark $\sim 1\times10^3$ K
Discharge Energy	$\leq \frac{\text{J}}{discharge}$	$> \frac{\text{kJ}}{discharge}$
Electric Field Intensity	100 to 1×10^4 $\frac{\text{kV}}{\text{cm}}$	0.1 to 10 $\frac{\text{kV}}{\text{cm}}$

1.3.1.1.1 Corona Glow

Corona glow discharges are discharges in which the plasma occurs locally about the powered electrode. One such discharge is shown Figure 1.6. Unlike the streamer discharge (schematically depicted in Figure 1.5), the corona discharge tends to be localized at the powered electrode—which is typically sharp (generating a locally high, non-uniform field), (see Figure 1.7 for an illustration of the ionization region of the corona discharge). Corona discharges tend to be too weak to produce useful sterilizing quantities of UV [**74**].

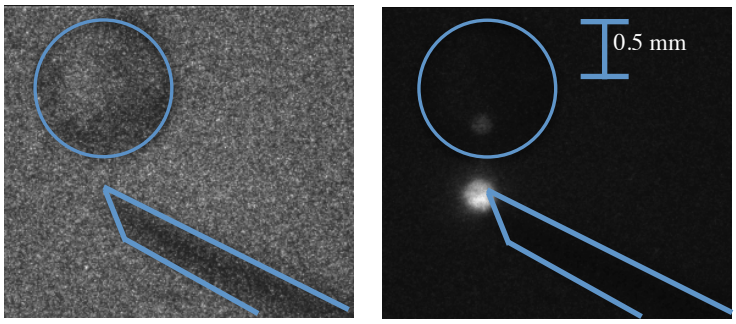

Figure 1.6: Corona discharge in a levitated bubble system. Pin electrode with levitated air bubble: before discharge (left), corona discharge on electrode tip due to 13.0 kV pulse (100 ns rise time, 1 μs pulse width). There is no breakdown in the bubble, only a reflection of the plasma at the electrode tip.

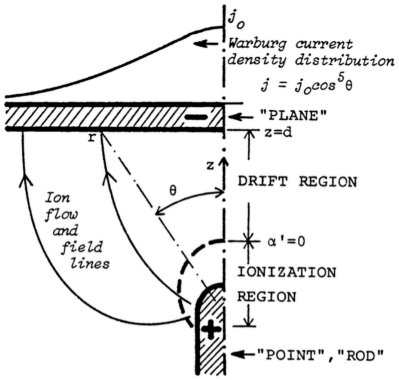

Figure 1.7: Anatomy of a positive corona discharge in a point to plane geometry. α'=0 is the spatial extent of the plasma, the boundary where ionization and attachment are equal. From [75].

1.3.1.1.2 Streamer

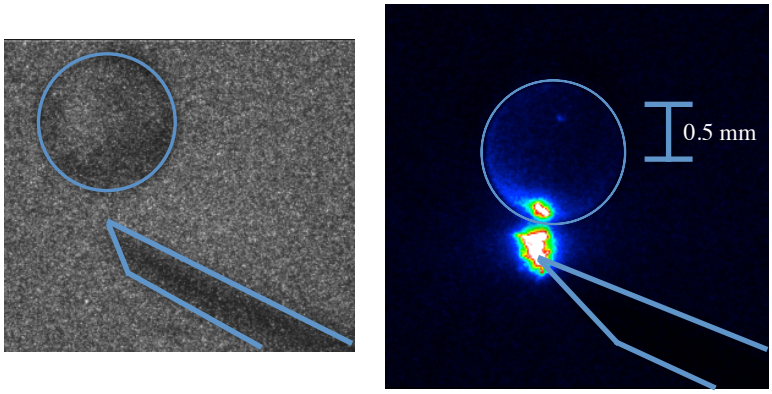

Figure 1.8: Liquid streamer between electrode and levitated air bubble. A glow discharge is ignited within the air bubble upon streamer contact. Applied voltage = 13.6 kV.

Coronas may transition to streamers if the Meek criterion is satisfied (discussed in detail in Chapter 2). Such a transition is illustrated in Figure 8. Here the corona first shown in Figure 6 intensified with applied voltage to become a streamer. The streamer channel diameter has been measured to be ~10-20 μm in width. Both coronas and streamers tend to have discharge energies of 1 J/pulse or smaller, and are typically created via direct current discharge [**76**] or with AC (typically up to a few kHz in frequency) for high power depositions [**77**].

1.3.1.1.3 Arc Discharge

Unlike many (but not all) coronas and streamers, arc and spark discharges bridge the inter-electrode gap. These discharges are high current, and much of the energy is diverted to heating the discharge channel, which also results in a quasi-thermal plasma. These discharges produce strong shock waves, which has an antimicrobial effect as the microorganisms, causing significant damage to the cells [**74**]. In addition, arcs are much more efficient at producing UV, which adds to the antimicrobial uses (see Table 1.4 for example case of *E. coli* deactivation through different discharge types).

1.3.1.1.4 Spark

Spark discharges are essentially shorter duration arcs. The shorter pulse allows for lower temperatures (see Table 1.5), which makes them more energy efficient (see Table 1.4). Sparks also create stronger shock waves as they propagate faster [**74**].

1.3.1.2 Indirect Discharges

Indirect discharges are discharges in which the plasma is ignited in a material (typically air) separate and adjacent to the liquid to be treated. Plasma-produced gas-phase species diffuse into the liquid whereupon liquid-phase chemistry occurs. Most indirect discharge systems utilize gases such as argon, helium, air, and oxygen [**69**,**49**,**50**]. Producing a plasma in the gas phase is more energy efficient than in the liquid phase, with breakdown voltages typically ranging from 1s to 10s of kV/cm [**74**,**78**]. The gas-phase plasma interacts with the liquid surface, diffusing into the liquid as well as creating additional species at the gas-liquid boundary. As the liquid-phase species are created secondarily, fewer radicals are created in comparison to direct discharges and in general these discharges have smaller mass yields than direct discharges [**73**,**79**]. Dozens of indirect discharge types exist [**69**,**49**]; a few of the major designs are illustrated in Figure 1.9. Thorough reviews of such devices may be found elsewhere [**49**,**50**,**69**].

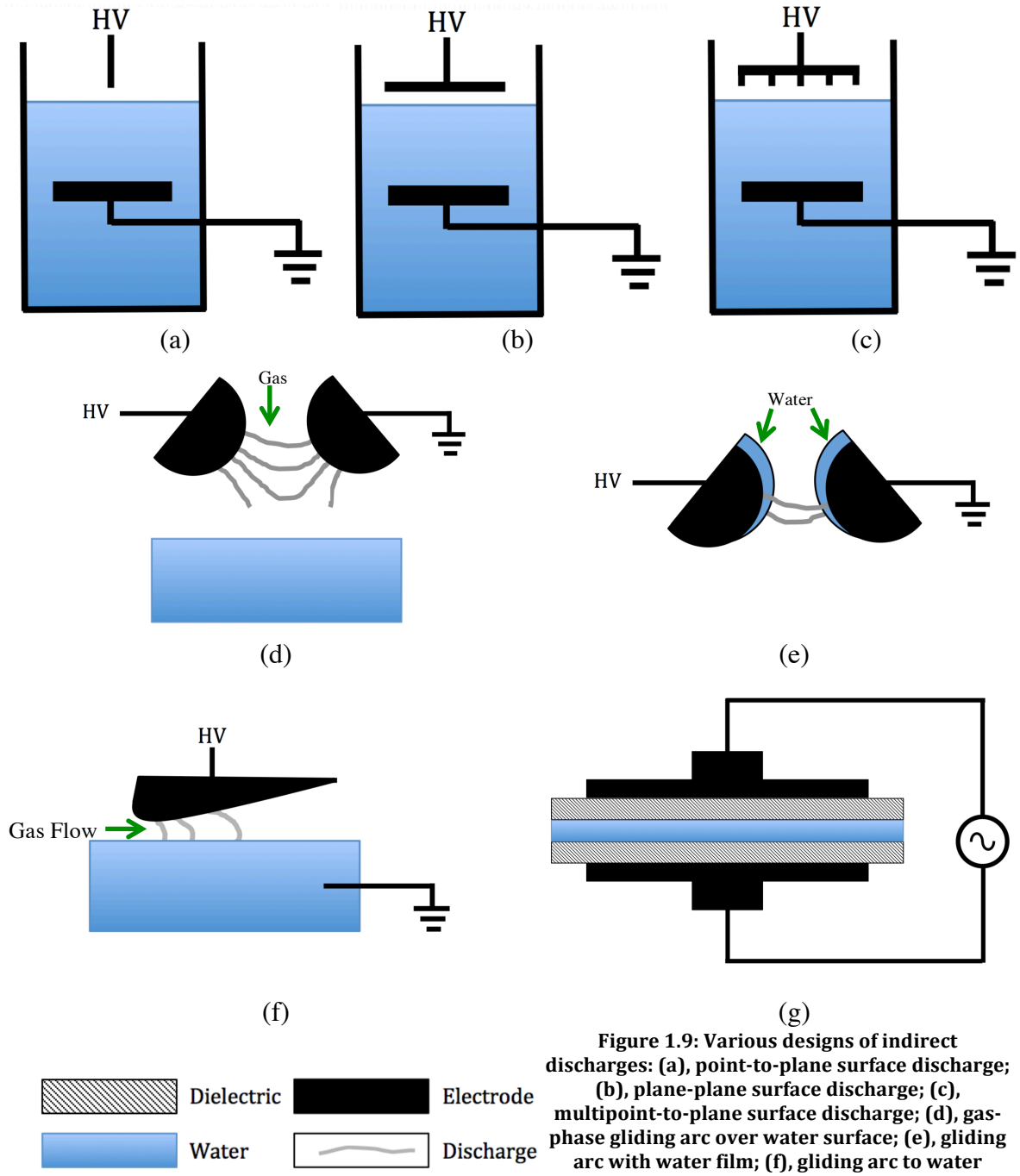

Figure 1.9: Various designs of indirect discharges: (a), point-to-plane surface discharge; (b), plane-plane surface discharge; (c), multipoint-to-plane surface discharge; (d), gas-phase gliding arc over water surface; (e), gliding arc with water film; (f), gliding arc to water surface; (g), dielectric barrier discharge.

1.3.1.2.1 Surface Discharge

Surface discharges, schematics shown in Figure 1.9a through c, are the most simple and commonly studied indirect discharges. These devices can be several orders of magnitude (reported up to ~2000x) more energy efficient than direct discharges, as measured by the G_{50}

value[11] [**50**]. These devices may be powered as DC, AC, or pulsed discharges [**80**,**81**,**82**], as point-to-plane or plane-to-plane devices [**83**,**84**], and may produce coronas, sparks, arcs, and DC discharges [**49**,**69**,**85**].

1.3.1.2.2 Gliding Arc

Gliding arcs (or sliding arcs or a "Jacob's ladder" discharge) have been studied with bare or liquid water layer electrodes, or with the treated water as the ground electrode [**86**,**87**,**88**]. Gas flows with and without water sprays are used for the gas-phase discharge [**89**]. Including water droplets increases efficiency by up to 400x [**90**]. In general, however, these reactors have low reactivity due to the low plasma exposure [**50**] (see Table 1.6).

1.3.1.2.3 Dielectric Barrier Discharge

Dielectric barrier discharges (DBDs) are constructed such that a dielectric material is on both electrodes. The presence of a dielectric barrier between the electrodes allows the discharge current to remain stable, i.e., runaway currents leading to arcing that are typically an issue at atmospheric pressures is prevented. First used by Siemens in 1857 to produce ozone (and considered by Siemens as one of his most important inventions [**91**]), DBDs are powerful sources of reactive species. Typical concentrations of hydrogen peroxide are in the range of 10s – 100s μM of H_2O_2 in water [**77**], concentrations that are able to destroy double-strand DNA within seconds [**74**]. DBDs can also be used air purifiers, and have high efficiency when pollutant concentration is below 1,000 ppm [**92**].

In 1932, Buss [**93**] determined the discharge typically occurs in the form of many micro-current filaments, which are typically a few hundred microns in width (it is possible to generate uniform glow DBDs as well [**94**]). The radii of streamer channels are correlated to the electronegativity of the gas, with oxygen DBDs have smaller streamer radii than air DBDs, which are smaller than helium DBDs [**91**].

A surface discharge (such as in Figure 1.9a through c) may be considered a dielectric barrier discharge in its simplest form. To increase plasma process area, Foster et al. [**95**,**96**,**73**] have

[11] This value, proposed by Malik [**50**], is a measure of the energy efficiency of a plasma reactor's ability to decompose 50% of the contaminant. This value is described in Chapter 3, section 3.4.5.2.

developed an underwater dielectric barrier discharge jet (see Figure 1.10). The system is a coaxial design with the excited electrode (1-5 kHz, 1-10 kV) surrounded by a quartz discharge tube with the ground electrode around the base of the tube. In this configuration, the discharge is created within a gas pocket that is submerged within the treated water. The gas pocket is either pumped down the tube from an external source [**53**] or self-generated [**77**]. Typical decomposition rates of methylene blue dye possible are on the order of 93% reduction in concentration after 7 minutes of plasma processing. Other DBD designs to maximize surface reactivity include the use of porous ceramic or glass frit in between electrode and liquid, which allows for significant transmission of species to the liquid while preventing significant gas-liquid mixing [**81**].

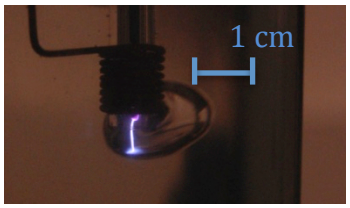

Figure 1.10: Dielectric barrier discharge in water. Argon is the feed gas. [97]

A comparison between gliding arc discharges and dielectric barrier discharges may be found in Table 1.6. DBDs are some of the most efficient discharges for processing contaminated water.

Table 1.6: Discharge characteristics of gliding arc discharges and dielectric barrier discharges.

	Electron Density	**Electron Temperature**	**Operating Voltage**	**Discharge Power**
Gliding Arc	10^{11}-10^{15} cm^{-3}	0.1 – 0.5 eV	10-15 kV	100 - 1000 W
DBD	10^{14}-10^{15} cm^{-3}	1 – 10 eV	~100 V to 10s kV	10s W to 1s MW

In the field of plasma medicine, dielectric barrier discharges are also important: Fridman et al. [**67**] have shown that direct plasmas provide quicker and more efficient deactivation of bacteria than other commonly used medical plasmas, such as needles, jets or torches. In medical DBDs, the dielectric is atmospheric air and the treated tissue takes the place of the ground electrode. This requires the plasma to be pulsed quickly (microseconds [**98**] to nanoseconds [**99**])

to reduce thermal damage. DBDs have been shown to have significant effect on cancer cells, with numerous in vitro [**100**] and in vivo [**101**] studies performed. Medical DBDs, however, at their current technological stage of development have the downside of operating very close (i.e., millimeters) away from the treated tissue, limiting the application.

1.3.1.3 Hybrid or Bubble Discharges

Bubble discharges are a hybrid of the two former methods, and are attractive as they are believed to combine the lower energy requirements of indirect discharges with the greater radical generation of direct discharges [**69**,**73**,**102**,**103**,**72**]. Several discharge schemes exist (see Figure 1.5 for one such design), examining single or attached bubbles physically on an electrode [**104**,**105**,**106**], or bubbles separated from the electrodes by water. Two current methods of isolating bubbles are either by acoustic levitation [**63**,**107**] or through a rising stream [**108**,**109**]. Breakdown of isolated bubbles is an attractive engineering goal as it offers the prospect of increasing the treatment volume via the induction of breakdown of a matrix of bubbles within a volume of water. This would allow for high production rate of radicals within the liquid directly and may also accommodate high throughput.

However, the presence of both liquid and gas presents a complicated environment in which to study breakdown processes. To date, no breakdown condition has been established for underwater bubbles, nor is it clear how analogous bubble discharges are to atmospheric pressure streamers. It is uncertain what factors determine the region (gas or liquid) over which the plasma forms [**62**]. Understanding these discharges would have significant impact on multiple physical problems; indeed, a fundamental characterization of the bubble breakdown process is an integral part to the development of plasma-based water treatment.

1.3.1.3.1 Electrode-Attached Bubbles

The point of highest electric field strength is at the electrode surface [**110**]. Motivated by this fact, several plasma water treatment experiments and simulations have examined the concept of bubble-based discharges with bubbles attached to the electrode [**111**,**112**,**113**,**104**]. These studies have revealed various important characteristics of breakdown within bubbles in water. Tachibana and Takekata [**104**] observed discharges in bubbles of noble gases formed diffuse

channels within the bubble volume, whereas in molecular gas bubbles, the breakdown occurred as a streamer strictly along the bubble boundary. In addition, the importance of the dielectric surface and permittivity of the surrounding liquid has been computationally demonstrated to determine the discharge path: large permittivity liquids (such as water) affect the discharge such that the streamer travels along the interface between gas and liquid [**114**]. These discharges are sources of radicals (e.g., hydrogen peroxide production rate measured by Yamabe et al. [**105**] to be 19-27 mg/h, an order of magnitude below the hydrogen peroxide production rates (up to 550 mg/h) of the steam discharge developed by Gucker and Foster [**77**]); Yamabe et al. achieved 67% concentration reduction after 30 minutes of processing time of indigo dye solutions via large (i.e., ~24 μL in volume) attached bubble discharges.

1.3.1.3.2 Isolated Bubbles

One method of producing plasma in bubbles is through the use of a rising stream, traveling between the electrodes [**108**,**109**] (similar to Figure 1.5). Because these tests were focused on demonstrating the efficacy in producing chemical species, little emphasis was placed on determining the exact nature of the discharge. It is unclear if the rising bubbles need to be in contact with the electrodes for plasma ignition to occur.

Another method of inducing plasma in isolated bubbles was developed at the University of Michigan by Sommers [**72**] and investigated by Sommers et al. [**106**,**107**] and Gucker et al. [**63**,**115**]. Here, the bubble is trapped in an acoustic pressure field within the liquid water volume, suspending the bubble and allowing for the application of voltage using electrodes of various geometries. This method allows for the ignition of plasma in the bubble both through contact by a liquid streamer, which induces a glow discharge of the gas within the bubble, and for isolated breakdown, with plasma believed to be confined to the bubble only [**116**,**107**]. Simulation of plasma excitation in a multiplicity of gas bubbles by Babaeva and Kushner [**114**] indicate that it may even be possible to communicate streamer ignition between adjacent bubbles.

1.3.2 Evolution of plasma water purification

1.3.2.1 Ozone

> *Then Zeus roared out his thunderand with a bolt of lightning struck our ship. The blow from Zeus' lightning made our boatshiver from stem to stern and filled it upwith sulphurous smoke.*
>
> The Odyssey*, Homer, Book XII Verse 542, trans. Ian Johnston*
>
> *One of the first records of recognizing "sulphurous" odored ozone production*

As mentioned previously, AOPs are processes that consist of the creation and utilization of highly oxidative species (primarily OH radicals but also includes O_3, H_2O_2, etc.). Ozone was one of the first AOP-type species experimentally detected, and was discovered in early electrical discharge experiments. Ozonation, the treatment of water or other substances with ozone for sterilization and the like, is currently the only water purification method in conventional use that utilizes electrical discharges [**117**].

In 1785, Martinus van Marum first noted the presence of ozone, the "odour of electricity," during his electrostatics experiments. Though he did not identify ozone as an allotrope of oxygen, he did hypothesize the gas must be from air or oxygen that had experienced an electrical discharge, and had the ability to tarnish mercury [**118**,**119**]. Officially discovered by Christian Friedrich Schönbein in 1840, Werner von Siemens created the first ozone generator, one of the first dielectric barrier discharge devices, in 1857 [**120**].

Since 1854, chlorine was used in water treatment due to its effectiveness against cholera [**20**]. However, chlorine was soon discovered to cause respiratory disease, prompting a search for another disinfectant. Ozone was identified as a powerful oxidizer, and the specific application of ozone for water purification on a commercial level began in 1906 in Nice, France [**20**].

Today, ozone is still regarded as a powerful water-sterilizing agent with numerous advantages [**121**] (refer to Chapter 2 for further discussion). However, engineering challenges presented by conventional ozone generation methods, including dealing with such a highly corrosive material and on-site generation (high energy, typically via corona discharges and oxygen gas), make the capital costs high [**122**]. Currently almost 300 major water treatment plants in the United States use ozone as a part of the treatment process, including Los Angeles,

California (continuously since 1987); Dallas, Texas (1993); Ann Arbor, Michigan (initially from 1911-1915, continuously since 1996); and Seattle, Washington (2000).

1.3.2.2 Early 20th century

The first work on electrical discharges in water for water purification date back to the turn of the 20th century. These works may be found in scholarly journals, but mainly patent applications and reports. While many of the efforts described in these texts report mediocre results (this is most likely due to a lack of scientific understanding of electrical properties and a materials/power generation issue), the development of electrical discharges in water may be traced from the 1890s onward. Several designs of water purification devices induced arcs throughout the water main or holding drum [**123**,**124**,**125**]; one illustration of such a device may be found in Figure 1.11. One of the first texts to identify precipitates forming in water subjected to electrical discharges may be found in a patent filed in 1905 [**126**]. Other designs investigated include combinations of ozonation and (it is assumed) glow discharges [**126**,**127**]. Failed attempts include the use of electromagnets after arcs in an attempt to separate out microorganisms [**125**].

It is interesting to note many of the techniques that were attempted by early investigators are in use today, both in the experimental laboratory setting and in conventional use. For example, the use of strong magnets for magnetic separation of contaminants in water is today a frequently used water purification technique used in ore mining industries, anti-scale treatment of pipes, removal of organic and inorganic contaminants (once sorbed by magnetic colloid) and nanoparticle filtering [**128**,**129**,**130**,**131**].

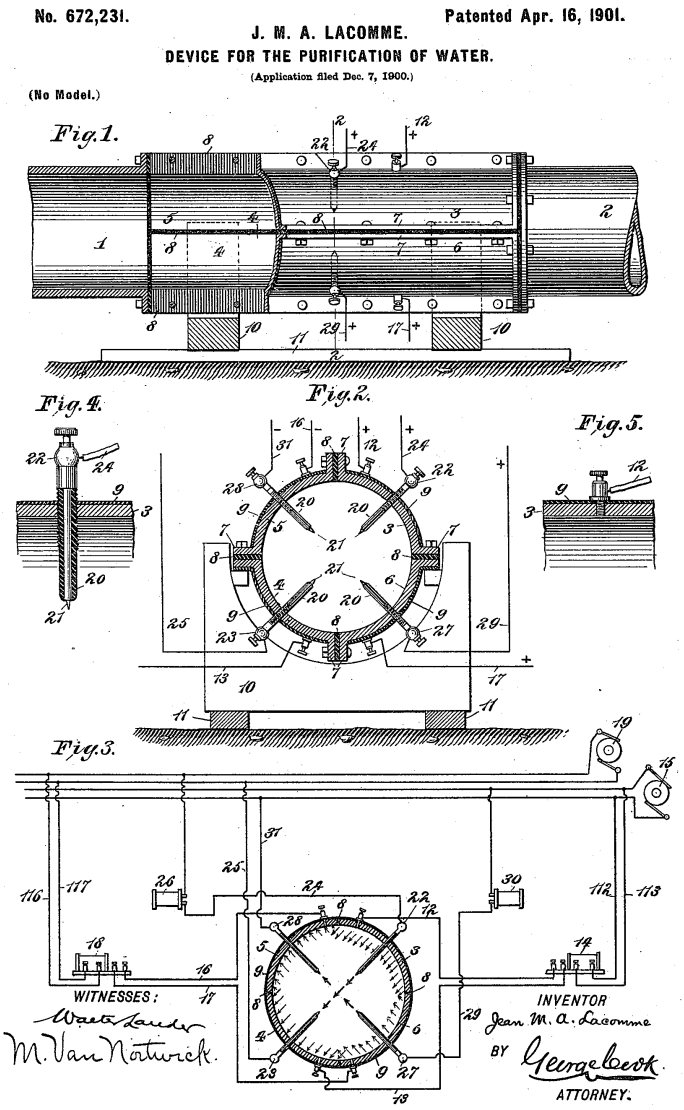

Figure 1.11: "Device for the purification of water", art from patent filed in 1900 [123]. The water is treated via arc discharge as it passes through the electrodes (labeled 21 above).

1.3.2.3 Mid-20th century

After the initial investigations of the 1900s and prior to the 1960s, the interim decades did not see many substantial contributions to discharges in water with the goal of purification though knowledge of radical production from discharges in water vapor was advanced [**132**,**133**]. Electrohydrodynamic experiments during this time period were primarily limited to prefect conductors (e.g., mercury or water) or perfect dielectrics (i.e. apolar liquids, e.g., benzene) [**134**].

Many fundamental investigations that would establish the field of electrical discharges in water as understood today began in the 1960s. Allan and Mason first analyzed the effect of

electric field stress on a liquid "leaky" dielectric in 1962 [**135**], introducing the study of electromechanical effects on poorly conducting liquids (a material with finite conductivity (e.g., deionized water, ~μS/cm) versus a perfect dielectric, which has zero conductivity). Many groups studied the formation of shock waves due to plasma arcs in liquid water [**136**,**137**,**138**]. Brandt et al. [**139**] were some of the first to study the effect of electrical discharges in water on microorganisms, noting that what is now called plasma-activated water[12] by some authors (e.g. [**140**]) was identified as having strong bactericidal effects. Further studies by the group noted *Escherichia coli* was efficiently deactivated through electrical arcs in water [**141**], an effect that was not related to the arc-induced shock wave [**142**]. They also demonstrated arc-produced UV radiation had a significant effect on bacterial death [**143**]. Radicals, especially OH, produced by water vapor in a microwave discharge at reduced pressures were also studied during this time [**144**,**145**]. By the end of the decade, chemical reactions resulting from electrical discharges in gases were firmly established (e.g., [**146**]), but the formalization of the liquid counterparts was still obscure.

Electron beam irradiation of contaminated waters for sterilization was investigated beginning in the 1970s, though much of the work was done in the 1990s-2000s. While electron beams in aqueous solutions were studied to determine reaction rates over the previous decades [**147**,**148**], this time period saw the beginnings of direct use of electron beams as a water cleaning method. Electron beams have been used to decompose various dyes [**149**], organics such as glycol ethers [**150**], aromatic hydrocarbons [**151**]. A nonconventional AOP, treatment by electron beam is primarily due to the creation of hydroxyl radicals from the excitation and ionization of water. However, electron beams are not very significant OH producers; the G-value (number of reactions per 100 eV of electron beam energy) of OH production is only 2.6-2.7 [**151**,**152**]. Consequently, complete mineralization of contaminants is often not realized [**151**] or multiple methods used in concert are required [**150**].

[12] i.e., water that has been subjected to electrical discharges and contains various reactive oxygen and nitrogen species (RONS), such as OH, H_2O_2, NOx, etc.

1.3.2.4 Late 20th century

One of the first studies of plasma discharges in liquids for contaminant degradation was completed in 1987 by Clements et al. [**153**]. The reactor investigated used a point-to-plane pulsed streamer corona discharge and bubbled gas (various ratios of N_2 and O_2) from the base of the reactor vessel, which facilitated the decomposition of dye, the contaminant used in the study. When operated with O_2, this device was observed to be a strong ozone producer as well as a more efficient method of decomposing contaminants than electron beam irradiation of contaminated water.

The 1990s saw rapid growth for plasma-driven water purification [**154**,**155**,**156**]. Degradation of various contaminants in aqueous solutions by various discharges were demonstrated, including phenol [**152**] and microorganisms [**157**]. Radical production was noticed to depend on not just feed gas used, but also discharge type [**155**,**158**]. Liquid phase reactors were developed by various authors (e.g., [**159**,**156**,**160**]), with various approaches to circumvent issues such as arcing between electrodes. Two main methods used to avoid arcing included using dielectric barrier discharges [**161**] and pointed electrodes for corona discharges [**162**]. As an example, Šunka et al. [**163**,**164**] developed a pulsed streamer corona system with a porous ceramic electrode cover that increased plasma volume, as well as reduced electrode tip wear (reduced arcing issues between electrodes). In addition, numerous gas phase reactors (e.g., [**165**,**166**,**167**]), in which the plasma is produced in the gas adjacent to the treated liquid, were developed. (See following section for discussion on various discharge types.)

Capitalizing on the decontamination and sterilizing ability of plasmas in liquids, the 1990s also marked the beginning of plasmas applied to the biomedical arena [**168**] and general surface sterilization (e.g., treating surfaces contaminated with biological and chemical warfare agents [**169**,**170**]). The *in vivo* biological environment (cells) is 65-90% water, thus the field of plasma medicine is interrelated with much of the scientific efforts of plasma water purification. Plasmas for medical applications are currently being investigated and successfully applied for many medical areas, including dental [**171**]; dermatology, including wounds [**172**] and cosmetic procedures [**173**]; emergency services, such as aiding in blood coagulation [**174**] and surgical tools [**175**].

1.3.2.5 Early 21st century and Today

Today, many different reactor designs for plasma water purification have been investigated and presented in the literature [**50**,**176**,**73**]. However, this makes comparisons between reactor types difficult, and researchers are confined to drawing comparisons to disparate elements of each reactor, such as hydrogen peroxide production [**177**] or relative energy yield (i.e., energy required to convert 50% of pollutant, as in [**50**]); however, these comparisons are limited in usefulness due to unaccounted characteristics, such as operating cost (e.g., high flow rates (~10+ SLPM) of expensive gases, such as helium) or different reaction chemistries (due to the pollutant or processing materials, etc.). A standardized reactor cell, an analogue to the Gaseous Electronics Conference Reference Cell [**178**], is strongly suggested [**73**].

1.3.2.5.1 From Bench-top to Conventional Use: Scaling Up, Current Considerations and Challenges

Though input power, applied voltage and discharge current are kept essentially identical, contaminant decomposition increases in degradation rate with increasing number of applicators, regardless of discharge type. Two examples include (1), the use of two underwater DBD air jets has been shown to decompose methylene blue solutions to concentrations 250 times lower than a single jet at identical input powers and treatment times [**179**], and (2), multi-needle-to-plate pulsed corona discharges are seen to decolor acid orange solutions twice as quickly when the number of active discharge electrodes are increased from four to seven for identical operating parameters [**180**]. The correlation between increased decomposition with increased applicator number is believed to be primarily due to an increase in the interfacial region between plasma and liquid, resulting in greater flux throughout the volume of plasma-driven species into the bulk liquid.

In addition, more applicators can also result in increase in species generation, though this aspect is complicated in that chemical interactions come into play and may limit the creation of species. Studies regarding multiple applicators or discharges must be completed, as species production is not simply additive with increasing discharges. Chang and Wu [**117**] noted fixed power systems with a single dielectric barrier discharge produce more ozone than systems with an addition dbd. Additionally, numerous multi-discharge interaction issues (such as multi-jet arrays) have been identified, including surface charge [**181**] and mismatch between applied

voltage and memory voltage [**182**]. Atmospheric jets may interact with each other not just electrostatically, but also hydrodynamically and through photolysis [**183**]. Successful stabilization of 7+ jet arrays have been achieved through the use of a capacitive ballast [**181**]; stabilization is very much an active area of research.

1.4 Goal and Focus of Dissertation

The chief goal of this dissertation is to lay the fundamental stepping-stones to progress toward a plasma-based water purification technology. The chief focus of this research is to understand the nature of breakdown in bubbles in liquid water and then focus on the operation and chemical effectiveness of a specific plasma source which may have some potential as the basis of a water purification system. These goals are accomplished through careful examination into the breakdown processes of gas bubbles in liquids and the associated plasma-driven chemistry.

1.5 Scope of Dissertation

To attain these aforementioned objectives, this dissertation approaches the topic of plasma water purification through the perspective of the gas bubble in liquid with breakdown throughout. This work uses a combination of physics and chemistry to examine the bubble, the surrounding liquid and the electrical discharge itself through a series of experiments. Specifically, this dissertation:

1. Investigates some of the breakdown mechanisms of attached and unattached gas bubbles. This is accomplished through:
    a. Study of general plasma production in attached and unattached air bubbles,
    b. Study of the innate properties of gas bubbles and water and their effect on plasma discharge,

    and through:
    c. Study of the breakdown voltage scaling of bubbles of varying diameters.
2. Examines large-scale water-plasma systems. This is important in the assessment of plasma as a water purifier. This is brought about through:
    a. Study of resulting plasma parameters and identifying “knobs” for species control,
    b. Study of decomposition efficacy for various pollutants,

c. Cytotoxicity studies,

and by:

d. Development and study of a novel discharge that avoids acidification

3. Development and demonstration of a new method for interrogation of the plasma-liquid interface region and reaction zone.

Experimental methods used to accomplish these objectives include:

1. Optical techniques (e.g., high-speed photography, optical emission spectroscopy, photo diode, intensified charge-coupled device (iCCD) camera),

2. Chemical diagnostics and chemical probes (e.g., pH, conductivity, DO, species concentration (e.g., mass spectrometry via gas chromatography (GC/MS), ion chromatography (IC/MS), , and high-performance liquid chromatography (HPLC)), decomposition studies (e.g., methylene blue (MB), halogenated compounds, Methyl Orange, algae), etc.),

and

3. Physical methods (e.g., power studies, VI analysis, temperature measurements).

Computational methods used to accomplish these objectives include:

1. Electric field simulation via *ANSYS Maxwell*,
   and
2. Plasma chemistry simulation via *GlobalKIN*, developed by M. J. Kushner and associates [**184**,**185**,**186**].

Chapter 2:

Theoretical Review of Electrical Discharges in Water

This chapter gives an overview of the theoretical basis of this dissertation research. The science behind electrical discharges in gases and liquids is examined. An overview of essential chemistry initiated by the plasma discharge is summarized.

2.1 Gas-phase Breakdown

Electrical discharges in liquid water have been historically derived from gas-phase studies, which are more clearly understood than discharges in liquids. It is still unclear to what extent gas-phase breakdown is analogous to liquid-phase breakdown. Despite this unknown, even if liquid-phase breakdown involves additional, not well understood processes, gas phase processes are still expected to play an important role owing to the presence of gas bubbles either pre-existing within the liquid or formed via electrical influences (e.g., Ohmic heating, electrolysis) [**110**,**73**,**69**].

2.1.1 The Townsend Discharge

An electron in an electric field E will be accelerated to an energy ε as it travels a distance d.

$$\varepsilon = eEd = \frac{1}{2}mv^2 \quad \textbf{(2.1)}$$

In a sufficiently high field (e.g., imparting [ionization] energy ε to the electron of at least 12.2 eV for N_2 or 15.5 eV for O_2), a collision with neutral particles results in electron impact ionization. Electron-ion pairs are produced grows exponentially as governed by α, the first Townsend coefficient (see Figure 2.1). The density of electrons grows as an exponential function of distance x starting from the seed electron density n_0:

$$n(x) = n_0 e^{\alpha x} \quad \textbf{(2.2)}$$

The collisional process resulting in the exponential growth given by (2.2) is known as a Townsend avalanche (see Figure 2.2).

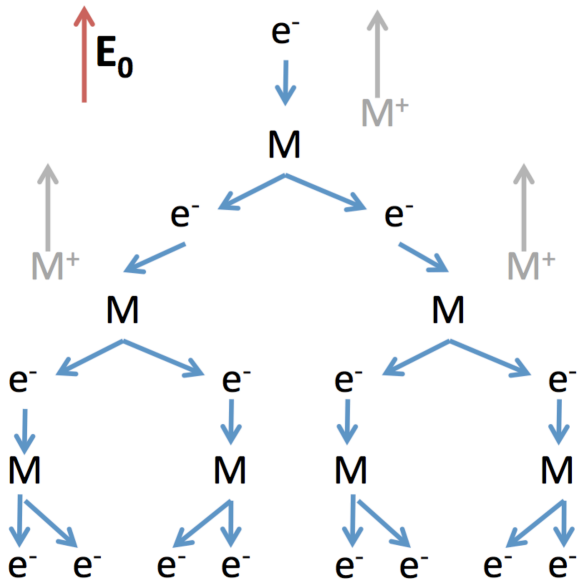

Figure 2.1: Schematic of the electron avalanche process in a gas. M represents a neutral gas molecule. In this schematic, $\alpha = 2$.

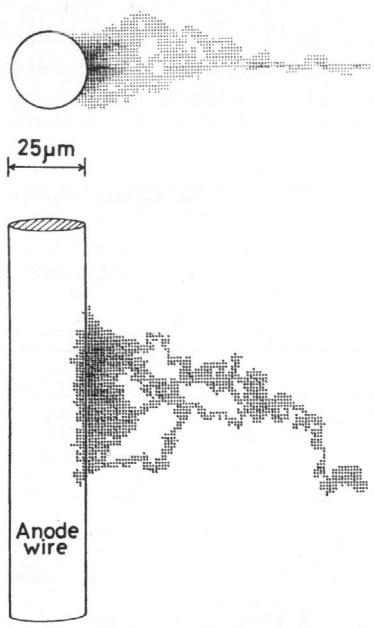

Figure 2.2: Monte-Carlo simulation of an avalanche created by one electron as it journeys toward a wire anode [187].

Note that α is not an intrinsic quality (i.e., it is an extensive property) of the system, but is rather a function of intensive properties of the system; α, ionizations per unit length, is defined via the neutral particle density N, electron drift velocity v_d, ionization cross section $\sigma_i(\varepsilon)$ and the electron energy distribution $f(\varepsilon)$ (see (2.3) below). A more general form, in terms of the mean free path of inelastic electron-neutral collisions, λ_e, the energy gained between collisions, $E\lambda_e$, and the ionization energy, ε_i, is also given (2.4).

$$\alpha = \frac{N}{v_d}\int \sigma_i(\varepsilon)\left(\frac{2\varepsilon}{m}\right)^{1/2} f(\varepsilon)\mathrm{d}\varepsilon \ [\mathrm{cm}^{-1}] \tag{2.3}$$

$$\alpha = \frac{\text{const}}{\lambda_e}\exp\left(-\frac{\varepsilon_i}{E\lambda_e}\right)[\mathrm{cm}^{-1}] \tag{2.4}$$

Additional sources of electrons, termed secondary electrons, that may initiate more avalanches include

1. Electrons freed from the cathode surface upon positive ion impact
2. Electrons released from photoemission via excited molecule-emitted photon (e.g., [**188**])
3. Electrons released during atomic collisions with metastables (e.g., [**189**]).

Similarly to the first ionization coefficient α, the total number of secondary electrons emitted is given as γ. Including secondary electrons in (2.2), the total density of electrons that reach the anode distance d away becomes

$$n = \frac{n_0 e^{\alpha d}}{1 - \gamma(e^{\alpha d} - 1)} \tag{2.5}$$

For energies typically associated with atmospheric discharges in liquid water (i.e., E/N[13] ≈ 100s of Td[14,15] [**190**]), water has a low secondary electron emission coefficient, γ, typically taken to be 2×10^{-4} [**191**].

Electrons produced in the avalanche are subject to both diffusion and attachment. Attachment can be especially significant in high electronegativity gases such as air and water vapor, and may even prevent the avalanche from propagating. Electron attachment in dry[16] atmospheric pressure discharges typically occurs as either dissociative attachment (2.6) or three-body attachment (with arbitrary third body M, (2.7) [**192**,**193**]:

$$e^- + AB \longrightarrow A^- + B \tag{2.6}$$

[13] The reduced electric field, E/N, which is the applied electric field E divided by neutral gas density N, is a parameter that can succinctly characterize several parameters of an electron in equilibrium, including average electron velocity, v_e, and the electron energy distribution function, $f(\varepsilon)$ [**192**]. The reduced electric field is used frequently in this work.

[14] 1 Td = 10^{-17} V cm^{-2}.

[15] For example, optimal ozone generation in pure oxygen is ~ 140 Td, ~200 Td in air [**96**,**72**]; computer simulations of atmospheric dielectric barrier discharges in air on human skin (for plasma medicine applications) predict reduced fields as high as ~630 Td [**74**].

[16] i.e., not humid, no water vapor. Ignoring trace molecules, such as CO and CO_2, negative ions are all due to oxygen [**200**].

$$e^- + A + M \longrightarrow A^- + M$$

(2.7)

In atmospheric pressure discharges, the electron attachment coefficient, η, scales with N, the neutral gas density. For dissociative attachment, this scaling is $\eta \propto N$, while for three-body attachment, $\eta \propto N^2$. Three-body attachment relies on *M* to conserve energy and momentum, and is thus more important at higher gas densities; therefore, low values of E/N (~ 0.1-10 Td) are dominated by three-body attachment and are a sensitive to density changes [**194**,**78**]. Conversely, dissociative attachment becomes important at higher electric fields. At atmospheric pressures, it is imperative that the reduced electric field (given as E/N) is large enough to counter these processes if the avalanche is to be maintained. Similarly to α and γ, units for η are attachments per unit length. Including attachment processes, (2.5) becomes [**193**]:

$$n = n_0 \frac{\left(\frac{\alpha}{\alpha-\eta} e^{(\alpha-\eta)d}\right) - \left(\frac{\eta}{\alpha-\eta}\right)}{1 - \frac{\gamma\alpha}{\alpha-\eta}\left(e^{(\alpha-\eta)d} - 1\right)}$$

(2.8)

The Townsend breakdown criterion for attaching gases (that is, the criterion for the avalanche electron density to grow to infinity) is found by setting the denominator of (2.8) to zero:

$$1 - \frac{\gamma\alpha}{\alpha-\eta}\left(e^{(\alpha-\eta)d} - 1\right) = 0$$

(2.9)

In the case of atmospheric discharges, where the gas number density *N* is large, the breakdown criterion becomes

$$\alpha - \eta - \alpha\gamma\left(e^{(\alpha-\eta)d} - 1\right) = 0$$

(2.10)

When γ is very small, as the case with water, the third term on the left hand side of (2.10 may be neglected, and the criterion reduces to

$$\alpha = \eta$$

(2.11)

It should be noted that (2.11 refers to the equilibrium point of the breakdown: that is, the breakdown electric field E_{br} in electronegative gases [**195**]. If ionization is equal to attachment, the avalanche cannot exist. (2.11 is rewritten as a limit to arrive at the breakdown criterion.

$$\alpha > \eta \tag{2.12}$$

In practice, it is experimentally difficult to independently measure ionization and attachment coefficients of electronegative gases at high (>100 Td) E/N values, as ionization typically dominates above this threshold, making determining the effect of attachment difficult in large fields [**192**,**195**]. As mentioned previously, for atmospheric pressure plasmas in electronegative gases, commonly encountered reduced electric field values are 100s of Td, and thus it is more convenient as well as more accurate to use the apparent ionization coefficient, λ:

$$\lambda(x) = \alpha(x) - \eta(x) \tag{2.13}$$

λ must be a positive value for the discharge to occur, which is merely a restatement of (2.12). The reduced apparent ionization coefficient for dry air over a range of E/N is shown in Figure 2.3.

Additional processes that occur in an avalanche that are not considered in this work include electron detachment (the process of adding electrons to the avalanche through removing electrons from anions), or photon-related processes, such as radiative attachment (electron impact causing attachment and the release of a photon) or photoionization. A detailed discussion on the chemistry resulting from electron collisions may be found in the Plasma Electrons subsection further in this chapter.

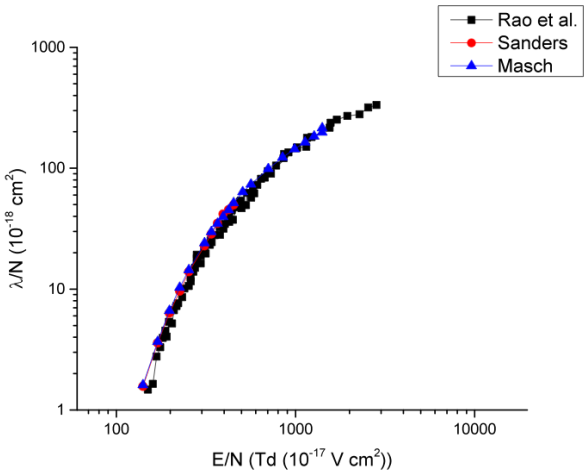

Figure 2.3: The reduced apparent ionization coefficient with E/N for dry air [192,196,197,198**].**

2.1.1.1 Effect of Humid Air

It is well known that the presence of water vapor in air (i.e., humid air) will increase the sparking potential of air for both positive and negative polarities [**199**]. This is an expected result, as oxygen, air and water vapor are electronegative gases[17]. Breakdown in the presence of water vapor is an important consideration in that discharges that occur in liquid via bubbles propagate through bubbles containing admixtures of air-derived gas and water vapor. Unfortunately, electron swarm data for humid air in E/N range of threshold to 1000 Td does not exist [**200**]. In this case, one must rely on published findings on the effect of humid air on breakdown.

Figure 2.4 shows the reduced attachment coefficient η/N for humid and dry air over a range of E/N from threshold to 100 Td. As expected, humid air has a greater η/N, due to the presence of H_2O. Figure 2.5 presents the reduced ionization and attachment coefficients over a narrow range of E/N, but the observed trend matches the overall trend of ionization dominating at greater E/N values [**200**]. Based on these (albeit limited) data, the data in Figure 2.3 is taken as a reasonable estimate for the reduced apparent ionization coefficient, as the primary difference between humid and dry air is believed to be stronger attachment due to the presence of water molecules.

[17] Electronegative refers to the tendency of the atom or molecule to attract electron bond pairs. Examples of non-attaching gases include hydrocarbons (e.g., methane, propane), nitrogen, and mercury [**200**].

However, the E/N values that are used within this work are greater than 100 Td, so it is also believed that these large electric fields promote ionization above attachment.

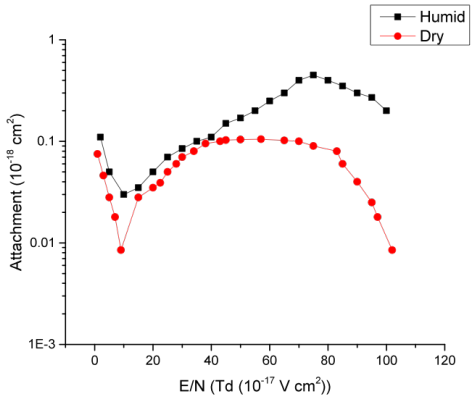

Figure 2.4: Reduced attachment coefficients for humid and dry air. From [201].

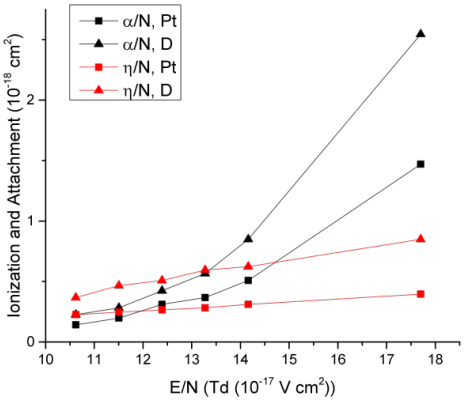

Figure 2.5: Reduced ionization and attachment coefficients for humid air. Ionization, black points; attachment, red points. Square points indicate platinum electrodes used; triangles, Dural (Al95%/Cu4%/Mg1%) electrodes. Adapted from [193].

2.1.1.2 Breakdown Scaling: Paschen's Law

In the absence of attachment and multiple ionizations, the reduced ionization coefficient, α/N, is dependent on E/N only, as given by the semi-empirical formula derived by Townsend (2.14), rewritten by Raju [**200**])

$$\frac{\alpha}{N} = F * \exp\left(-G\left(\frac{E}{N}\right)^{-1}\right), \tag{2.14}$$

where F and G are empirically derived gas constants [**195**,**202**,**203**]. This equation may also be determined from (2.4) by recognizing that $\lambda_e \propto 1/N$. Rewriting (2.12) in terms of reduced ionization and attachment coefficients

$$\frac{\alpha}{N} > \frac{\eta}{N}, \tag{2.15}$$

and when used in conjunction with (2.14), it is clear that not only does α/N have an exponential dependence on E/N, but that there exists a critical E/N for a given system below which breakdown cannot occur due to the dominating attachment processes[18].

This fact may be exploited to determine the minimum sparking voltage necessary for a given electrode spacing *d*. If the attachment coefficient is small enough to be neglected (this is the case for electronegative gases at low pressures [**200**]), then by setting the denominator of (2.5) equal to zero to find the breakdown criterion

$$1 - \gamma(e^{\alpha d} - 1) = 0,$$

(2.16)

which is approximately

$$\gamma e^{\alpha d} = 1\,,$$

(2.17)

one finds the critical distance d_s, the sparking distance,

$$d_s = \frac{1}{\alpha}\ln\left(1 + \frac{1}{\gamma}\right).$$

(2.18)

Substituting (2.18) into (2.14), the minimum sparking voltage as a function of *N*, neutral gas density, and *d*, electrode gap, is derived.

$$V_s = \frac{G\ N\ d}{\ln\left(\frac{F\ N\ d}{\ln\left(1 + {}^{1}/_{\gamma}\right)}\right)}$$

(2.19)

The above equation represents the breakdown scaling relation known as Paschen's law. Figure 2.6 illustrates Paschen breakdown curves for various gases and Table 2.1 is a compilation of minimum breakdown voltages and the corresponding *Nd* product for various gases.

[18] The following derivations assume a uniform electric field.

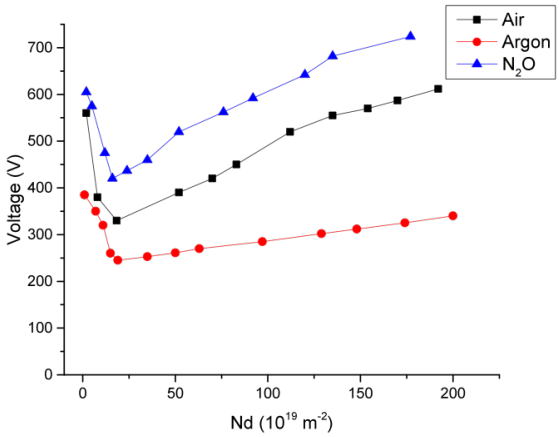

Figure 2.6: Paschen breakdown curves for air, argon, and nitrous oxide. From [200].

It should be noted that due to historical usage, Paschen breakdown data is typically reported in terms of a pressure and electrode gap distance (*pd*) product as opposed to the *Nd* product.

As the Paschen's law depends on γ, which is material dependent, the shape of the breakdown curve will depend on the electrodes used. In addition, the shape of the electrode will dictate the electric field produced, which also affects the breakdown curve shape. At high *Nd* or *pd*,

Table 2.1: Paschen minimum voltages and corresponding Nd_{min}. From [200].

Gas	$V_{S,min}$ (V)	Nd_{min} (10^{19} m^{-2})	Gas	$V_{S,min}$ (V)	Nd_{min} (10^{19} m^{-2})
N_2	270	22.0	He	161	21.0
Air	330	18.3	CO_2	418	16.4
O_2	435	22.5	Ar	245	19.0
H_2	275	37.0	N_2O	420	16.1

breakdown curves of various gases using different electrode shapes tend to match, while at electrode shape tends to have a noticeable effect at low *Nd* or *pd* values (i.e., to the left of the Paschen minimum of the curve) [**204**].

2.1.1.3 Breakdown in Practice: Theoretical Predictions versus Experimental Observations

Townsend discharge theory predicts initiation time lags between the application of voltage and the actual inception of the discharge, on the order of roughly microseconds for a 1 cm gap [**205**]. This time lag originates from the transit time of ions moving across the electrode gap and producing secondary electron emission [**195**]. However, the time lags observed in experiment

were far shorter, on the order of 10^{-8}-10^{-7} for a 1 cm gap [**206**]. In addition, atmospheric discharges were observed to be somewhat independent of electrode material [**207**]. Finally, the structure of discharges was noted to completely change from diffuse plasmas produced at lower pressure to the branching, filamentary structure of a high pressure spark (e.g., [**208**,**209**]).

To explain these various phenomena, the streamer theory of breakdown was proposed independently in 1940 by Loeb and Meek [**210**] and Raether [**211**].

2.1.2 Sparks and Streamer Theory

Strict definitions of what constitutes the Townsend regime or in which parameters the streamer mechanisms dominate do not exist, and are somewhat debated. Generally speaking, Townsend discharge mechanics apply for systems at gas pressures of 0.01-300 Torr and *pd* values of 1000 Torr-cm and lower; greater pressures and *pd* values typically operate under streamer theory [**206**,**212**]. Fridman et al. [**195**] use a pseudo-Townsend regime that extends the discharge theory much broader, applying it to atmospheric systems with the cutoff point of around $pd < 4000$ Torr-cm, which corresponds to $d < 5$ cm at $p = 760$ Torr. Beyond these values, sparks are formed and the streamer discharge theory applies.

Regardless of definition metrics, streamer discharge mechanisms are fundamentally different from the Townsend regime in a few important characteristics, as discussed in the previous section. Unlike Townsend discharges, streamers do not rely on electrode processes [**207**] as they develop on time scales far faster than ion transit time. Instead, the streamer is "fed" through photoionization and field driven ionization (discussion follows).

2.1.2.1 The Meek Criterion

The streamer begins as an avalanche, with electron multiplication being the same as described in the previous section, with n_0 electrons creating $n_0 e^{\alpha x}$ additional electrons over a distance x (2.2). The avalanche transitions into a streamer when it becomes self-propagating; that is, when the electric field at the avalanche head is roughly equal to the applied electric field.

Ionization by the avalanche results in space charge accumulation. Space charge separation occurs as the charge carriers drift in their respective directions (i.e., negative species, such as electrons, drift toward the anode, and positive species drift toward the cathode), and intensified

due to the differences in electron and ion mobilities[19]. This space charge separation creates a space charge field, E_{sc}. For cathode-directed discharges, or positive streamers, seed electrons downstream of the streamer are produced by photoionization derived from the streamer head. In anode-directed discharges, or negative streamers, seed electrons are extracted from the neutral media (refer to Figure 2.8).This local electric field, which can reach values of several hundred kV/cm, drives the ionization processes necessary for the streamer to propagate [**213**]. As with Townsend avalanches, ionization in the streamer head region must also exceed loss mechanisms such as attachment. The electric field produced by the space charge at the very beginning of the streamer development (E_{sc0}) may be estimated as a sphere of positive ions of radius r at the head of the avalanche [**210**].

$$E_{sc0} = \frac{4}{3}\pi r N e \tag{2.20}$$

In (2.20), e is the charge of an electron, N is the number of ions per cubic centimeter, given as [**206**]

$$N = \frac{\alpha e^{\alpha x}}{\pi r^2} \tag{2.21}$$

and r, in both (2.20) and (2.21), is the radius of the avalanche. Raether gives the avalanche radius as a diffusion function, in terms of D_{aval}, the diffusion coefficient of the avalanche propagation, x, the distance the avalanche has traveled at velocity v [**211**]:

$$r^2 = \frac{2D_{aval}x}{v} \tag{2.22}$$

After a distance x_s, the distance required to form a streamer, the sphere of space charge grows such that the self-produced electric field equals the applied electric field, and a streamer is created [**214**].

[19] Mobility is given as $\mu_j = \frac{|q_j|}{m_j \nu_j} = \frac{|q_j| D_j}{kT_j} \left[\frac{m^2}{V\,s}\right]$, where j = species. Typically $\mu_i << \mu_e$.

$$E_{sc} = E_0 = \frac{e}{4\pi\epsilon_0 r^2} * \exp\left(\alpha\left(\frac{E_0}{N}\right)x_s\right)$$

(2.23)

In general, (2.23) is satisfied when

$$\exp(\alpha x) \approx 10^8 \qquad \text{or} \qquad \alpha x \sim 20$$

(2.24)

which is also known as the "Meek criterion". For breakdown in electronegative gases, it is more accurate to write the criterion with the apparent ionization coefficient to account for losses due to attachment.

$$\lambda(x) = \alpha(x) - \eta(x)$$

(2.25)

(2.24) then becomes

$$\lambda x \sim 20$$

(2.26)

In integral form, the criterion (also referred to as ionization product [**72**]) is given as

$$M = \int_l (\alpha - \eta)\mathrm{dx} = \int_l \lambda(\mathrm{x})\mathrm{dx}$$

(2.27)

where l is the path of integration. Once again, $M \sim 20$ for streamer formation.

2.1.2.2 Streamer Propagation

Streamer initiation and propagation are affected by system geometry, most strongly by electrode tip shape and positioning [**215**]. For example, Yi and Williams [**216**] noted initiation delays of 30-60 ns using an electrode with tip radius of 100 μm protruding only 10 mm from the experimental set up, whereas Nijdam et al. [**217**] did not observe any initiation delays (< a few nanoseconds), with an electrode radius tip of 15 μm and mounted using a standoff holder that separated the electrode from the bulk of the experimental set up surroundings. Ceccato [**218**] measured delays as long as 538 μs from a positive streamer developing from a tip with radius of 1.5 mm.

Structurally, positive (or cathode-directed) streamers are typically more filamentary as the electrons they receive are accelerated from further away, while negative (or anode-directed) streamers tend to be more diffuse or "bush"-like [**218**]. In addition, negative streamers tend to have less field enhancement (see Figure 2.7), which require larger fields to create them, making them more difficult to produce [**217**,**219**]. In positive streamers, the electron drift velocity due to the streamer head electric field can be as high as 10^8 cm/sec [**220**], whereas streamer velocities in negative streamers are much slower, approximately 10^4 to 10^5 cm/s [**218**]. Secondary structures propagate approximately ten times faster than the primary structure [**218**].

Propagation of negative streamers is schematically depicted in Figure 2.8, where the electron drift is naturally aligned with the electric field (additional propagation methods possible). Positive streamer propagation, on the other hand, is in the direction opposite the electron drift direction and therefore relies on the creation of electrons ahead of the streamer head. In general, photoionization is considered the dominant source of the new electrons [**217**,**221**].

2.1.2.3 Photoionization

In air discharges (the primary discharge type investigated in this dissertation), the prominent photoionization mechanism is believed to be to a two-step process with nitrogen and oxygen. A two-step process, an excited nitrogen molecule with energies greater than the ionization potential of oxygen will emit a photon in the 98 nm to 102.5 nm range (2.28). This photon ionizes an oxygen molecule, producing an electron ((2.29) [**78**].

$$N_2^* \rightarrow N_2 + \gamma_{98-102.5\ \mathrm{nm}} \quad \textbf{(2.28)}$$

$$O_2 + \gamma_{98-102.5\ \mathrm{nm}} \rightarrow O_2^+ + e^- \quad \textbf{(2.29)}$$

This pathway has been called into question by some researchers (e.g., Nijdam et al. [**217**]), who observe no oxygen fractional dependence on N_2/O_2 mixtures and reported no change in

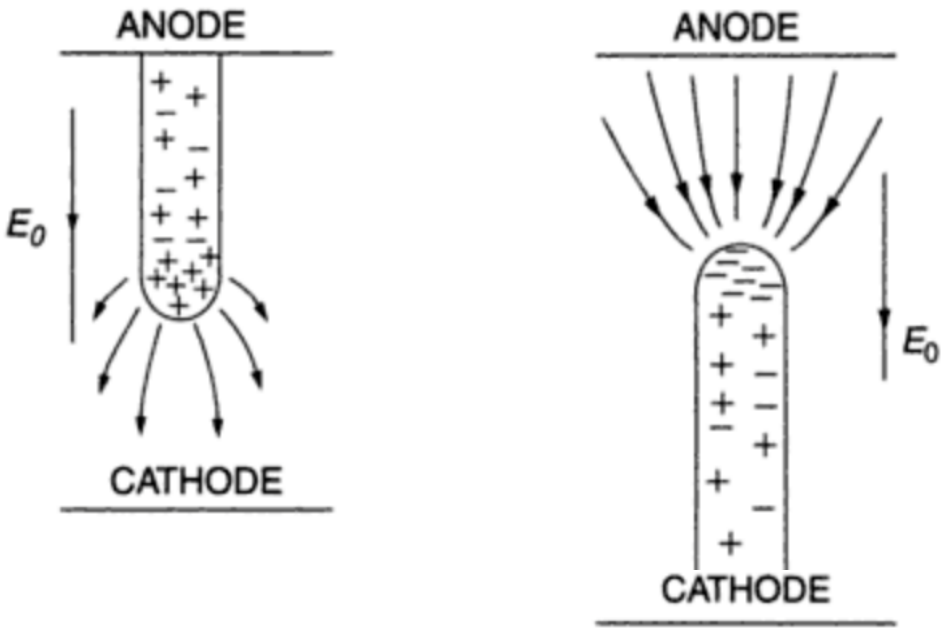

Figure 2.7: Electric field at streamer head. Left, positive streamer; stronger field enhancement typically results in more filamentary structures. Right, negative streamer; weaker field enhancement than positive streamers tend to produce more diffuse, bush-like structures. Figure adapted from Fridman and Kennedy [220].

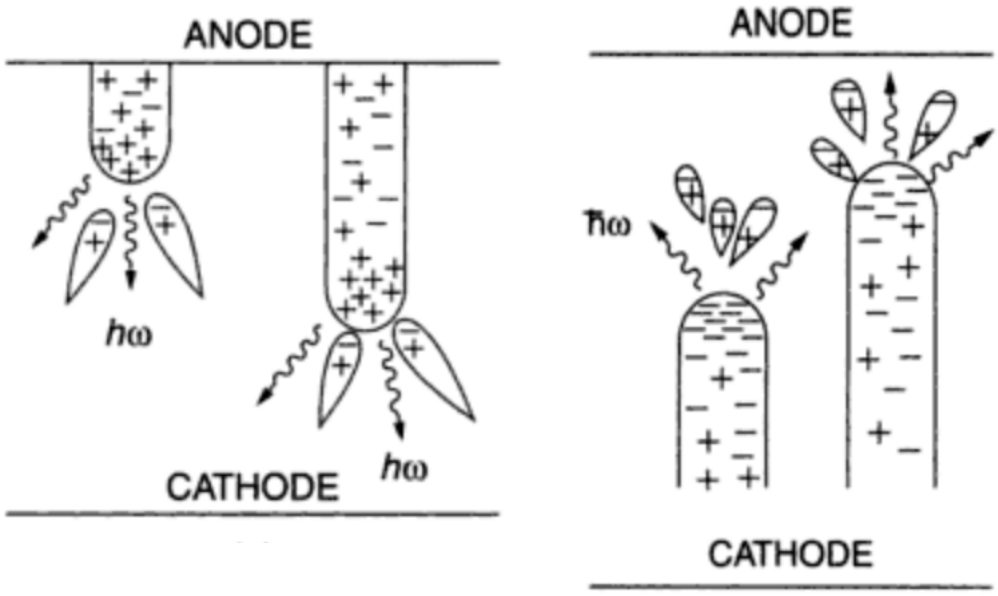

Figure 2.8: Streamer propagation. Left, positive streamer: electrons are extracted from the media via photoionization. Right, negative streamer: electrons impact onto media. Figure adapted from [220].

ionization rate, counter to the expected result if photoionization of oxygen is responsible for electron production. This is in contrast to previous groups reporting oxygen dependencies (e.g.,

[**216**]). Nijdam et al. suggest that while the direct photoionization as described in (2.28) and (2.29) may not be the primary ionization source in air streamers. Other proposed electron production mechanisms include: (1), other photoionization pathways (instead of $N_2 \rightarrow O_2$), such as step-wise ionization of N_2; and (2), background ionization, due to cosmic radiation, background radioactivity, or remaining charge from previous shots. However, numerical simulations [**222**] suggest changing the background radiation from 10^5 to 10^7 cm^{-3} only changed streamer dimensions and discharge characteristics by some tens of percent.

2.2 Plasma Ignition in Liquids[20]

Though much progress has been made over the years, plasma ignition in liquid water remains poorly understood [**223**,**224**,**225**,**73**,**69**,**226**]. Numerous aspects of breakdown in liquid water have proven difficult to discern but also have revealed a complicated system of interwoven multiphase phenomena. Vapor bubbles, dissolved gas, aqueous ions, electrode processes, polarization effects and even the electronic structure of interconnected, hydrogen bonded water molecules all contribute to physical breakdown [**110**].

Breakdown of liquid water involves electronic injection and electron mobility (solvated and perhaps free), avalanche phenomena, thermodynamic processes that can generate vapor and shocks, and fluid motion, which is driven by the dielectric liquid's elastic response to charging or polarization in the presence of a strong electric field. Additionally, the high dielectric constant of water gives rise to strong shielding and thus field localization and intensification at the liquid/metal or gas boundary. High electric fields (i.e., fields of 10 MV/cm and greater, which is on the order of the breakdown strength of water) can produce strong inhomogeneities within liquid water. Water molecules closest to the electrode (i.e., several molecular diameters from the electrode surface) can have twice the density than the bulk liquid [**227**]. This strong density gradient can affect the refractive index [**228**], which has been observed in multiple experiments (e.g., [**116**,**229**]). All of these processes are also affected by the local water electrical conductivity.

[20] Some content from this section appears in some form from a manuscript submitted by Foster, Gucker, Sommers, and Garcia to the *Journal of Physics D: Applied Physics*. Submitted February 2015, currently under review. [**110**]

2.2.1 The Physics of Water

Liquid water has a large dielectric constant – $\varepsilon_w = 80.1$ at 293.2 K. This large value is an order of magnitude greater than molecules with a comparable dipole moment[21] [**230**]. The high dielectric constant of water is due to the hydrogen bonding of the molecule, which in turn has strong polarization dynamics when subjected to an external electric field. Water molecules are strongly coupled through this hydrogen bonding [**231**] and will form complexes or groups to stabilize the collective whole [**232**]. This coupling phenomenon causes water to be categorizes as an "associated fluid" in the literature.

The electric field in the water is reduced by the factor of the dielectric constant, ε_w:

$$E_{water} = \frac{E_o}{\varepsilon_w} \tag{2.30}$$

This makes water an exceptional insulator for short pulselengths and is used extensively for insulation and switching in ultra-high voltage applications (e.g., the Sandia Z machine [**233**], CERN [**234**]).

As water is a highly polar fluid, electrohydraulic effects can come into play and even dominate hydrostatic pressure effects if the applied electric field is strong enough. Strong electrohydraulic forces will deform the liquid, which then alters the field. This deformation through field effects is known as electrostriction. The electrostriction force, F_v, on a dielectric medium, ε, for an applied field, E, is given as [**235**]

$$F_v = \frac{\varepsilon_o\left(\varepsilon/\varepsilon_o + 2\right)\left(\varepsilon/\varepsilon_o - 1\right)}{6} \cdot \nabla E^2 \tag{2.31}$$

and the field-associated pressure (or stress), P_v, is given as [**235**]

$$P_v = \frac{\varepsilon_o\left(\varepsilon/\varepsilon_o + 2\right)\left(\varepsilon/\varepsilon_o - 1\right)}{6} \cdot E^2 \,. \tag{2.32}$$

In the previous equations, ε_0 is the permittivity of free space (8.854×10^{-12} F m^{-1}).

[21] Water has a dipole moment of 1.84 and a dielectric constant of approximately 80. As a counterexample, isopropanol has a dipole moment of 1.66 and a dielectric constant of 19.9, and ethyl acetate, 1.78 and 6.02, respectively [**240**].

2.2.1.1 The Solvated Electron

An electron injected into water rapidly thermalizes ultimately becoming "solvated." Solvation is the process by which an electron is captured in a potential well formed by clusters of water molecules. This is a fast process, on picosecond timescales [**69**]. This is reflected in the strong electron stopping power of water (for a 10 keV electron, the stopping power is 22.6 MeV $cm^2\ g^{-1}$ which results in an electron penetration depth of only 2.5 microns) [**236**]. Here, the solvated electron resides essentially in a "cage" formed by hydrogen bonded water molecules [**237**]. The theoretical binding energy of this "cage" ranges between 1.5 and 4 eV [**238**].

Once the electron is solvated, it participates in radical and charged species production, which can contribute to Ohmic dissipation of heat through ion drag from time varying electric fields, which can result in vapor production, a mechanism that facilitates breakdown.

2.2.2 Breakdown Mechanisms: Competing Theories

The theories behind electrical breakdown in liquid water may be summed into two categories: bubble-facilitated and bubble-free ignition. The former [set of theories] relies upon the production of a low-density state in order for the breakdown process to develop. The latter is based on electrostriction effects, creating nanopores in which the avalanche develops. Ionization of the water itself occurs with bubble-free ignition. Both sets of theories are outlined.

2.2.2.1 Bubble and Bubble-like Breakdown

The streamer breakdown mechanism as discussed in the previous section propagates in gaseous medium. For breakdown in liquid water, this presumably takes place in gas bubbles or other low density regions within the liquid. As bubbles represent discrete, spatially localized volumes dispersed in the liquid, the following questions naturally arises: how can the discharge propagate via the streamer mechanism, producing long filamentary discharges in liquid water if the propagation medium is discrete and dispersed? Two interrelated mechanisms have been proposed: (1) localized, continuous bubble production; and (2), streamer hopping.

Bubble production suggests the streamer head itself generates a low density medium ahead of itself through which it propagates. The formed bubbles are then ignited by the oncoming streamer. Streamer hopping, proposed by Babaeva and Kushner [**114**], is the process of a

streamer inducing avalanche formation in adjacent bubbles, resulting in the discharge propagating via discrete hops between bubbles. The daughter avalanches are created due to the intense electric field at the streamer head coupled with the copious streamer-produced UV photons. Computational modeling supports this mechanism [**114**]. Experimentally, liquid streamers (i.e., streamers propagating in water) have been shown to interact with target bubbles [**116**], leading to plasma ignition, and possible experimental evidence of streamer hopping was observed and is discussed in this thesis work (see Chapter 4).

Various methods of producing bubbles in liquid water, which allow for the formation of the streamer discharge, are described in the following subsections.

2.2.2.1.1 Thermal Breakdown Mechanisms

Breakdown in the vapor state at high pressure starts with a Townsend avalanche leading to constriction due to limited radial diffusion, ending in the formation and propagation of a short lived streamer [**206**,**239**]. Considerable sources of vapor production include liquid phase Ohmic heating via ion drag; the effect of electrode surface roughness, which is locally heated and in turn locally heats the surrounding liquid; and electrolysis. A discussion on the latter two vapor producing follows.

2.2.2.1.1.1 Field-enhanced auto-ionization of water

The amphoteric[22] nature of water implies autoionization:

$$H_2O\ (l) \rightleftharpoons\ H^+(aq) + OH^-(aq) \quad \textbf{(2.33)}$$

As free protons do not exist in water, (2.33) may also be written as

$$2H_2O\ (l) \rightleftharpoons\ H_3O^+(aq) + OH^-(aq). \quad \textbf{(2.34)}$$

At 25 °C, the water dissociation constant, K_w, is 1.01 x 10^{-14} where $K_w = [H_3O^+][OH^-]$ [**240**]. The source of autoionization in water is due to fluctuations in the polarization electric field brought on by the re-arrangement of the polar water molecules in solution [**241**]. Similarly,

[22] i.e., the ability for a substance to act as an acid or as a base in chemical reactions. The most common example of an amphoteric substance is water, other solutions HCO_3^- (hydrogen carbonate ion or bicarbonate ion).

strong, localized fields near the electrode can also drive field ionization; molecular dynamics simulations predict threshold fields to drive the disassociation of water are approximately 35 MV/cm [**242**]. In this respect, field disassociation can increase the fraction of ions in solution even in deionized water. This increase in ion concentration locally increases solution conductivity. Localized Ohmic heating near the electrode is therefore possible via field driven ion drag collisional conduction, producing vapor—a potential precursor medium for breakdown [**243**]. Indeed, this is surmised as the basis for vapor formation in saline solutions leading eventually to breakdown [**244**]. In this respect, the field ionization property of liquid water cannot be discounted as a contributing mechanism toward breakdown.

2.2.2.1.1.2 Electrolysis

Electrolysis takes place at the electrodes where water is reduced at the cathode and oxidized at the anode. This process gives rise to the formation of hydrogen bubbles at the cathode and oxygen bubbles at the anode [**245**]. Ordinarily this reaction proceeds slowly in pure water owing to its low conductivity (~10^{-6} S/m for deionized water). However, dissolution of ions from electrodes, impurities in the water or the localized aforementioned field disassociation of water allows this process to proceed at an increased rate. The susceptibility of water molecules to decomposition via electrolysis means that this process will always be present at some level, generating vapor [**246**]. This vapor can serve as a low-density medium for breakdown [**110**].

2.2.2.1.2 Crack Theory

Another discharge mechanism theory put forth by Lewis [**247**] suggests ponderomotive-driven mechanical stress on the liquid water creates cracks or fissures within the liquid media, thereby producing a low-density region for discharge to form. Analogous to the fissure formation in solids under stress, the electric fields necessary to produce such a phenomenon are on the order of 5 MV/cm or greater[23].

The properties of cracks, namely the characteristic length scale (10^{-7} m) and electric field (10^{8} V/m), have the potential to accelerate electrons to near the ionization potential (~10 eV). In this theory, the short time scales of streamers are related to fluctuation in void population formed

[23] Using the theoretical tensile strength of water as 10^{8} Pa [**436**]

under electric field-driven stress. In this case, ignition is accomplished via fissure formation followed by streamer inception. Anode and cathode-directed streamers can be explained at least qualitatively with the crack model. Very high-resolution optical diagnostics are required to test this potential breakdown mechanism.

2.2.2.1.3 Bubble Mechanisms

While the thermal mechanisms discussed previously have considerable experimental evidence, other bubble formation theories exist. In addition, as localized heating due to the application of voltage pulses with pulse widths of microseconds and shorter is not sufficient to yield the heating required to vaporize the surrounding water [**248**], other discharge mechanisms are necessary.

In its natural state, water contains dissolved gases. It has been postulated that micron-sized bubbles can stably exist in liquid water [**249**], and it has been demonstrated that the presence of long-lived microbubbles reduces time to breakdown in liquid water [**250**]. Monte Carlo simulations carried out by Joshi and colleagues suggest that breakdown in microbubbles is the most compelling mechanism leading to discharge ignition in liquid water [**251**].

Qian and colleagues further assert that it is field emission at the electrode or at the bubble-liquid interface that gives rise to nascent electrons that drive the avalanche process in the liquid bubbles [**224**]. In the case of the bubble-liquid interface, the field is also greatly enhanced. In fact, at such high field strengths, the dielectric constant locally is reduced just as in the case of the electrode-liquid interface, thereby further enhancing the local electric field leading to the field emission. In this case, the postulated microbubbles themselves are therefore the source of electrons and localized breakdown. Liquid streamer branching, current spikes, and pressure effects appear to be consistent with this theory.

2.2.2.2 Bubble-free Breakdown

The development of a discharge in the liquid water via electron avalanche has been largely dismissed due to the high collisionality and the extremely short solvation time of an injected electron. Recently however, the prospect of bubble-free ionization in the liquid state has been proposed [**252**,**253**]. This mechanism requires high voltage, sub-nanosecond pulses. With such a

short pulse, it is possible to form local to the electrode, a region monodispersed with nanopores or ruptures in the liquid water via electrostriction (2.31). The liquid water is rapidly drawn to the electrode surface, which gives rise to locally higher liquid density as discussed previously. This stress on the medium causes tearing of the liquid itself and creates voids within the volume, downstream of the electrode.

If the local field is high enough, the Meek condition can be satisfied in the nanopore and breakdown may form directly within these void regions, or within bubbles caused by secondary effects due to these void regions. Bubbles may form from the cavitation forces due to the sudden density gradients produced in response to the voltage pulse from the electrode, or due to pressure difference between the ambient and reduced pressure regions [**110**]. Electrons in the nanopore can be accelerated to energies necessary to ionize water at the interface and drive an avalanche between nanopores. This mechanisms requires the pulse rise time on the electrode be shorter than the pressure equilibration time—which determines the lifetime of the pores. Experimental evidence suggests that this mechanism is possible [**254**]. Meek's criterion for liquid (given in (2.24)) becomes:

$$e^{\alpha x} \cdot e^{\mu x} \geq N_{e\,min}, \qquad \text{or} \quad (\alpha + \beta)x \geq 20 \tag{2.35}$$

In (2.35), α is the ionization coefficient from traditional streamer theory, β is the electron multiplication inside the low density region of the nanopore, x is the distance traveled by the streamer, and $N_{e\,min} \sim 2\times10^{8}$ electrons [**254**].

In some respects, the distribution of nanopores is likened to the cracks and voids formed under electrostriction forces describe in the Lewis theory. The theories differ in that liquid phase ionization is important in the nanopore theory whereas in the crack theory, the streamer is essentially confined to the field-induced fissure.

2.3 Essential Plasma Chemistry

2.3.1 Species Creation & Decomposition Theory

2.3.1.1 Plasma Electrons

Plasma electrons are the primary drivers of chemistry, and collisions are some of the most important mechanisms within the system. A summary of electron collisions may be found in the previous section in Table 2.2. Electron energy transfer efficiency is important in driving these

Table 2.2: Electron collisions in plasmas [255].

Collision Type	Comments
Elastic/Momentum Transfer	$\Delta\varepsilon \approx 2m/M$
Rotational Excitation	Usually small energy loss
Vibrational Excitation	Large cross sections; $\Delta\varepsilon = 0.1\text{-}0.25$ eV
Electronic Excitation/Dissociation	Metastable excit. and dis. important
Ionization	Can dissociate
Attachment	Usually dissociative; neg. ions very important
Dissociative Recombination	Usually large *k*; important e^- loss process
Three-body Recombination	Coll. radiative recomb.; important at high P
Three-body Attachment	May be important at high pressure

reactions. The most efficient method of transferring energy to the electrons is through short pulses [**161**], which minimizes heat transfer to the heavy particles [**75**]. An example of the evolution of plasma chemistry following a short pulse may be seen in Figure 2.9, which gives the calculated densities of various species following a 10 ns-width pulse. These are the results from a global chemistry model, calculated from a 20% O_2, 80% N_2 mixture with 30 reacting species and 143 reactions [**256**]. Within the first 100 ns essentially all charged species have decayed either via diffusion, attachment or recombination. The subsequent chemical reactivity beyond this point is due to reactions driven by longer-lived species created by the discharge. These chemical reactions proceed without major electric loses. Important electron driven reactions with associated rate coefficients may be seen in Table 2.3.

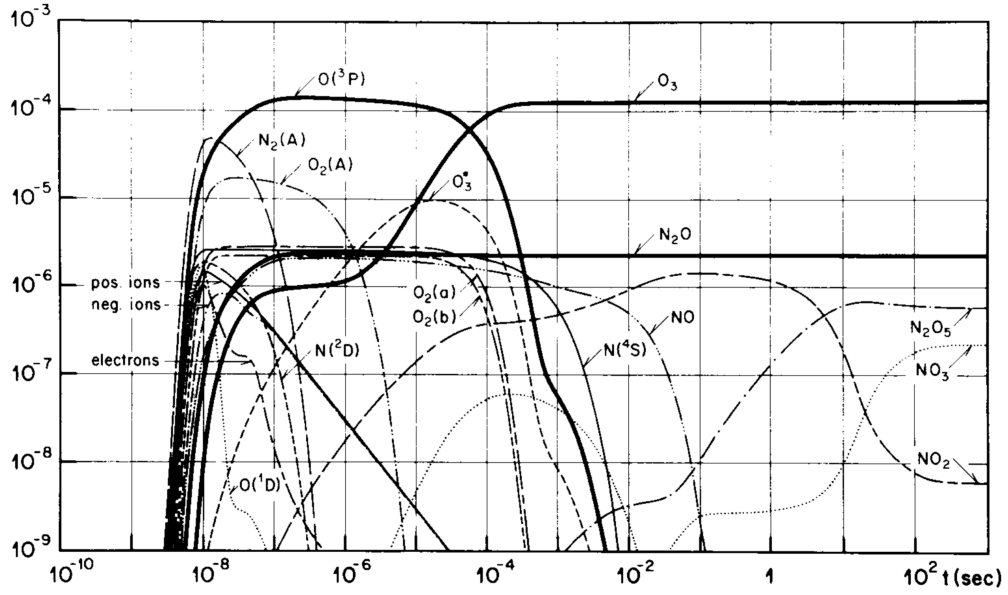

Figure 2.9: Calculated particle densities (a.u.) with time following pulse. Formation of chemical species in "air" (20% O_2, 80% N_2) due to a 10 ns-width pulse [161].

Table 2.3: Electrical discharges in air; some important electron driven reactions. $k = A \exp\left(\frac{-B}{E/N}\right)$. From [257].

Reaction	A ($cm^3\ s^{-1}$)	B (Td)
$e^- + O_2 \rightarrow O_2(a\ ^1\Delta) + e^-$	1.0×10^{-9}, $E/N \leq 40$	120, $E/N \leq 40$
	1.0×10^{-9}, $E/N > 40$	8.1, $E/N > 40$
$e^- + O_2 \rightarrow O\bullet + O\bullet + e^-$	1.3×10^{-8}	309
$e^- + O_2 \rightarrow O(^1D) + O\bullet + e^-$	1×10^{-8}	338
$e^- + N_2 \rightarrow N_2(A\ ^3S) + e^-$	1×10^{-8}	336
$e^- + N_2 \rightarrow N\bullet + N\bullet + e^-$	6.3×10^{-9}	949
$e^- + N_2 \rightarrow N_2(C\ ^3H) + e^-$	6.3×10^{-9}	486
$e^- + H_2O \rightarrow OH\bullet + H\bullet + e^-$	2×10^{-11}	322

2.3.1.1.1 Plasma Electrons and Sterilization

Plasma electrons are also important sterilization drivers in liquids containing biomass (e.g., microbe-rich water). Fridman [**74**] gives the characteristic depth of sterilization in bio-organisms from plasma electrons as

$$x^2 = x_0^2(\ln(\sigma_{io} N) - \ln(\ln(K))),$$

(2.36)

where σ_{io} is the electron-impact biodeactivation cross section (approximately 10^{-9} cm^2 [**258**]), N is total electron flux to the surface, and K (>> 1) is the degree of destruction. For plasma densities of around 10^{13} cm^{-3}, the electron penetration depth is around 6 μm. Charged particles are believed to play a dominant role in the deactivation of microorganisms [**259**]. Effective treatment of water contaminated by microorganisms is an important and necessary ability of plasma treatment systems; studying the boundary region between plasma and liquid and the diffusion of plasma-produced species (as in Chapter 7) is a critical area of research that should be investigated.

2.3.1.2 Ions

One of the most important type of ions in plasma-water systems are water cluster ions, as the non-resonant charge exchange reactions result in much of the ionization energy of the system becoming focused on the creation of water ions [**74**]. Prominent clusters of $M(H_2O)_n$ include $M = O_2^-, CO_3^-, O_3^-, NO^-, NO_2^-, NO_3^-, HCO_3^-$ and $M = H_3O^+, NO^+, NO_2^+$ [**260**]. Dominant hydrated ions (even at low water concentrations, e.g., 50 ppm) are $O_2^+(H_2O)_2$ and $O_3^-(H_2O)_2$ [**261**].

2.3.1.2.1 Positive Ions in Water

In general, both positive and negative ions interact with water molecules via charge exchange, due to the relatively low ionization potential (~10 eV [**262**,**263**]) and the high dipole moment of water molecules [**74**]. As an example, in non-thermal humid air or air+water plasmas, the N_2^+ ion is one of the most prevalent cations and undergoes the following charge exchange with water molecules at relatively fast rates (k (300 K) = 2.2×10^{-9} cm^3 s^{-1}) [**74**]:

$$N_2^+ + H_2O \rightarrow N_2 + H_2O^+$$

(2.37)

The ensuing fast (k (350 K) = 0.5×10^{-9} cm^3 s^{-1} [**74**]) ion-molecular reactions between water ions and neutral water are a strong contributor to the resulting acidic nature[24] of air discharges:

[24] Species also responsible for the acidification of air plasmas include nitric (HNO_3) and carbonic (H_2CO_3) acids.

$$H_2O^+ + H_2O \rightarrow H_3O^+ + OH$$

(2.38)

(2.38) is an exothermic reaction with ΔH = -0.52 eV. The fast production of hydronium (H_3O^+) initiates and is similar to other higher water ion clusters of $H^+(H_2O)_n$ [**74**,**264**]. H_3O^+ and $H_5O_2^+$ are nearly isoenergetic and therefore can rapidly change back and forth between the two cluster formations, though H_3O^+ is the more electrically stable formation as the charge is distributed over three hydrogen atoms versus $H_5O_2^+$, which is centered on the central hydrogen proton [**265**].

Many exothermic reactions between neutrals and positive or negative ions have zero activation energy, which results in ions being significant actors in plasma chemistry and chemical processes [**266**].

2.3.1.2.2 Negative Ions in Water

Negative ion formation in water and humid air is primarily due to electron attachment to electronegative species such as oxygen and water vapor [**267**]. One important negative ion in low temperature water discharges is O_2^-, or superoxide. It is created directly from solvated plasma electrons converting aqueous O_2 into aqueous O_2^-:

$$e_{aq} + (O_2)_{aq} \rightarrow (O_2^-)_{aq}$$

(2.39)

Aqueous superoxide goes on to create additional strongly oxidizing species, such as hydrogen peroxide (2.40) and peroxynitrate (2.41) (all in solution) [**74**]:

$$(2O_2^-)_{aq} + (2H^+)_{aq} \rightarrow (H_2O_2)_{aq} + (O_2)_{aq}$$

(2.40)

$$(O_2^-)_{aq} + (NO)_{aq} \rightarrow (OONO^-)_{aq}$$

(2.41)

Hydroxide (OH^-), the anion of the hydroxyl radical, has two stable isomers in water, $OH^-(H_2O)$ and $OH^-(H_2O)_3$, of which the latter is more stable due to direct solvation by three water molecules [**265**].

2.3.1.3 Radicals and Excited Species

Species produced in these plasmas is gas dependent. Many plasma systems used for treating contaminants in water use air [**268**,**269**,**270**] or oxygen [**271**,**111**,**272**]. Argon tends to be the third most commonly used gas [**271**,**273**], but other gases have been investigated, such as helium [**274**] and nitrogen [**275**]. Chapter 6 in this dissertation details the development and study of a discharge that uses the liquid water itself as the ionizing medium (i.e., water vapor) [**77**].

2.3.1.3.1 Ozone

As previously mentioned, plasma-based water purification is attractive in that mixtures of different reactive species are produced. Neutral species production can be significant in atmospheric air plasmas, and are large sources of strong oxidizers, both short-lived (such as OH, O, $O_2(^1\Delta_g)$, etc., less than a second[25]) and long-lived (ozone, NO, NO_2, etc., which can last in water up to half an hour, depending on the water chemistry [**276**]). Ozone in electrical discharges is an endothermic reaction ($\Delta H \approx 1.5$ eV/mol) and believed to be created via the following two-step process [**78**,**277**,**278**]:

$$O_2 + e \rightarrow O^+ + O + 2e \quad \textbf{(2.42)}$$

$$O_2 + e \rightarrow O + O + e \quad \textbf{(2.43)}$$

$$O_2 + e \rightarrow O^- + O \quad \textbf{(2.44)}$$

Diatomic oxygen is converted via plasma electrons into atomic ions ($O^{+/-}$) and the oxygen radical O. Free oxygen radicals then undergo three-body reactions to create ozone (in air plasmas, M = N_2 or O_2).

$$O + O_2 + M \rightarrow O_3 + M \quad \textbf{(2.45)}$$

Comparison between the disinfection rates of Giardia cysts by ozone and other disinfectants is given in Table 2.4, in which values of *Ct* (concentration times time, given in units of mg min/L)

[25] E.g., at room temperature and atmospheric pressures, OH radicals can recombine as quickly as 50 μs [**411**].

necessary for each disinfectant to produce the various inactivation levels are given, demonstrating the power of ozone as a disinfectant.

Table 2.4: Inactivation of Giardia cysts by various disinfectants. From [276].

Disinfectant	**Inactivation (mg min/L)**			
	0.5-log	*1-log*	*2-log*	*3-log*
Chlorine	17	35	69	104
Chloramine	310	615	1230	1850
Chlorine Dioxide	4	7.7	15	23
Ozone	0.23	0.48	0.95	1.43

2.3.1.3.2 Hydroxyl Radical

Ozone, while an excellent species for deactivating and decomposing microorganisms (as in Table 2.4) [**279**], is fairly ineffective against numerous organic compounds (as in Table 2.5). In these cases, the hydroxyl radical is a far more effective choice (oxidation potential of OH, 2.80 V; O_3, 2.07 V; from Table 1.1), with typical reaction rates of eight orders of magnitude greater than those of ozone. Hydroxyl radicals are a prominent source of reactivity in organic systems treated with plasmas. OH is able react with contaminants and enter cells very quickly (at the speed of its very fast diffusion rate [**74**]) and attach to any electron-heavy organic compound through its available free radical site. For example, with fatty acid R, once the initial reaction, $OH\cdot + R \rightarrow ROH$, is initiated, the product goes onto many different reaction chains, creating superoxide, H^+, peroxyl radical (R-OO-), and more caustic species. Existing atomic oxygen (e.g.,

Table 2.5: Reaction rates of ozone and the hydroxyl radical with various organic compounds in water. Adapted from [280,281,282].

Compound	**Reaction Rate ($cm^3\ s^{-1}$)**	
	O_3	**OH**
Acetic Acid	1.66×10^{-26}	1.66×10^{-14}
Benzene	3.32×10^{-21}	1.30×10^{-11}
Toluene	2.32×10^{-20}	1.30×10^{-11}
Chlorobenzene	1.25×10^{-21}	6.64×10^{-12}
Trichloroethylene	2.82×10^{-20}	6.64×10^{-12}
Tetrachloroethylene	1.66×10^{-22}	2.82×10^{-12}
n-Butanol	9.96×10^{-22}	7.64×10^{-12}
t-Butanol	4.98×10^{-23}	6.64×10^{-13}

Table 2.6: Radical formation in water. Adapted from [257].

Reaction	k (cm^{-3} s^{-1})
$H_2O \rightarrow OH\bullet + H\bullet$	5.57×10^{11}
$H_2O \rightarrow ½H_2O_2 + ½H_2$	7.23×10^{14}
$2H_2O \rightarrow H_3O^+ + e^-_{aq} + OH\bullet$	1.42×10^{12}
Reaction	**k (cm^3 s^{-1})**
$H\bullet + O_2 \rightarrow HO_2\bullet$	1.66×10^{-11}
$H\bullet + H_2O_2 \rightarrow H_2O + OH\bullet$	1.66×10^{-11}
$OH\bullet + H_2O_2 \rightarrow H_2O + HO_2\bullet$	8.3×10^{-14}
$e^-_{aq} + OH\bullet \rightarrow OH^-$	4.98×10^{-11}
$e^-_{aq} + H\bullet + H_2O \rightarrow OH^- + H_2$	4.15×10^{-11}
$e^-_{aq} + H_2O_2 \rightarrow OH\bullet + OH^-$	1.99×10^{-11}
$OH\bullet + H\bullet \rightarrow H_2O$	4.02×10^{-12}
$2OH\bullet \rightarrow H_2O_2$	6.64×10^{-12}
$2HO_2\bullet \rightarrow H_2O_2 + O_2$	3.32×10^{-15}
$H\bullet + HO_2\bullet \rightarrow H_2O_2$	1.66×10^{-11}
$2H\bullet \rightarrow H_2$	1.66×10^{-11}
$HO_2\bullet + OH\bullet \rightarrow H_2O + O_2$	1.66×10^{-11}
$H_3O^+ + OH^- \rightarrow 2H_2O$	4.98×10^{-11}

created by some other plasma process) will undergo hydrogen abstraction ($O\cdot + RH \rightarrow R\cdot + OH$), which makes more hydroxyls. In short, hydroxyls can wreak havoc in biological systems due to the self-feeding chain reactions they set off [**74**,**283**]. OH reaction rates with various organic compounds in water in comparison with ozone are shown in Table 2.5.

In plasma-water systems, OH and O production tends to be most efficient for low conductivity water (≤ 100 µS/cm) [284,285**]; as wastewater, very generally speaking, is substantially more conductive (ranging from ~1 mS/cm to ~1 S/cm) [**286**], industrial or municipal application of a plasma-driven system will most likely involve additional processing. Some of the important radical formation reactions formed in a water system are given in**

Table 2.6.

Hydroxyl radicals are produced in humid gases, thus many plasma-water discharges are excellent sources of hydroxyl radicals; with the additional plasmas-created species (e.g., ozone,

UV photons), the end result is a multifaceted decomposition system that has a broad application range.

2.3.1.4 UV Photons

One of the chief energy pathways of discharges in water is in the creation of UV [**287**]. UV radiation has long been known as a sterilizer against microorganisms [**288**] (such as antibiotic-resistant bacteria [**289**], and has been used extensively in water discharges to deactivate microorganisms [**290**]. However, the cell walls of many microorganisms tend to be easily damaged by other plasma products, such as the highly reactive molecule ozone, but some contaminants are more recalcitrant (such as anthrax spores, which have been known to be viable after dormancy of over 70 years [**291**]).

Spores, for example, need UV radiation to penetrate their thick shells to damage DNA in order to prevent growth (most efficient deactivation, 200-300 nm) [**292**]. Excited NO molecules, as well as various N_2 and N_2^+ bands will produce photons in this range [**293**], making air plasmas a cheap and viable option for spore decontamination. In addition, the afterglow of a N_2/O_2 plasma results in significant three body recombination, producing more NO (via $N + O + N_2 \rightarrow NO(A) + N_2$) [**294**]. In the case of spores, UV alone tends to be a slow deactivation process, primarily because of the thickness of the thick organic or inorganic[26] cell walls. This merely raises the attraction of plasmas for water purification, as plasmas contribute to a variety of inactivation and sterilization products to speed the process (e.g., electron etching of the spore surface). It should be noted that the role of UV photons as an instrument of deactivation is a contested one, with some authors claiming UV photons play little to no role at all in the sterilization process [**295**], while others give evidence of deactivation with specific conditions [**296**,**297**].

Finally, UV plays an important role in the production of OH and other reactive species via photodissociation of hydrogen peroxide (see (2.46) through (2.48) [**298**]).

$$H_2O_2 + h\nu \rightarrow OH + OH, \qquad \lambda_{threshold} = 557 \text{ nm} \tag{2.46}$$

[26] Other organisms may have inorganic cell walls, such as fungi. Such inorganic walls may be comprised of materials such as Fe, Si, Cu, Cr, Al, Be, Mn, etc. [**435**], which have far lower reaction rates than the oft-thought of fatty acid chains.

$$\rightarrow H_2O + O(^1D), \qquad \lambda_{threshold} = 359\ \text{nm} \quad \textbf{(2.47)}$$

$$\rightarrow HO_2 + H \qquad \lambda_{threshold} = 324\ \text{nm} \quad \textbf{(2.48)}$$

2.3.1.5 Mineralization, the Final Fate of Contaminants

The process of plasma destruction of contaminants is known as mineralization, which refers to reducing compounds into water, carbon dioxide and inorganic ions. Using methanol as an example compound, the mineralization process of methanol could proceed as follows:

$$CH_3OH + OH \rightarrow CH_3OH \xrightarrow{OH/O_2} CH_2O \xrightarrow{OH/O_2} CHO - OH \xrightarrow{OH/O_2} CO_2 + H_2O \quad \textbf{(2.49)}\ [299]$$

Total mineralization of contaminants is the idealized end goal of all water purification technologies, as it renders even the most toxic compound harmless.

2.3.1.6 Deactivation of Microorganisms via Plasma Discharges

The essential mechanics of plasma deactivation of microorganisms are given as: (1) UV radiation, which destroys genetic material; (2), photodesorption, the chemical desorption (or chemical bond breaking resulting in volatile by-products) by UV photons; and (3), etching of the cell material [**48**,**300**,**301**]. As microorganisms have multiple components (e.g., cell wall, organelles, etc.), the deactivation of microorganisms is also a multiphase process, especially if the cell is protected by resilient cell walls (such as in spores [**302**]). Figure 2.10 illustrates a typical deactivation curve for hardy spore-producing bacteria (*B. subtilis*) and Figure 2.11 depicts the corresponding phases of deactivation. While these experiments were carried out at reduced pressure (5 Torr), the results are typical of plasma deactivation of spore-producing bacteria.

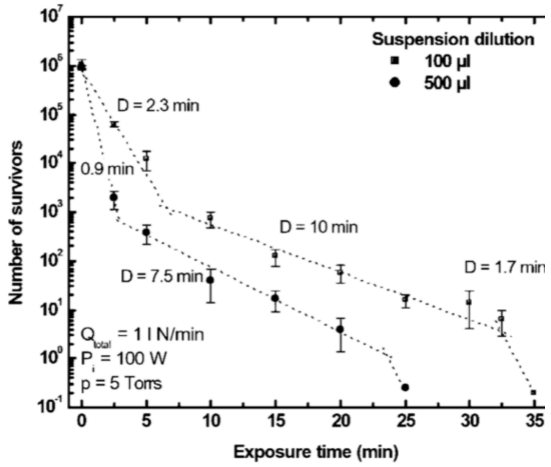

Figure 2.10: Deactivation curve of *B. subtilis* spores subjected to afterglow of a N_2/O_2 (0.7% O_2) plasma. From [48].

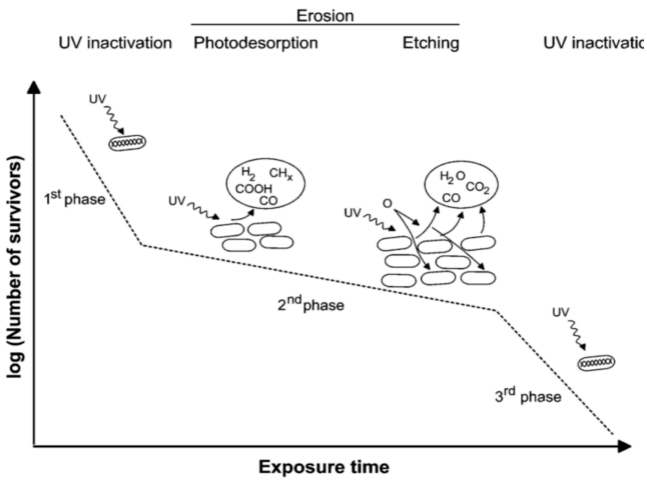

Figure 2.11: Schematic illustrating the deactivation kinetics at each phase of deactivation as described in Figure 2.10. From [48].

2.3.2 Plasma vs. Conventional AOPs

One of the most attractive characteristics of plasma-based purification technology is the synergistic quality of the discharges and resultant species each playing off another and working in concert. For example, combinations such as low pH, H_2O_2, nitrate, and nitrite in plasma treated water has been shown to have a greater effect than individual species [**140**,**303**]), as well as synergism between plasma and catalysts material [**304**]. For many circumstances and applications, plasma-based methods are more efficient and more reactive than many typical methods. A summary of typical reactions with reaction rates may be found in Table 1.1.

2.3.3 External Factors Influencing Decomposition

OH is the primary driver of decomposition. The effectiveness of OH (and other AOPs) is determined by several characteristics of the treated liquid. As OH has no selectivity between compounds, it will react with essentially any organic material dissolved in the liquid. If the chemistry of the treated liquid is unfavorable, this can lessen the impact of OH on the target contaminant [**305**]. Two examples are given below.

2.3.3.1 Alkalinity

Carbonates (CO_3^{2-}) and bicarbonates (CO_3^{2-}) (the source of alkalinity in water under natural circumstances [**306**]) can be so plentiful that they compete against toxic contaminants even if the contaminant has a higher reaction rate with OH. The rate constants for carbonate and bicarbonate reactions with OH are 3.8×10^{8} M^{-1} s^{-1} (6.31×10^{-13} cm^3 s^{-1}) and 8.5×10^{6} M^{-1} s^{-1} (1.41×10^{-14} cm^3 s^{-1}), respectively [**283**], while the reaction rate of OH with MTBE (a gasoline-additive commonly occurring in groundwater) is 10^{9} M^{-1} s^{-1} (1.66×10^{-12} cm^3 s^{-1}).

2.3.3.2 Nitrates and nitrites

Photooxidation of hydrogen peroxide is one source of OH; however, nitrates and nitrites absorb UV within the necessary energy range (e.g., 200-250 nm photons strongly drive photolysis-based conversion of nitrate to nitrite [**307**]) Thus, large quantities (>1 mg/L for both) of nitrate and nitrite will suppress OH within the liquid [**308**]. In addition, nitrites react quickly with hydrogen peroxide (removing sources of OH) [**309**].

2.4 Closing Comments

Although electrical discharges in liquid water have been studied for several decades, a multitude of questions remain. On the discharge physics side, perhaps the main question to be answered is the physical processes in water that lead to breakdown and streamer propagation in liquid water. While some characteristics and mechanisms are known [**110**], further experiments are necessary to arrive at a mature understanding of the role of liquids in discharges. On the plasma chemistry side, it is necessary to develop an understanding of the interplay between plasma electrons and produced reactive species within the discharge system, specifically to (1) develop controlling parameters, and (2), assess the role of the plasma-liquid interface. The nature of plasma production at the gas-liquid interface and a clear understanding of reactant transport throughout the bulk liquid are unknown. This thesis work contributes experimental evidence and analysis to assist both of these matters.

Chapter 3:

Experimental Methods

This dissertation is centered on three main experiments: single bubble studies, bulk plasma phenomena in large bubbles, and assessment of the interfacial region between bubble gas and treated liquid during plasma discharge. A number of diagnostics were used throughout this research and are described in this chapter. Unless otherwise noted, all experiments and diagnostics took place in the Plasma Science and Technology Laboratory at the University of Michigan.

3.1 Experimental Apparatuses

3.1.1 Single Bubble Studies

Studying a single gas bubble and small ensembles (<5) of bubbles immersed in liquid water, stressed by a high electric field enables one to observe breakdown dynamics and associated hydrodynamics associated with plasma formation. Basic experiments can be performed on a single bubble, thereby allowing one the opportunity to isolate the physics, ultimately enabling one with a fundamental understanding of breakdown physics. Single bubble studies reported in this thesis were studied in the levitation cell developed by Sommers [**72**] (refer to image in Figure 3.1 and schematic in Figure 3.2). Through the use of a piezoelectric transducer, a sound field is created in a Plexiglas cell and a three dimensional acoustic standing wave is excited in the cell which is filled with degassed deionized water. Bjerknes forces trap the bubble at the vertical node of the standing wave. Electrodes, which provide electrical grounding and excitation to ignite plasma, are arranged about the levitated bubble. The cell was designed and constructed such that the three dimensional standing wave would be sustained at 26.4 kHz, the resonant frequency of the transducer used.

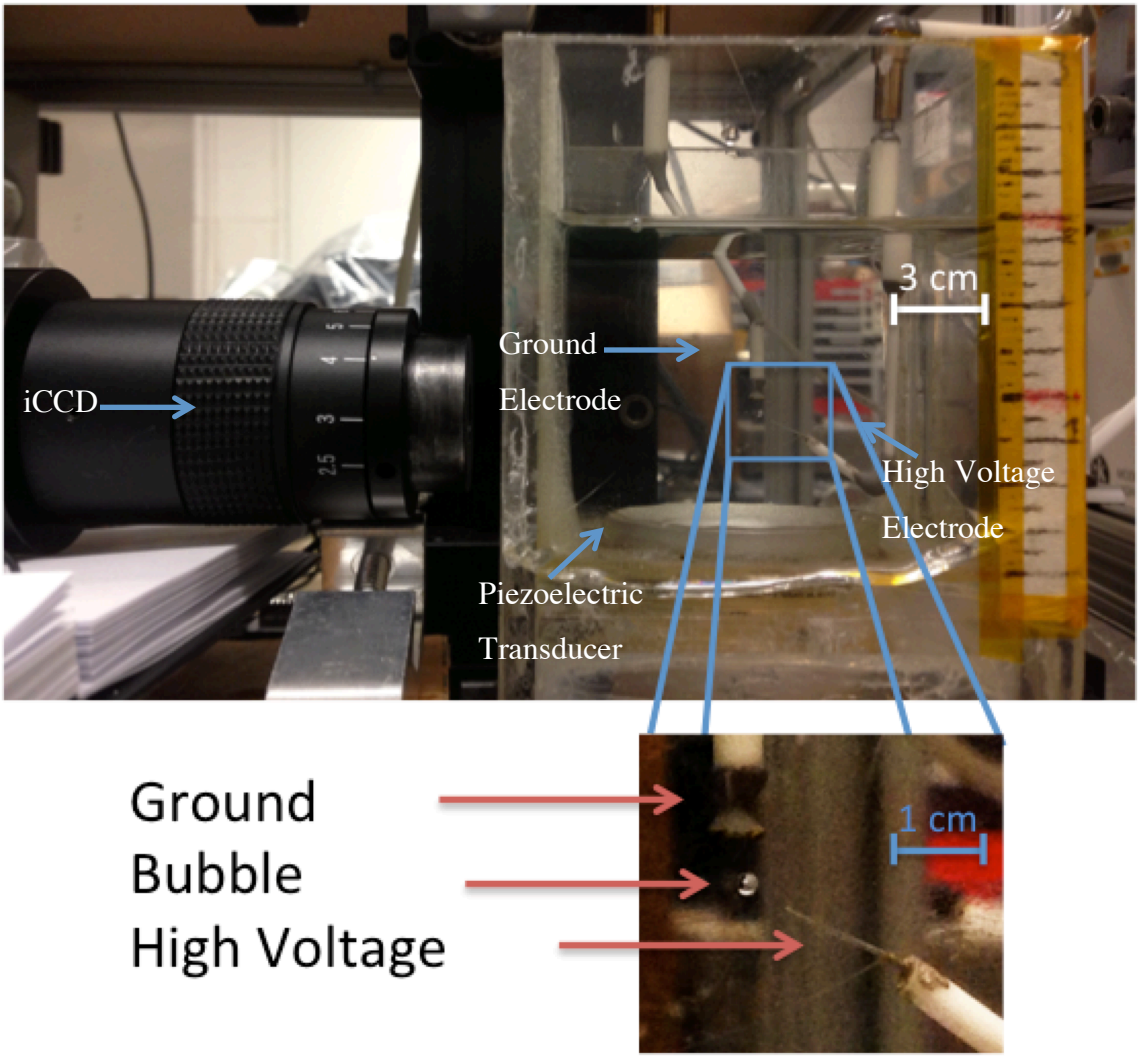

Figure 3.1: The levitation cell in use, with a single bubble levitated with electrodes (point-to-plane configuration).

3.1.1.1 Bubble Levitation

A piezoelectric transducer of resonant frequency f_s was used to induce a sound field within the cell that set up a three-dimensional standing wave within the cell. The inherent resonant frequency of the transducer (26.4 kHz) determined the dimensions of the cell. The relationship between the dimensions of the rectangular cell and the resonant frequency is given by:

$$f_s = \frac{c_s}{2}\sqrt{\left(\frac{n_x}{L_x}\right)^2 + \left(\frac{n_y}{L_y}\right)^2 + \left(\frac{n_z}{L_z}\right)^2} \quad (3.1)$$

where f_s is the frequency, c_s is the speed of sound in water, n_i is the number of half wavelengths along axis i (e.g., $n_i = 2$ is one full wavelength), and L_i is the length dimension along axis i. The cell is symmetric in $\hat{x}$ and $\hat{y}$. The standing wave excited within the cell is [1,1,2], where the standing wave is in half wavelengths along the x- and y-axes, and in a full wavelength in the z-axis (see Figure 3.2).

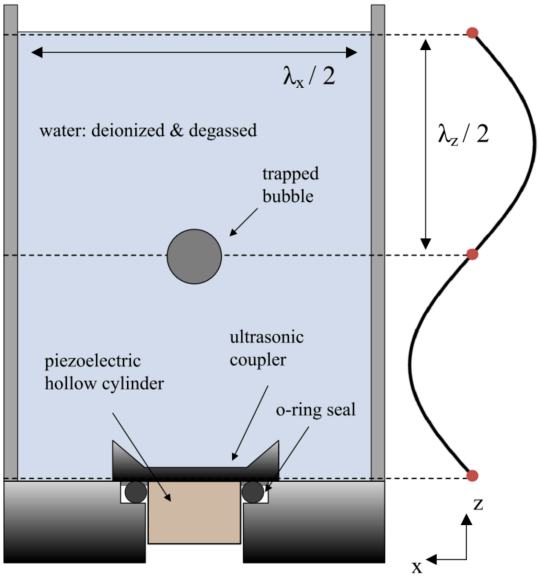

Figure 3.2: The levitation cell. From [72].

Vertically, the bubble is trapped as the Bjerknes force (F_B) exactly counters the force due to buoyancy (F_b).

$$F_B = F_b$$

(3.2)

$$F_b = \rho g V(t)$$

(3.3)

Above, ϱ is the density of the liquid, g is the acceleration due to gravity, and V is the volume of the bubble.

The Bjerknes force refers to the translational force on a bubble that arises when a bubble is within an acoustic pressure field [**310**] ((3.4).

$$F_B = \pm \frac{3P_A k \xi_0 V_0 \sin(2ky)}{2R_0}$$

(3.4) [310]

Above, P_A is the amplitude of the sinusoidal pressure sound wave, k is the wave vector, ξ_0 is the initial amplitude of radial oscillation, V_0 is the initial bubble volume, and R_0 is the initial bubble radius. The equation takes the positive sign if the bubble is smaller than resonance (pushing the bubble toward the node of the standing wave), and has a negative sign when the bubble is larger (pushing it toward the antinode).

3.1.1.2 Isolated Bubbles

Breakdown studies are carried out by positioning electrodes near the trapped bubble. In this apparatus, contact-less breakdown could be studied (electrode not in contact with the bubble). Electrode-less plasma initiation is attractive in that it can potentially eliminate electrode erosion, enabling purely capacitive coupling. For isolated bubbles, the point-to-plane electrode configuration was used. The point-to-plane configuration allows the electric field to be enhanced due to the non-uniform electric field produced by the pointed electrode.

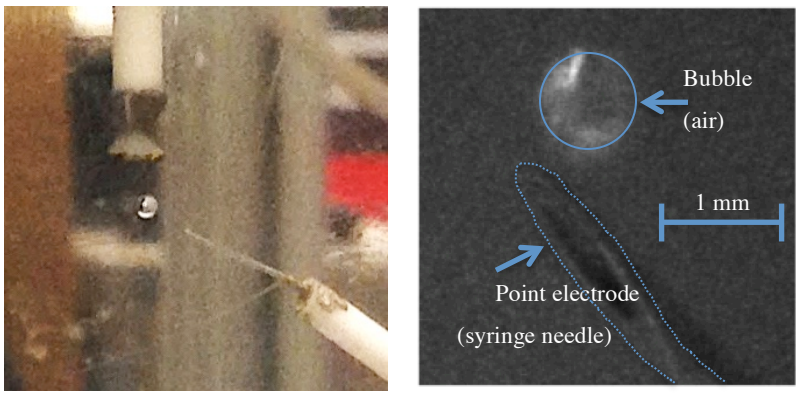

Figure 3.3: Point to plane electrode: left, the electrode set up with levitated bubble (top, ground plane; bottom, pulsed point); right, image of a physical bubble next to point electrode through ICCD.

3.1.1.3 Electrode Attached Bubbles

The presence of plasma and electric fields in water can result in nonlinearity of the water dielectric constant. This can result in the electric field varying nonlinearly with distance from the electrode into the bulk liquid. The point-to-plane electrodes, while more effective at producing

breakdown, increase this non-linear effect. The plane-to-plane electrode configuration was investigated in an attempt to immerse the bubble in a uniform electric field. In the plane-to-plane configuration, the bubble was in contact with the top, powered electrode. In addition to investigating bubbles not in contact with the electrode, electrode-attached bubbles were also investigated. It is presumed a water film between the bubble gas and the electrode was present.

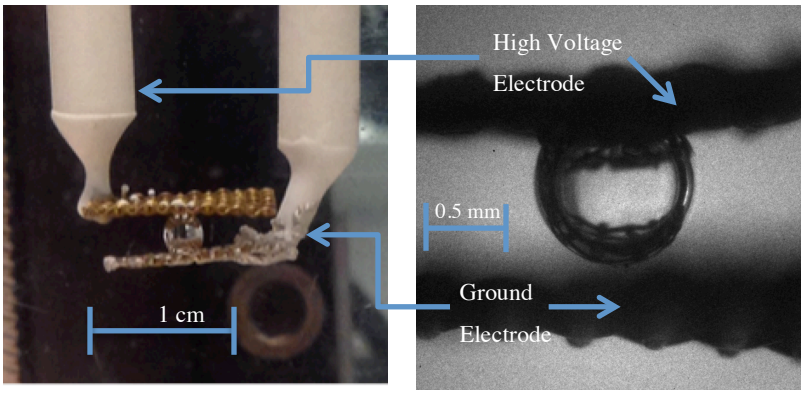

Figure 3.4: Plane to plane electrode: left, the high voltage electrode rests on top of the bubble, with the ground electrode underneath (not touching); right, the image of a bubble in between the electrodes.

3.1.1.4 Equipment

3.1.1.4.1 Electrodes

The immersed electrical lead that powered the electrode was isolated from the water using alumina tubing. The actual contact between the lead and the electrode was made using silver conductive epoxy with an outer layer of waterproof epoxy was used for construction. The alumina aided in shielding the system from parasitic discharges. The point electrode was constructed from a 30 gauge (0.305 mm OD) stainless steel, syringe needle. The plane-to-plane electrodes were constructed from a brass wire mesh of 0.25 mm in diameter and 0.75 mm spacing. The choice of mesh in the construction of the plane-to-plane electrodes was made to minimize the physical perturbation to the acoustic trapping field.

3.1.1.4.2 Power

Plasma in both electrode configurations was ignited by a Suematsu MPC1300S fast, μs-pulser. The pulser produces pulses of positive polarity with a rise time of 100 ns and a pulse width of 1 μs. The pulses can be produced either as a single shot or at repetition rates up to 2kHz

with peak voltages up to +14 kV. As the pulser was used with an open load (ignition into water, mismatched to its optimal 500 Ω load), a large overshoot occurs with the pulse. An example voltage profile with camera signal (used to correlate the camera exposure to when the plasma is ignited) is shown in Figure 3.5.

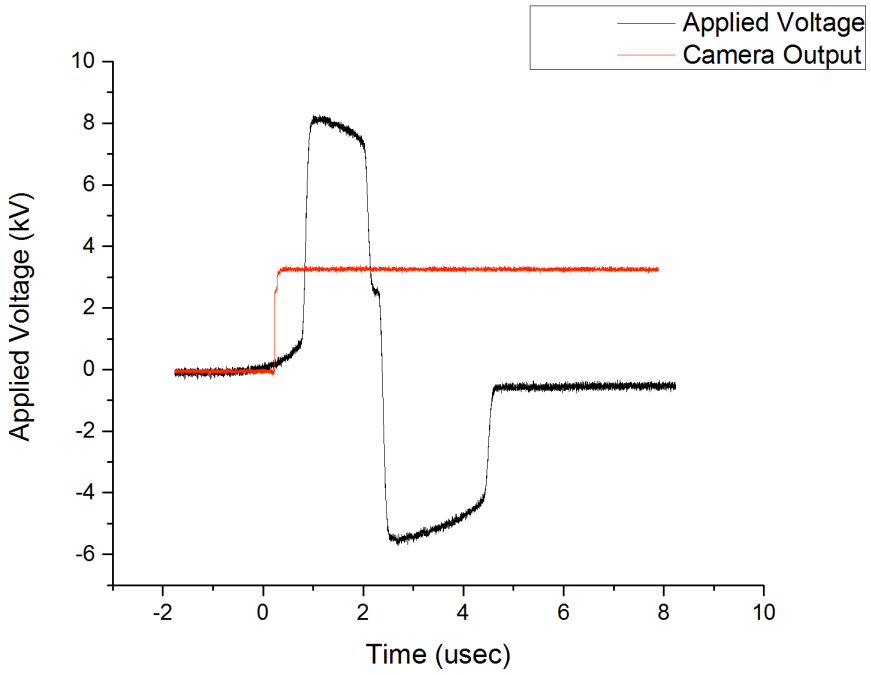

Figure 3.5: Typical voltage profile and corresponding camera turn-on.

3.1.1.5 Producing Degassed Water

Levitation is enhanced when the water used in the chamber is degassed. Degassing removes much of the dissolved gases, which allows for better coupling to the trapped bubble. Gas bubbles within the liquid result in scatter of an ultrasonic field [**311**]. Coupling is significantly reduced or impossible in water with dissolved oxygen concentrations of 4 mg/L and higher.

To degas the water, deionized water was boiled for 45 minutes. As oxygen solubility decreases with increasing temperature (Table 3.1), bringing the water to a boil removes the oxygen (and other dissolved gases). The boiled water is then rapidly cooled in an ice bath for 15 minutes. The process of degassing the water brings the water from roughly 6 to 7 mg/L down to 1.5 mg/L. After approximately 2 hours, the water typically reaches a dissolved oxygen content of about 3.75 to 4 mg/L.

3.1.2 Bulk Plasma Chemistry in Bubbles

To study plasma-driven chemistry and plasma spectroscopy, the experimental apparatus described in the previous section is not ideal due to the limitations of bubble size (i.e., low production of chemical species) and the relatively large optical depth (i.e., limiting spectroscopic investigations). To study plasma-induced chemistry on a scale, a dielectric barrier discharge that is operated underwater (i.e., with water acting as the dielectric between the powered electrode and the ground electrode) was used (see Figure 3.6). This set up allows for spectroscopic analysis, different gases, and large process volumes (100 mL +) to study decomposition efficacy.

Table 3.1: Oxygen solubility with temperature. From [312].

Temperature-Oxygen Solubility Relationship	
Temperature (°C)	*Oxygen Solubility (mg/L)*
0	14.6
5	12.8
10	11.3
15	10.2
20	9.2
25	8.6
100	0

The central, powered electrode, centered within a quartz tube, is biased with a low frequency RF (1 – 5 kHz), sinusoidal voltage (2 – 20 kV_{pk-pk}). An Elgar 501SL power supply provided the input signal to a 50:1 step-up transformer to provide the high voltage signal. In this work, copper and tungsten were used separately in the construction of the powered electrode. Primarily argon, air and helium were used as feed gas for this work. If no feed gas is injected into the quartz tube, localized heating at the electrode tip generates a steam bubble within which the discharge ignites. External to the quartz tube, a coiled ground electrode was positioned near the exit of the tube, at approximately 0.4 mm from the exit. Molybdenum and copper wires were used separately during operation. The apparatus in operation is shown in Figure 3.7. A complete experimental diagram is displayed in Figure 3.8, in which the discharge system in conjunction with time-resolved spectrometer with oscilloscope may be seen.

The underwater DBD plasma jet may be operated in three different modes: (1) the microdischarge mode; (2) the jet mode; and (3) the steam mode (discussed in detail in Chapter

7). The microdischarge mode is characterized by the presence of micro-spikes in the current waveform (see Figure 3.9) and lower power consumption (see Figure 3.11). The discharge is localized primarily to the discharge tube. The jet mode is characterized by a strongly modulated current and the appearance of a plasma jet present in the bubble (see Figure 3.10). The discharge is operates at higher power. (see Figure 3.12) [**313**]. Typical voltage and current waveforms for the jet mode operating with gas are shown in Figure 3.13, while waveforms for the steam plasma are displayed in Figure 3.14. The primary mode discussed throughout this dissertation is the jet mode.

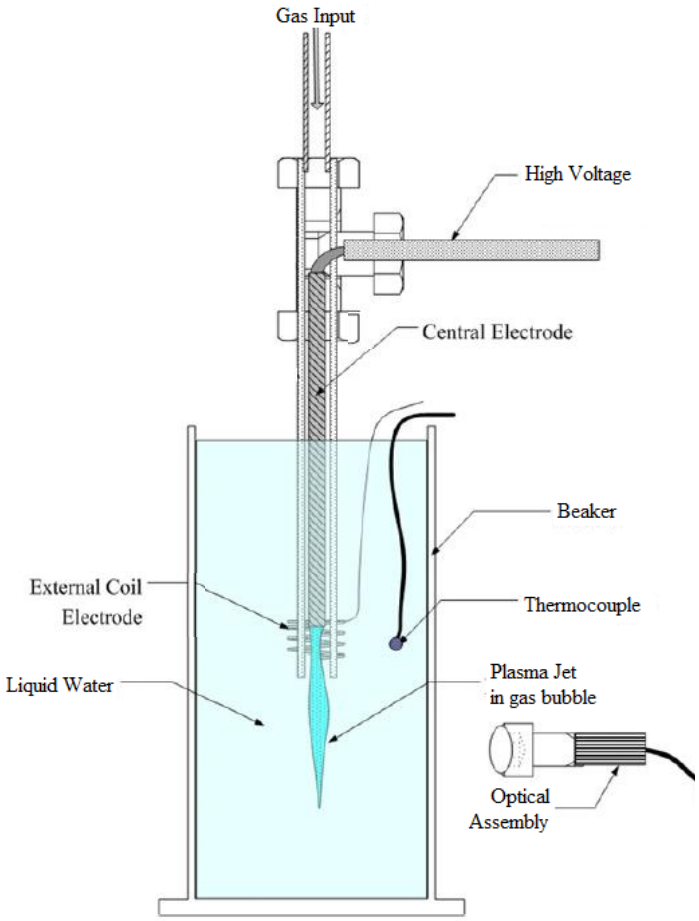

Figure 3.6: The underwater DBD plasma apparatus [95**].**

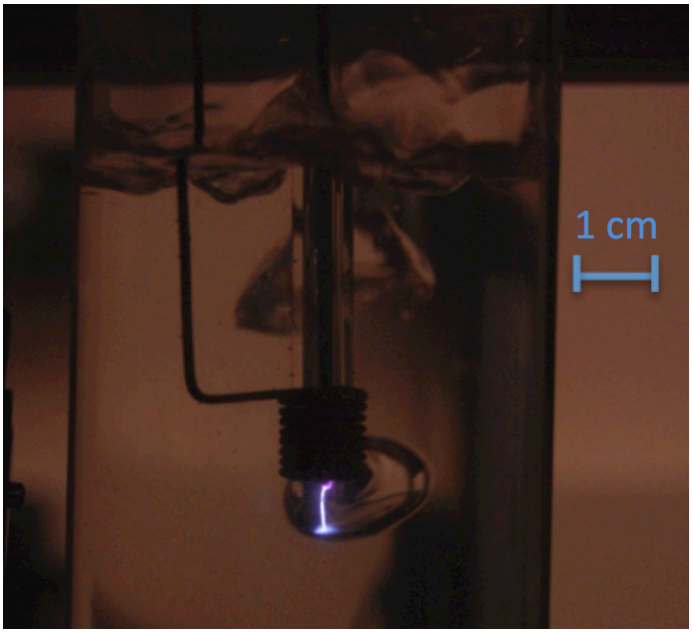

Figure 3.7: The underwater DBD used in all plasma chemistry experiments in operation (argon discharge in deionized water).

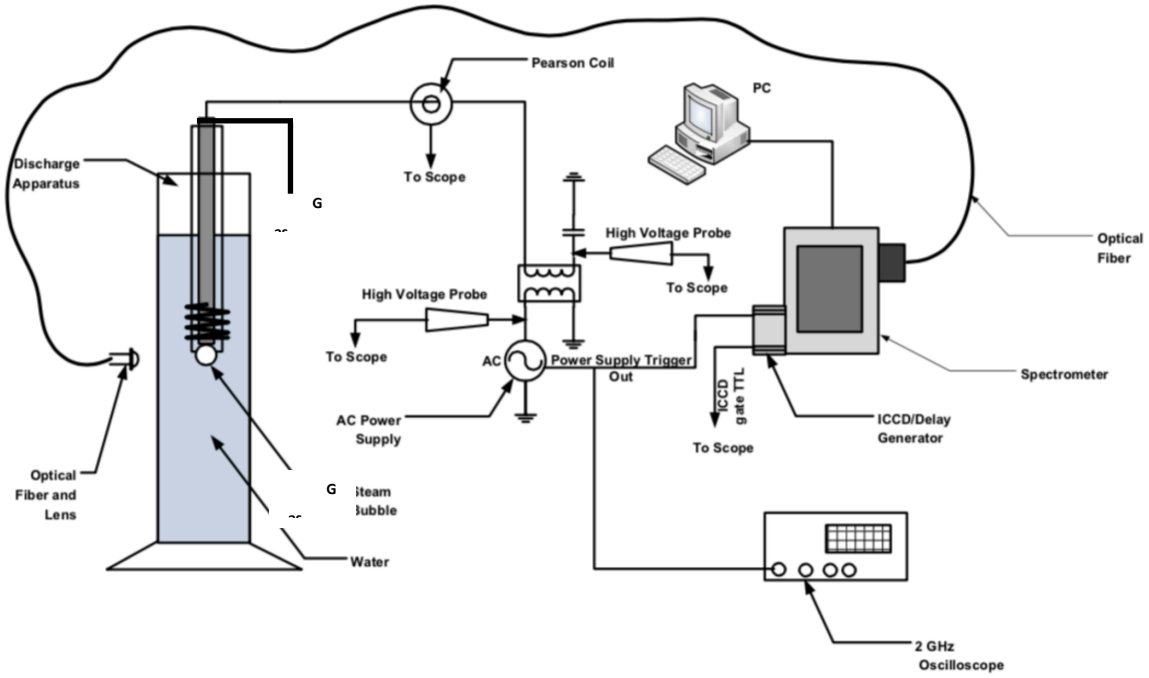

Figure 3.8: Experimental diagram of the set up [314**].**

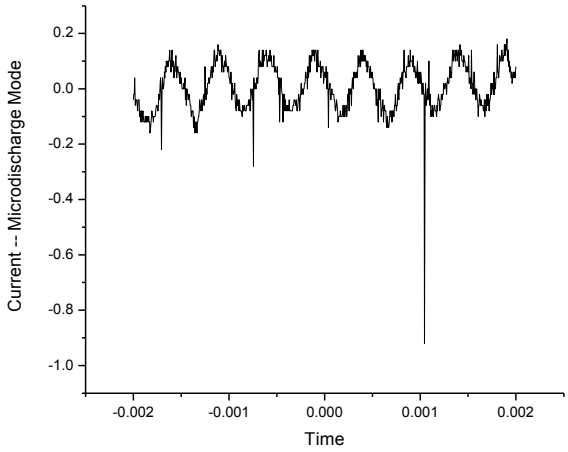

Figure 3.9: Microdischarge mode current profile.

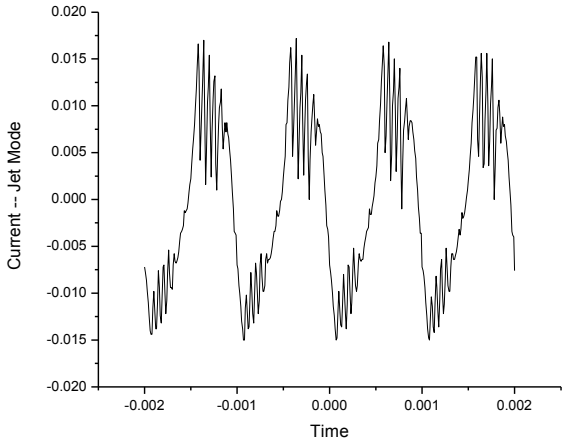

Figure 3.10: Jet mode current profile.

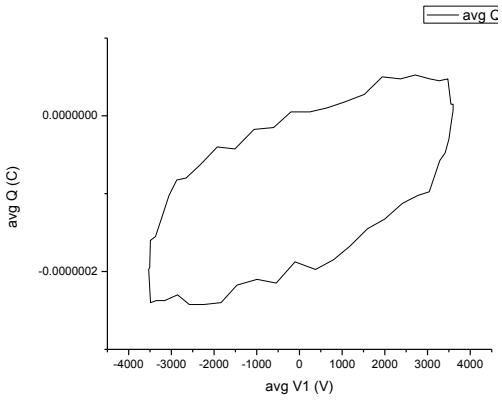

Figure 3.11: Microdischarge mode Lissajous figure. Applied voltage: 3.7 kV peak-to-peak, 2 kHz. Deposited power: 3.2 W.

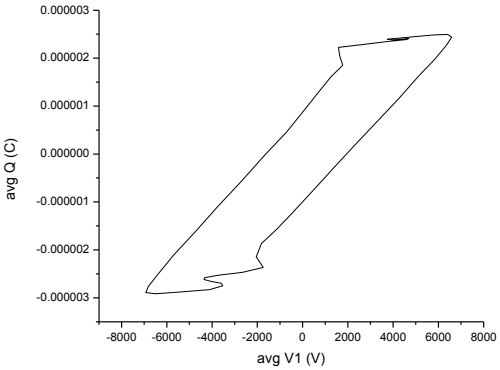

Figure 3.12: Jet mode Lissajous figure. Applied voltage: 6.7 kV peak-to-peak, 2 kHz. Deposited power: 112 W

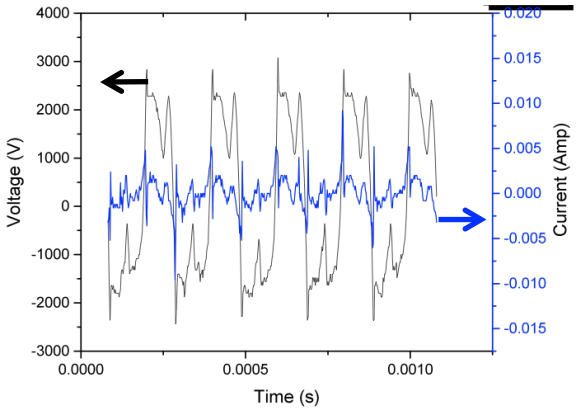

Figure 3.13: Typical voltage and current waveforms of the discharge running in jet mode and a feed gas.

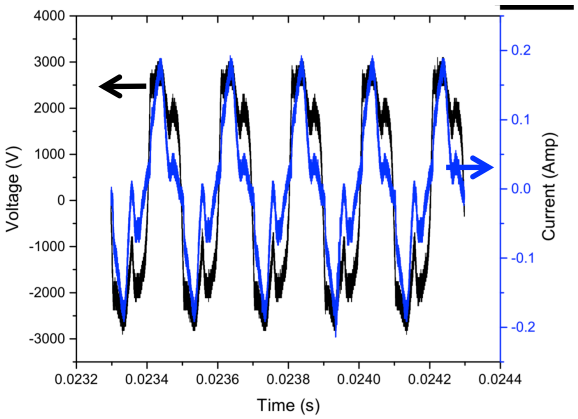

Figure 3.14: Typical voltage and current waveforms of the discharge running in jet mode without a feed

Gas is room air (~2.5 SLPM). gas/in the steam discharge mode.

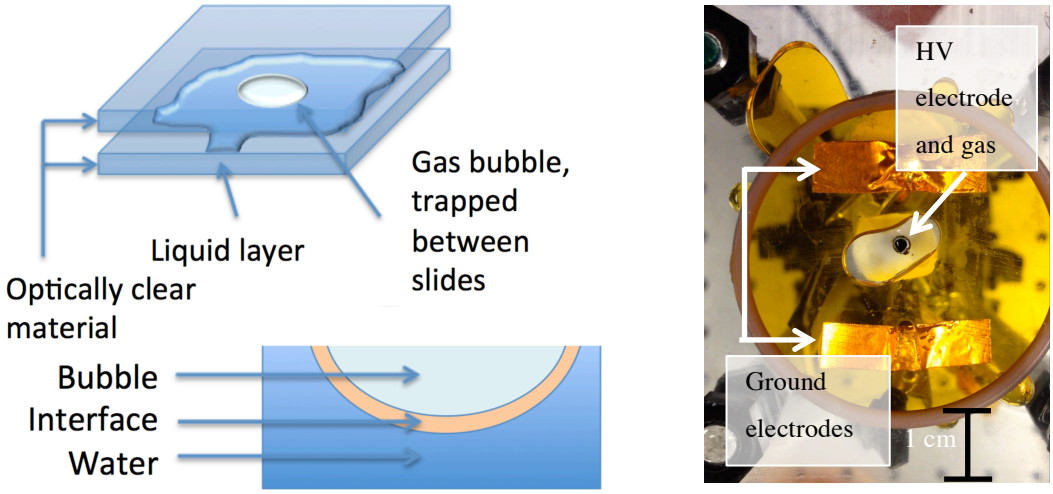

Figure 3.15: The Two Dimensional Bubble. Left, simplified schematic; right, one iteration of the cell in operation (with methyl orange, a pH indicator).

3.1.3 Two Dimensional Bubble

The final experiment is the development and demonstration of the two dimensional bubble cell (schematic in Figure 3.15), which is proposed as diagnostic to study the interface region between plasma and liquid. Similar to a Hele-Shaw cell, a device to study Stokes and other flows in fluid mechanics studies, the two dimensional bubble cell has been developed and tested. The experiment allows one to analyze essentially a cross-section of a normal, three dimensional bubble to study the boundary region between the gas and the bulk liquid.

A simplified view of the device and one of the iterations of the apparatus currently being investigated is shown in Figure 3.15. As the plates are close together, viscous forces dominate and only two dimensions (i.e., in the plane of the plates) become important. This makes the fluid motion in the cell mathematically equivalent to flows in two dimensions. As the bubble is flat, the optical depth of the intervening water is greatly reduced, thereby allowing for direct optical interrogation.

The results presented on this diagnostic are meant to be indicative of the capabilities of the device, and are simplified in comparison to the other experimental results presented in this dissertation. However, the development of this device is exciting as it enables a whole new scope of investigations to be carried out.

3.2 Optical Diagnostics and Imaging Systems

3.2.1 Photography

3.2.1.1 iCCD

An intensified CCD camera (PI-MAX3, Princeton Instruments) was used extensively throughout this dissertation research for both imaging plasma ignition and as a detector for the spectrograph. The short gate (2.5 ns) allowed the imaging of fast phenomena, such as the study of the time evolution of discharge processes. The imaging array of this iCCD was 1024x256, with a spectral response of 300-800 nm. Sensitivity was adjusted via gain settings in software, with 1 to 200 counts/photoelectron. Typical gate and exposure times used in this work ranged from 100 ns to 100 μs.

3.2.1.2 High-Speed Photography

High-speed photography (Redlake MotionPro HS-4 camera) recorded the steam bubble formation (exposure, 1 μsec; frame rate, 200,000 fps). The camera was a black and white device with a 1024x1024 imaging array.

3.2.2 Spectroscopy

Optical emission spectroscopy, both time resolved and time averaged, was one of the primary diagnostic techniques used throughout this dissertation research. In addition to analyzing species production in various discharges and production dependency on discharge parameters, it was also used to determine discharge parameters such as gas temperature and electron density.

3.2.2.1 Time Averaged Spectroscopy

To analyzed line widths a higher resolution spectrometer was used. This spectrometer was fitted with a photomultiplier tube. Time averaged spectroscopy was carried out using a Czerny-Turner type scanning monochrometer with 1 m focal length (AM-510 from Acton Research Corporation (ARC)). A grating of 1200 g/mm was used for all experiments. The detector used with this system was a photo multiplier tube.

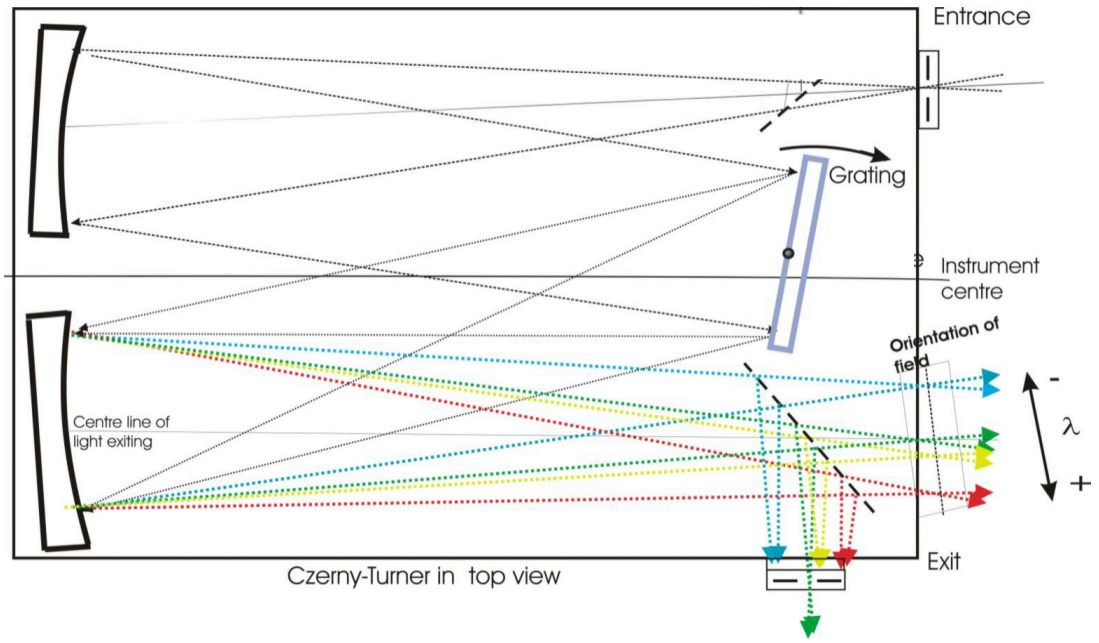

Figure 3.16: Example optics of a monochrometer. The grating turns to observe other wavelengths. From [315].

3.2.2.2 Time Resolved Spectroscopy

The time resolved device was a Czerny-Turner type spectrometer (Acton Series, SP-2300i), focal length 0.3 m. The spectral resolution was 0.02 nm. The spectrometer is equipped with three gratings; for all experiments in this dissertation, the grating with the highest groove density available was used. This grating was 1800 g/mm with holographic-UV blaze (corresponding to an optimum range of 190-450 nm). The equipment was operated via *WinSpec32* software.

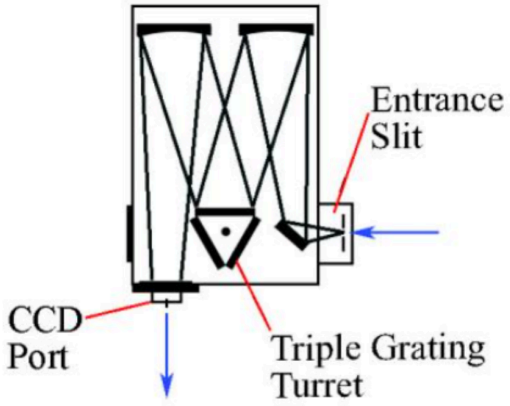

Figure 3.17: Schematic of the spectrograph used throughout this research (image from Acton/Princeton Instruments).

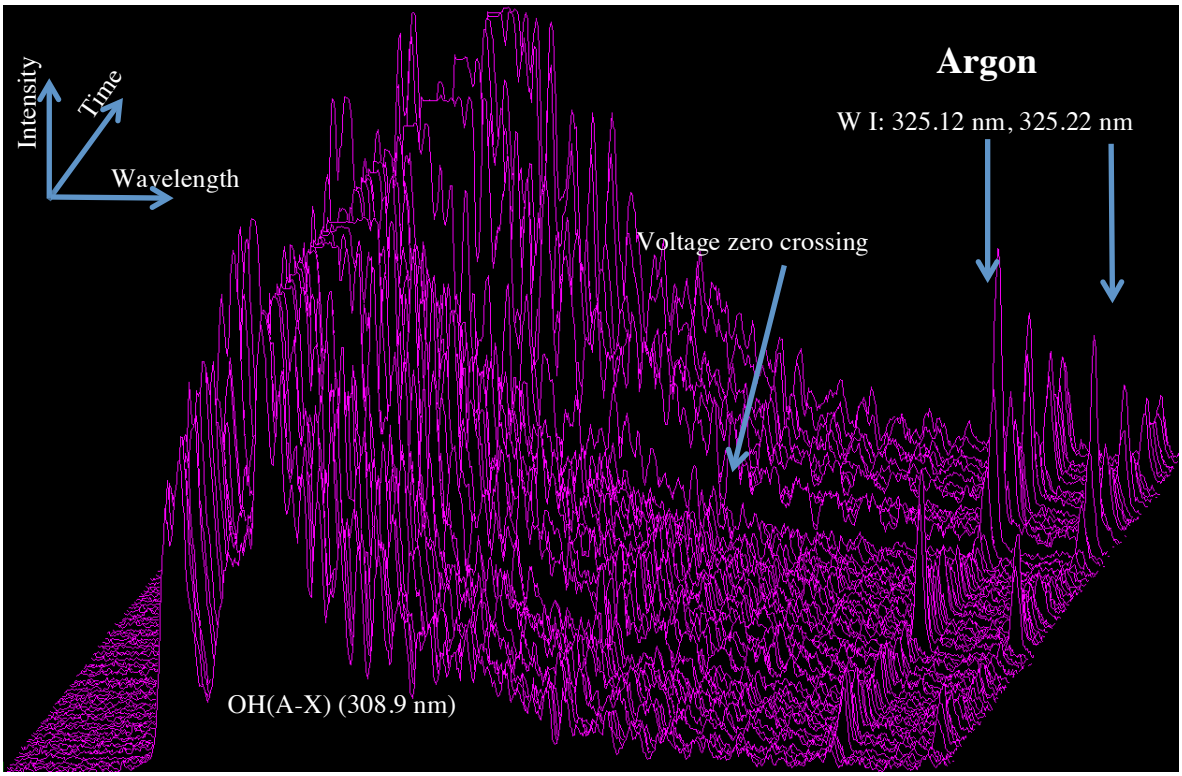

Figure 3.18: OH (A-X, 308.9 nm) system with tungsten lines (WI, 325.12 nm and 325.22 nm, from electrode). Argon plasma.

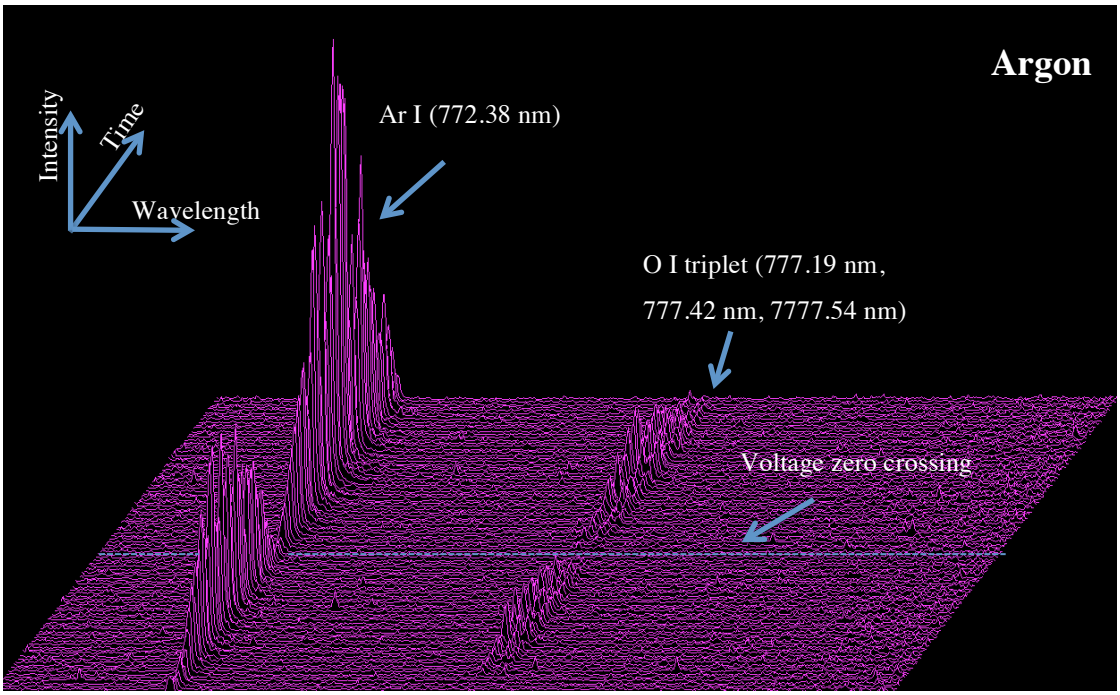

Figure 3.19: Left peak: Ar I, 772.38 nm. Middle triplet: O I (777.19 nm, 777.42 nm, 777.54 nm). Argon plasma.

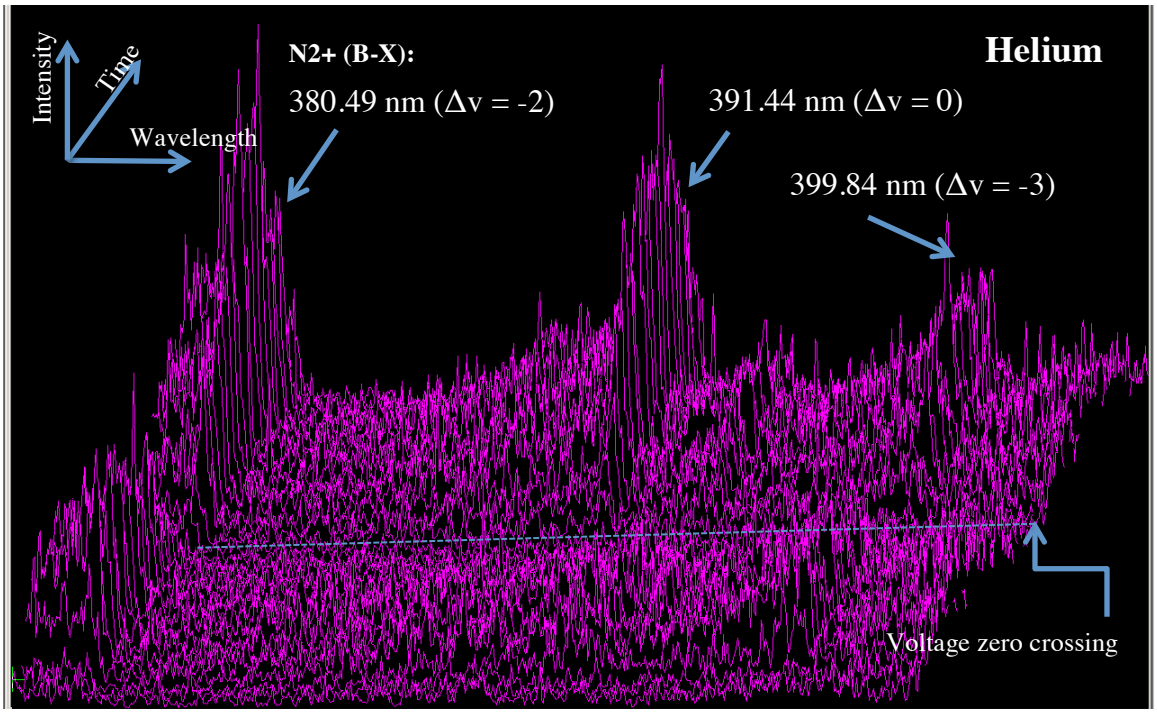

Figure 3.20: N_2^+ first negative system (B-X). Leftmost peak, 380.49 nm (Δv = -2); middle peak, 391.44 nm (Δv = 0); rightmost peak, 399.84 nm (Δv = -3). Helium plasma.

The detector used in conjunction with this spectrograph was the PI-MAX3 iCCD. Optic fiber channeled the plasma emission from the source to the spectrometer. Acquisition was synchronized via delay generator. Emission spectra acquired allow for the determination not only of the gas composition making up the plasma but also plasma gas temperature and electron number density over time during a voltage cycle. Examples of data acquired may be seen in Figure 3.19 through Figure 3.18. Each figure is made of 100 individual time-resolved images, corresponding to a time step resolution of 2 microseconds for each image. The dip in the center of each image corresponds to the voltage zero crossing (as the applied voltage for all of these discharges was sinusoidal).

To account for the varying pixel gain across the chip and spectra range, a flatfield was applied to all data post data collection. The flatfield was measured through imaging the most flat portion of a tungsten lamp spectra (528-551 nm).

3.2.2.3 Instrumental Broadening

The primarily source of line broadening was instrumental broadening. For both units, the instrumental broadening was determined via 30 mW He-Ne laser. The 632.8 nm Ne I line was recorded at various slit widths and its shape was fit with a Gaussian profile to determine broadening.

The instrumental broadening of the spectrometer for the slit widths used (10 μm and 15 μm) fit a Gaussian profile with a FWHM of 0.14 nm. Sources of instrumental broadening include non-ideal optics, wavelength dispersion, and axial divergence.

The instrumental broadening of the monochrometer was measured over the range of slit widths used, and was found to range between 0.04 nm and 0.20 nm (see Table 3.2).

Table 3.2: Measured instrumental broadening of the monochrometer.

Slit Width (μm)	Broadening (nm)
5	0.04
10	0.08
15	0.12
20	0.16
25	0.20

3.2.2.4 Plasma Electron Density[27]

The discharge electron density (n_e) was inferred from the Stark broadening of H_β (486.1 nm, 4→2 transition) atomic hydrogen Balmer series line whose profile shape is sensitive to the micro-field induced by charged particles (i.e., electrons and ions) that surrounds the emitter atom (i.e., hydrogen) [**316**,**317**]. This line is frequently used to determine electron densities as small as 10^{20} m^{-3}. In addition, the full width at half maximum (FWHM) of the emission line has a dependence of $T_e^{1/2}$ the plasma electron temperature, making this line especially convenient for discharges in liquids [**318**]. The Stark broadening linewidths have been theoretically calculated and tabulated by Gigosos et al. for wide ranges of electron densities [**319**].

It was assumed that the profile of the emitted H_β line as a Voigt profile, which is a convolution of a Gaussian shape profile and a Lorentzian shape profile. The Gaussian

[27] Work here presented in some form from [**389**].

contribution is attributed to the Doppler and instrumental broadening of the line, and Lorentzian part is associated with van der Waals and Stark broadenings [**318**].

From the best Voigt profile fit, the actual Stark broadening for line was determined. It should be pointed out the Doppler and van der Waals broadenings were calculated using expressions given by Bruggeman et al. [**318**]:

$$\Delta\lambda_{vdW} = \frac{4.10}{T_{gas}^{0.7}}\ [nm]$$

(3.5)

$$\Delta\lambda_{Doppler} = 3.48{\times}10^{-4}T_{gas}^{1/2}\ [nm]$$

(3.6)

Finally, using the tables from Gigosos et al. [**319**], the electron density was calculated. The electron density can also be found directly using the following equation [**318**]:

$$\Delta\lambda_{Stark} = 4.8\ nm{\times}\left(\frac{n_e}{10^{23}m^{-3}}\right)^{0.68116}$$

(3.7)

Both methods were used in this dissertation research, and the calculated electron densities were typically 10^{20} to 10^{21} m^{-3} [**320**].

In some discharges, the H_β line is too weakly emitting or has been depopulated and is unusable as a method to determine electron density as described above. In those circumstances, the H_α line (656.3 nm, 3→2 transition) is used. Using the Stark broadenings of the H_α line, the measurements are repeated and electron density determined. However, even though this line has a higher intensity, it is a less reliable method to measure electron densities (especially for smaller electron densities, on the order of 10^{19}, 10^{20} m^{-3}) due to its smaller FWHM, its higher sensitivity for self-absorption and its stronger dependence on kinetic equilibrium conditions in the plasma. Electron densities obtained from H_α were found to be higher than those measured using H_β line, but their trend over the time was quite similar in all instances observed throughout this dissertation research.

3.2.3 Photo Diode Detector

A high-speed photo diode (Thorlabs DET210; rise time, 1 ns; 350 MHz operation) was used to detect the presence of light associated with ignition and the evolution of plasma induced emission over a cycle. In particular, the photodiode was used to study the asymmetric quality of the bulk bubble plasma system of Chapter 5 and the plasma ignition of the steam discharge in Chapter 6.

3.3 Chemical Diagnostics

3.3.1 Bench-Top Measurements

3.3.1.1 pH, Conductivity and Dissolved Oxygen

pH, conductivity and dissolved oxygen measurements were performed with a handheld meter (Thermo Scientific Orion Star A329). Some of its extensive capabilities include pH range of -2.000 to 20.000 (± 0.002), conductivity range of 0.001 µS/cm to 3000 mS/cm (sensitivity of 0.5% of ± 1 digit > 3 µS; 0.5% of ± 0.01 µS ≤ 3 µS), and dissolved oxygen range of 0.00 to 50.00 mg/L (accuracy of ±0.1mg/L up to 8mg/L, ±0.2mg/L from 8 to 20mg/L, ±10% of reading up to 50mg/L). All measurements were temperature compensated with onboard ATC (automatic temperature compensator) probe with an accuracy of ±0.1°C.

3.3.1.2 Spectrophotometry

A spectrophotometer was used to measure the quantity of methylene blue dye in the liquid, before, during and after treatment. The spectrophotometer allows one to calculate the concentration of dye in the liquid via the Beer-Lambert equation:

$$I(x) = I(x = 0)10^{\theta xc} \tag{3.8}$$

Here, I is the intensity of light transmitted through the solution (units of W m^{-2} or other suitable units), $I(x=0)$ or I_0 is the initial quantity of light entering the solution (same units as I), θ is the molar absorption coefficient (for methylene blue dye: 3.67×10^4 L mol^{-1} cm^{-1} at 609 nm [**321**]), x is the optical pathlength through the liquid, and c is the concentration of the measured constituent in the liquid (in M, or mol L^{-1}). The fraction of I over I_0 is the quantity of light that is

transmitted through the liquid. This quantity is referred to as transmissivity, T. It is related to the relative absorbance, A, of light passing through the liquid via

$$-\log_{10}\frac{I(x)}{I_0} = -\log_{10} T = A = \theta x c$$

(3.9)

Using a spectrophotometer, this relation allows the concentration of a substance to be determined. Spectrophotometers detect the amount of light transmitted through the sample medium (wavelength of incoming light, typically in the 400-700 nm range, may be selected via grating, see Figure 3.21); taking the value of the quantity of light absorbed and other material-dependent variables given in (3.9) allows the concentration of the sample to be determined. In this work, the optical pathlength was 1 cm. The wavelength setting of the spectrophotometer was 609 nm, a strong absorbance peak for the dye [**321**].

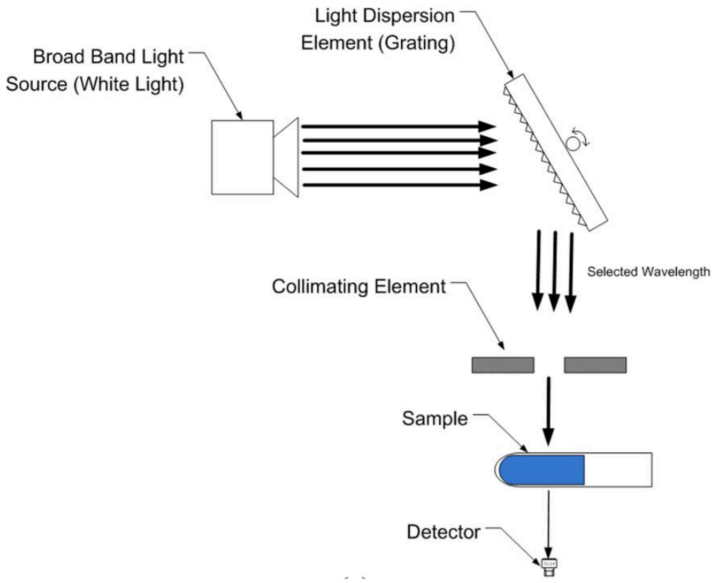

Figure 3.21: Schematic of a spectrophotometer. From [96].

3.3.1.3 Hydrogen Peroxide

Hydrogen peroxide concentration in plasma treated solutions was determined enzymatically with colorimetric test strips for rapid, in-situ H_2O_2 determination (sensitive to a range from 0 to 25 mg/L H_2O_2), and via iodometric titration (Hach HYP-1, range of 0.2-2 and 1-10 mg/L to) for post-processing peroxide determination. The iodometric titration method utilizes ammonium molybdate to catalyze the peroxide, and the solution is acidified with sulfite reagent. Potassium

iodide reacts with the peroxide to form free iodine and water (see (3.10). To determine the H_2O_2 concentration, sodium thiosulfate titrates the iodine and the quantity of peroxide is calculated (see (3.11).

$$H_2O_2 + 2\,KI + H_2SO_4 \rightarrow I_2 + K_2SO_4 + 2H_2O \quad \textbf{(3.10)}$$

$$I_2 + 2\,Na_2S_2O_3 \rightarrow Na_2S_4O_6 + 2\,NaI \quad \textbf{(3.11)}$$

Hydrogen peroxide concentration is used as a metric for reactive species generation as the formation of hydrogen peroxide is believed to be principally due rate and energy of production costs provides a metric for comparison to other advanced oxidation methods including other plasma-based water purification methods [**177**].

3.3.2 Chromatography

Chromatography was used as the primary method of species identification (other than hydrogen peroxide, which was determined enzymatically and iodometric titrations). All gas and ion chromatography (GC and IC, respectively) was conducted with Mr. Tom Yavarski, Department of Civil and Environmental Engineering, University of Michigan, at the Water Research Laboratory of the Environmental and Water Resource Engineering group. All samples for GC and IC were prepared by the author and Mr. Yavarski. All high-performance liquid chromatography (HPLC) was conducted by Mr. Jim Windak of the Department of Chemistry, University of Michigan, at the Mass Spectrometry Lab of the Chemistry Department. All samples for HPLC (after being created) were prepared by Mr. Windak.

3.3.2.1 Gas Chromatography

Gas chromatography (GC) is a straightforward method that can be highly sensitive (10s of ppt (parts per trillion), or ng/L), and is a common analytical chemistry diagnostic. A gas chromatograph vaporizes the sample and the sample is broken up into its different constituents. As the sample moves through the column of the device (see Figure 3.22), the velocity of each component is based on its individual chemical interaction with the column it travels through. The substances that have very little interaction with the column material exit the chromatograph

sooner with a short retention time, and those with greater interaction leave at late times. After leaving the column, the compounds enter a detector. All gas chromatography work in this dissertation utilized an electron capture detector, with a detection limit of approximately 0.5 ppb (μg/L). An electron capture detector was chosen to best complement the analyzed species in question, that is, highly electronegative compounds (here, halogenated compounds). The detector uses a beta emitter in the sample stream, and as an electronegative sample passes by, the compound collects extra electrons as it travels to the anode. A current of the collect species is collected as the species impinge on the anode. Results can be improved based on column and detector selection. The results of a GC are given in a chromatogram, which is a plot of current or arbitrary counts vs. time. These results or constituents themselves may be passed on to additional detectors for additional analyses.

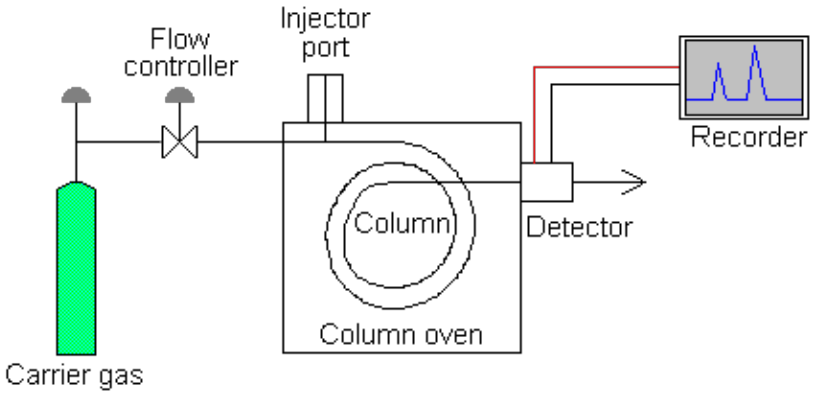

Figure 3.22: A typical gas chromatograph. Choice of carrier gas depends on the column chemistry, but is typically an inert gas. Helium or argon is typically used. From [322].

An example of a chromatogram is shown in Figure 3.23, showing a chromatogram of untreated tap water (in blue) and tap water after six minutes of plasma treatment.

As the retention time and peak area depends on the interaction chemistry of the sample and column, gas chromatography requires a foreknowledge of species composition, or at least a strong educated guess. A GC cannot be used to identify random peaks; one must instead have a "template" with peaks of known identity and concentration to be useful. Because of this limitation, gas chromatography was used very little in this dissertation work. An example of unknown peaks is shown in Figure 3.23, where the plasma produced peaks are apparent, but to

properly analyze, one must analyze standards of likely species first – such as OH, NO_2, NO_3, carbonates, or organic acids.

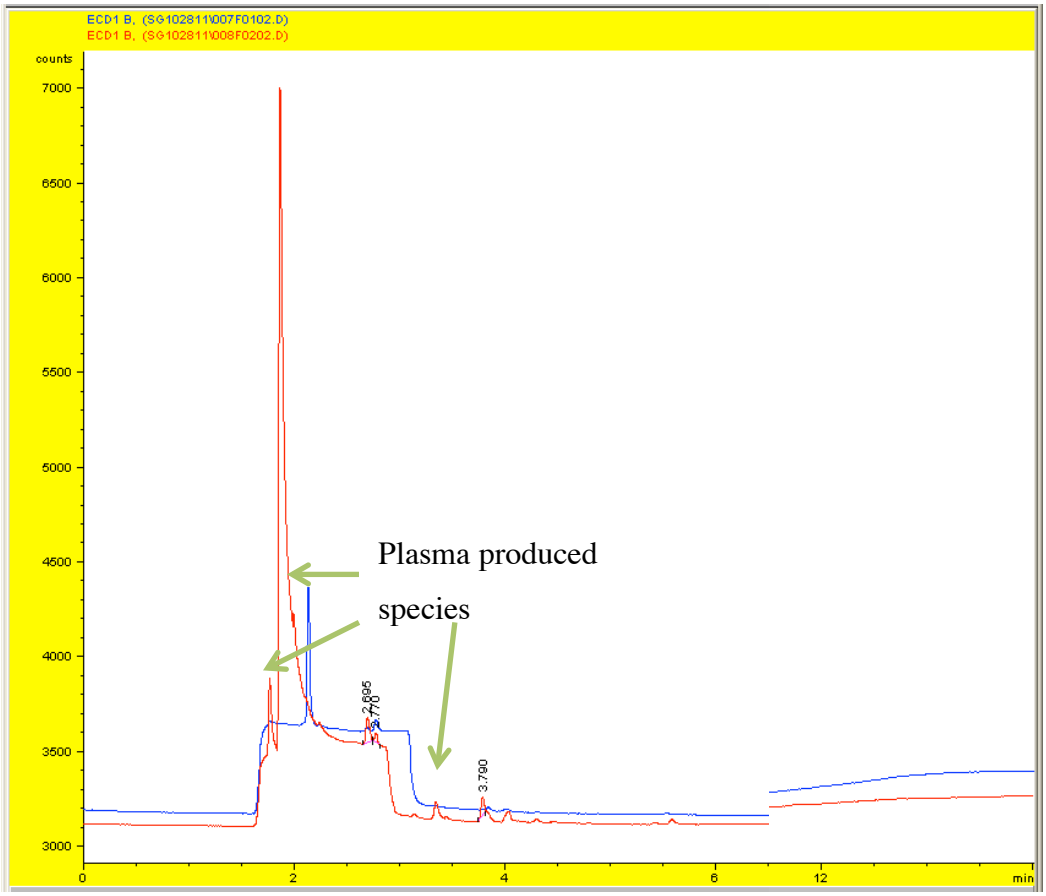

Figure 3.23: Untreated tap water (blue) and tap water with six minutes of plasma jet discharge (red).

3.3.2.2 Ion Chromatography

For direct measurements of the molecular content, samples were analyzed via ion chromatograph (Dionex DX-100). The column used in the analyses was the Dionex IonPac AS-14 analytical column, 4.1x250 mm in dimension and a carbonate eluent (3.5 mM Na_2CO_3/1.0 mM $NaHCO_3$). The analyte is assessed conductometrically via suppressed conductivity detector, with an anion self-regenerating suppressor. This detector decreases the conductivity signal of the mobile eluent and increases the signal of the analyte. The results of the IC system are given as peaks of conductivity with time, where the peaks are calibrated to determine the quantity of the anion in question (i.e., nitrate and nitrite).

3.3.2.3 High-Performance Liquid Chromatography

High-performance liquid chromatography (HPLC) electrospray ionization mass spectrometry (ESI-MS) was used to analyze decomposed methylene blue samples for molecular analysis of plasma degradation. The HPLC was the Agilent Q-TOF (quadrupole time-of-flight), and the ESI-MS used positive ion detection. It should be pointed out that neutrally-charged radicals will not be detected by the ESI-MS detector, as it will only detect cations.

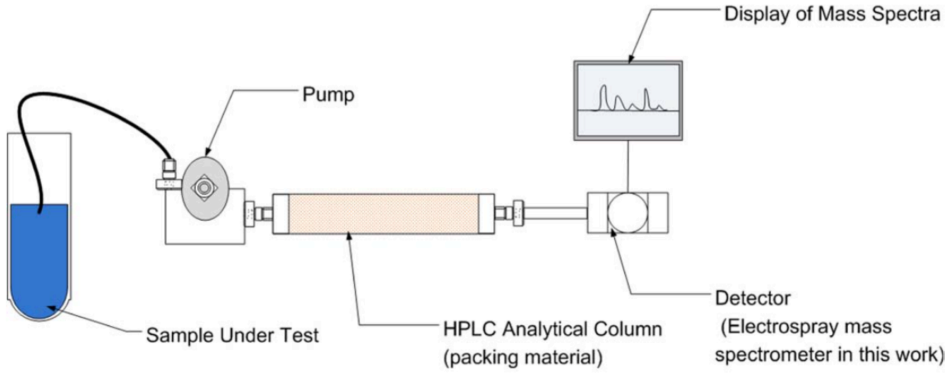

Figure 3.24: Schematic of an HPLC. From [179].

3.4 Additional Experimental Methodology

3.4.1 Electronic Measurements

All voltages were measured with Tektronix P6015A 20-kV, 75 MHz high voltage probes, and discharge current was measured via 6595 Pearson coil. A 2 GHz oscilloscope (LeCroy Wavepro 7200a) was used to record all associated data (i.e., voltage, etc.).

3.4.2 Temperature Diagnostics

The temperature of the high voltage electrode was measured via nickel-chrome high-temperature thermocouple (Super OMEGACLAD XL, ungrounded).

3.4.3 Sonic Verification

A hydrophone (Teledyne Reson TC4013-1, response of 1Hz to 170kHz, sensitivity: -211dB ±3dB.) was employed to study the formation of both the central mass of the steam bubble but as to study the formation of microbubbles in the vicinity of the electrode.

3.4.4 Computational Modeling

Three simulation tools were used in this dissertation research. They include *ANSYS Maxwell*, a finite element method electromagnetic field solver used to calculate local fields produced by the electrodes; *LIFBASE*, a diatomic molecule spectroscopic tool used to simulate rotational and vibrational spectra for determination of gas temperature [**323**]; and *GlobalKIN*, a plasma chemistry model.

3.4.4.1 GlobalKIN

Plasma discharges and the ensuing chemical production in liquids were modeled via *GlobalKIN* [**185**,**184**], a zero-dimensional global-kinetics simulation code expanded to include liquid interactions and chemical reactions within the liquid phase by Lietz [**186**]. The plasma is approximated as a well-stirred-reactor. Electron dynamics are determined via the Boltzmann equation for a range of reduced electric field values (E/N). Densities of electrons, ions, and neutral species are calculated via rate equations. Specific details regarding the functionality of *GlobalKIN* may be found elsewhere [**184**,**185**,**186**]. In this work, a total of 107 species (see Table 3.3; "V" signifies vapor-phase) and 567 reactions (see Appendix) were used to simulate the plasma and plasma chemistry. It should be noted that liquid-phase carbon species, such as CO, were not included in the collection of species and reactions. Based on experimental observation and measurement in this thesis, it is suggested that carbon species may play an important role in liquid-phase chemistry [**324**].

The gas bubble-plasma-liquid system is approximated as a sphere of gas, encased in a thin shell of plasma, surrounded by a layer of liquid. The thin shell of plasma is used to approximate the behavior of a plasma jet in a gas bubble (e.g., following the curve of the change in dielectrics, as seen in [**116**,**106**]). The gas bubble was approximated as a 1 cm diameter sphere with the plasma shell residing in the outer-most 50 μm of the sphere[28]. The depth of the water layer was chosen to be larger than the diffusion length of hydrogen peroxide, the primary species of interest for these experiments, during the simulation time of the plasma discharge. Vapor phase

[28] As in, from the center of the sphere outward on the radial axis, the first 0.495 cm of the sphere is gas, and the last 0.005 cm is plasma.

diffusion of hydrogen peroxide[29] is 0.189 $cm^2\ s^{-1}$, which results in a diffusion length of 0.14 mm after 0.1 seconds (the integration time used in the simulations). Therefore, to accommodate the diffusion of products in the liquid while maintaining low computational cost, the thickness of the water layer was chosen as 0.5 mm.

Table 3.3: Species used in *GlobalKIN* simulation.

Gas-Phase Species Considered

E	N_2	N*	NO_3	HO_2	CO_2
O_2	N_2V	NH	NO_3^-	H_2O_2	CO_2V
O_2V	N_2*	H_2	N_2O	H_2O^+	CO_2^+
O_2*	N_2**	H_2^+	N_2O_4	H_3O^+	NH_2
O_2^+	N_2***	H	N_2O_5	H_3O^+*H_2O	NH_3
O_2^-	N_2^+	H^-	HO_2NO_2	H_2NO^+	NH_3^+
O_3	N_4^+	NO	HNO	C	NH_4^+
O	N_3	NO^+	HNO_2	C^+	CN
O*	N_3^+	NO_2	HNO_3	CO	NCO
O^+	N	NO_2^+	H_2O	COV	C_2O
O^-	N^+	NO_2^-	OH	CO^+	

Liquid-Phase Species Considered

E_L	H_2O^+_L	HO_2_L	H_L	O_2_L
H_2O_L	H_3O^+_L	OH_L	H_2_L	O_3_L
H_2OEL_L	H_2O_2_L	OHL^-_L	O_L	O^-_L
O_2^-_L	NO_2^-_L	N_2_L	O_2^+_L	N_2O_5_L
O_3L^-_L	NO_3^-_L	N_2*_L	H^+_L	N_2O_L
HO_2L^-_L	ONOOL^-_L	N_2**_L	H_3O^+*H_2O_L	HO_2NO_2_L
NO_L	HNO_2_L	N_2^+_L	NO^+_L	
NO_2_L	HNO_2_L	N_4^+_L	N_2O_3_L	
NO_3_L	ONOOH_L	O_2*_L	N_2O_4_L	

Dissolved gases are naturally present in water, and were included in the simulation. The water layer surrounding the plasma and gas sphere included dissolved N_2 and O_2, to represent air. At 1 atmosphere of pressure and 25° C, the solubility of N_2 and O_2 in water are approximately 0.0175 g/kg of water and 0.04 g/kg of water, respectively [**325**]. Using the partial pressure of each gas[30], the mass of each gas in the volume of the liquid is calculated and used as the initial conditions

[29] In air, at 60° C, 1 atm [**437**].

[30] Approximating air as a mixture of 79% N_2 and 21% O_2.